UNIVERSITY OF STRATHCLYDE

Adaptation of TFM for Inspection of Complex Components

A Thesis submitted in fulfilment of the requirements

for the degree of Doctor of Engineering

Ailidh McGilp

Centre for Ultrasonic Engineering

Department of Electronic and Electrical Engineering

May 2016

Declaration of Authorship

This Thesis is the result of the author's original research. It has been composed by the author and has not been previously submitted for examination which has led to the award of a degree.

The copyright of this Thesis belongs to the author under the terms of the United Kingdom Copyright Acts as qualified by University of Strathclyde Regulation 3.50. Due acknowledgement must always be made of the use of any material contained in, or derived from, this Thesis.

Signed:

Date:

Abstract

Ultrasonic inspection is a major Non-Destructive Evaluation (NDE) method used to assess the integrity of components in nuclear power plants. It is one of only a few methods capable of volumetrically interrogating a component, and it is therefore key to the essential maintenance schedule required to operate nuclear plant. Recent years have founded significant advances in ultrasonic technology, including the introduction of phased arrays, increased computer power and the development of innovative signal processing algorithms. These aspects can be combined to offer the potential of improving current inspection capabilities, by enhancing their efficiency and performance. Challenging inspections, such as those involving complex geometry components, would particularly benefit from such improvements.

The Total Focusing Method (TFM) is now widely accepted as the gold standard of ultrasonic imaging algorithms. Despite this recognition it is yet to be widely utilised in industry, meaning that along with arrays it has essentially remained a research topic. This study aims to bring together the key elements, to contribute towards an efficient inspection for complex components.

An efficient implementation of TFM incorporating an auto-correction routine to handle refraction through an arbitrary inspection surface has been developed. A bespoke sparse 2D array adds to the efficiency of the inspection, which is demonstrated on a calibration test block representative of in-service components. Furthermore, a method for determining the relative sensitivity in an inspection of complex components using TFM is formed.

Acknowledgements

The author would like to acknowledge the support provided by numerous individuals throughout her time completing this EngD.

Prof. Anthony Gachagan

I would like to offer my sincere gratitude to my supervisor Tony, who has coached me through the past 4 years. He is the most humble Prof. I ever expect to meet and I am thankful for all of the academic guidance and encouragement he has provided me with.

CUE

I would like to extend thanks to various members in CUE who I have worked with throughout my EngD. Credit especially to Jerzy Dziewierz, Timothy Lardner and Bo Xiao who I worked with intensively to develop the software required for this study. Thanks also to Tommy McCunnie, John Mackersie and Charles MacLeod who helped immensely with the manufacture of my array.

Doosan Babcock

I would like to thank the industrial partner of this work Doosan Babcock, for their sponsorship. I would especially like to acknowledge Colin Bird for his supervision, enthusiasm and guidance throughout my EngD. Essentially he was the one who inspired me to start the EngD and he has provided me with ongoing support.

Additionally, I would like to thank my colleagues at Doosan Babcock for their friendship, support and wisdom throughout my project. I'm sure they will all be glad the write-up process is over.

RCNDE

I would also like to show my appreciation for RCNDE, who are doing a wonderful job in raising the profile of NDE. I found the EngD scheme thoroughly enjoyable, and I really feel it has prepared me well for an industrial career. Credit must also be given to my EngD colleagues who added greatly to my experience.

Family & Friends

Finally, I would like to extend my greatest thanks to my family and friends. First to my parents, Peter and Isabel, for planting a thirst for knowledge in me at a young age, and supporting me in whatever I wish to do. To my partner Alan, for always believing in me and motivating me to be the best I can be. Thanks also to my sister and nephew, Mhairi and Harvie, for being there for me throughout. Also I owe my four Pointers some attention, for the welcome distraction from work they always give me.

I have been given unconditional love and support from you all, and that means more to me than any title.

Last but not least, I would like to say cheers to all of my close friends who I can now enjoy spending time with again.

Contents

List of Figures

List of Tables

Abbreviations

NDE	**N**on **D**estructive **E**valuation
UT	**U**ltrasonic **T**esting
EngD	**Eng**ineering **D**octorate
RCNDE	**R**esearch **C**entre for **N**on **D**estructive **E**valuation
CUE	**C**entre for **U**ltrasonic **E**ngineering
SDH	**S**ide **D**rilled **H**ole
BW	**B**ack **W**all
PAC	**P**hased **A**rray **C**ontroller
TFM	**T**otal **F**ocusing **M**ethod
GP-GPU	**G**eneral **P**urpose - **G**raphics **P**rocessing **U**nit
DAC	**D**istance **A**mplitude **C**orrection
FMC	**F**ull **M**atrix **C**apture
BINDT	**B**ritish **I**nstitute of **Non** **D**estructive **T**esting
SONAR	**SO**und **N**avigation **A**nd **R**anging
P-E	**P**ulse - **E**cho
P-C	**P**itch - **C**atch
Tx	**T**ransmitter
Rx	**R**eceiver
Nz	**N**ear **z**one
Fz	**F**ar **z**one
SNR	**S**ignal to **N**oise **R**atio

dB	**d**eci**B**el
FSH	**F**ull **S**creen **H**eight
FEA	**F**inite **E**lement **A**nalysis
ENIQ	**E**uropean **N**etwork for **I**nspection **Q**ualification
Tx-Rx	**T**ransmit - **R**eceive
HMC	**H**alf **M**atrix **C**apture
SMC	**S**parse **M**atrix **C**apture
SAFT	**S**ynthetic **A**perture **F**ocusing **T**echnique
PCI	**P**hase **C**oherence **I**maging
ToF	**T**ime **o**f **F**light
FPGA	**F**ield **P**rogrammable **G**ate **A**rray
CPU	**C**entral **P**rocessing **U**nit
PoR	**P**oint **o**f **R**efraction
MP5	**M**icro**P**ulse **5**
P-Axis	**P**rimary - **A**xis
RMS	**R**oot **M**ean **S**quare

Symbols

d	Distance
c	Velocity (with shear (s) or longitudinal (l) components)
ρ	Density
E	Young's Modulus
μ	Poisson's Ratio
f	Frequency
λ	Wavelength
Z_a	Acoustic Impedance
T_c	Transmission Coefficient
R_c	Reflection Coefficient (with shear (s) or longitudinal (l) components)
θ	Angle (various components defined in text)
T_p	Transducer thickness
θ_{half}	Half angle of ultrasonic beam
k	Ultrasonic beam amplitude factor
R_{Nz}	Range of near zone
D	Ultrasonic source diameter
p	Element pitch (with primary (p) or secondary (s) components)
w	Element width (with primary (p) or secondary (s) components)
L	Element length (with primary (p) or secondary (s) components)
g	Gap between elements (with primary (p) or secondary (s) components)
A	Complete array aperture

S	Signal amplitude (active and reference components)
x	Secondary imaging axis
y	Primary imaging axis
z	Depth imaging axis
τ	Time of Flight (with various components)
I	Image intensity (2D or 3D)
θ_{pixel}	Pixel window angle
W	Pixel windowing parameter

Chapter 1

Introduction

Non-Destructive Evaluation (NDE) plays an essential part of the maintenance schedule commissioned to assess the integrity of operational plant. Ultrasonic Testing (UT) is one of the major NDE techniques used, valued for its ability to volumetrically interrogate a component [1]. Significant advances in the technology associated with UT have been realised in recent years. Key developments include the introduction of ultrasonic arrays, novel signal processing algorithms and new approaches for harnessing computer power. Until now these factors have mainly been considered independently, leaving a complete inspection system encompassing each of the developments yet to be formed. This Chapter introduces the motivation behind the work presented in this Thesis, detailing the objectives of the study and the author's contribution to the field.

1.1 Commercial Motivation

The motivation for this study was established through a combination of industrial and academic partners. The research was completed through an Engineering Doctorate (EngD) scheme under the UK Research Centre for Non-Destructive Evaluation (RCNDE). The aim of the Centre is to move NDE into the 21st century, by performing industrially relevant, forward thinking research. The industrial sponsor of this work was Doosan Babcock, a specialist in fabrication, maintenance and extension of industrial plant life. The academic partner was the Centre for Ultrasonic Engineering (CUE) at the University of Strathclyde.

Doosan Babcock's vision is to be a global leader in asset support. In order to achieve this they are continuously aiming to increase the skill of their personnel, as well as keeping up to date with state of the art equipment and inspection techniques. One key area of Doosan Babcock's asset support focus is NDE, with particular applications in nuclear, oil and gas, and petrochemical plant. To allow

Doosan Babcock to remain competitive in this area it must commit to ongoing research and development, invest in new technology and respond to the market requirements.

The NDE group within Doosan Babcock identified numerous recent advances in technology associated with UT. It was perceived that they could significantly improve various complex inspections currently being performed. More specifically, developments in innovative signal processing algorithms and sparse 2D arrays offered potential in developing a solution for the efficient inspection of complex, arbitrary surface components. Considerable expertise on these specific topics were recognised at various academic partners of RCNDE. Doosan Babcock therefore decided to pursue an EngD project focused on combining advances in arrays, signal processing and computer technology to develop an efficient inspection for complex components.

Performing research in this way allowed Doosan Babcock to draw upon the broad expertise of academics within CUE, and wider partners of RCNDE. This avenue also leads to an expert in the field that is integrated within the company, as opposed to sponsoring academic research alone. The success of this work has paved the way for Doosan Babcock to further develop a new inspection technique to replace some of the most complex and labour intensive inspections that are currently performed. Technology transfer has successfully been exploited through this study, opening the door to the future of efficient inspections for Doosan Babcock. There are currently no qualified inspections using FMC/TFM and the findings of this Thesis will now be extended with the aim of producing a qualified inspection procedure suitable for nuclear plant.

1.2 Technical Context

The objective of this research is to adopt advances in UT technology to form an efficient inspection for complex components. A number of key aspects contribute towards developing such an inspection and they are considered throughout this Thesis. Figure 1.1 illustrates the key components of this study and indicates how they are related in an efficient inspection system.

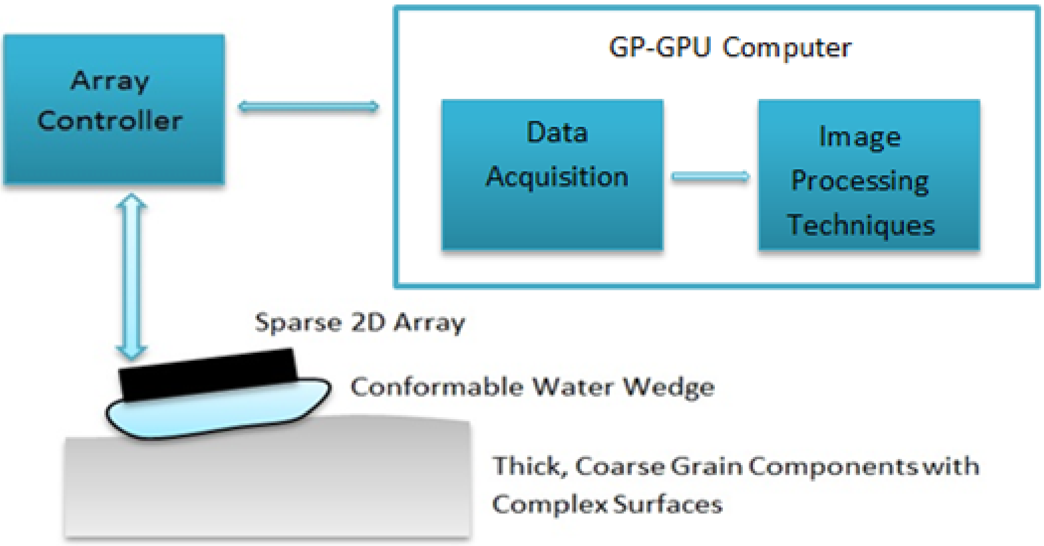

Figure 1.1: Overview of the key components involved in reaching an efficient inspection system for complex components.

The focal point of this study is the complex components for which an efficient inspection technique is desired. In the context of this Thesis complex components are defined as components requiring UT that present an irregular surface form due to welding or machining processes. In particular, this relates to components typical of the primary circuit pipework in nuclear plant. Such components are generally thick section, between 40mm and 100mm, coarse grain 304 stainless steel. The surface of such components is ground smooth after any welding or machining, removing any surface roughness but potentially resulting in undulations on the surface. The surface height is estimated to vary up to 2mm in height over any 60mm region and it is intrinsically difficult to represent such variations on component drawings. Surface roughness is not a factor in this work due to the smooth surface preparation.

UT of such components is currently performed using a combination of conventional probes and requires lengthy data analysis by a highly skilled operator. The process is therefore extremely dependent on the operator and repeatability is difficult to achieve, it is also time-consuming and therefore costly. An efficient inspection technique harnessing recent advances in UT technology could potentially reduce the dependence on the operator, significantly reducing the time required for data analysis, while providing a reliable and repeatable evaluation of such components.

The key aspects that contribute towards an efficient inspection system for complex components include economical execution of novel signal processing algorithms, advanced data acquisition hardware and innovative probe designs. This Thesis aims to combine each of these factors to develop an inspection technique suitable for complex components.

Various commercially available Phased Array Controllers (PAC) and software packages have emerged in recent years. Significant advances in the electronic components used in PACs have allowed for efficient data collection and transfer from the PAC to computer. Modern PAC typically offer 32 to 128 channels, suitable for powering arrays of equal number of elements.

1.3 Bespoke Test Block

A bespoke test block was designed to aid the development of an inspection suitable for complex components. It presents a representative surface profile and contains six 3mm Side Drilled Holes (SDH) to be used as calibration reflectors. Additionally, it contains five angled 6mm slots that are used in the final evaluation of the inspection system. The SDH and slots are standard reflectors used to assess the performance of the inspection and correspond with the size of defects that would require detection in an inspection. Figure 1.2 shows this test block with the SDH and slots and further information is available in Appendix A. The interface and Back Wall (BW) are also indicated on the image for reference. This test block is used throughout this Thesis to demonstrate and evaluate aspects of the inspection system.

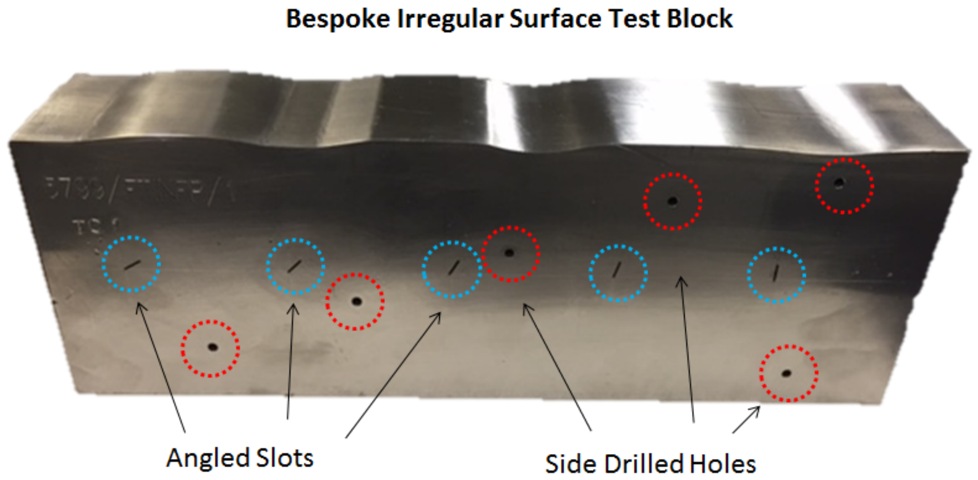

Figure 1.2: Bespoke test block used throughout this Thesis, showing the irregular surface form, SDH and slots.

1.4 Objectives

A number of objectives were set in an effort to reach an efficient inspection of complex, arbitrary surface components. First, consideration on recent advances in the field were made. One major development was recognition of the Total Focusing Method (TFM) as the gold standard in ultrasonic imaging [2]. Furthermore, CUE had developed an extremely efficient implementation of TFM using General Purpose Graphic Processing Units (GP-GPU). This move towards a real-time execution of TFM paved the way for its application for intricate imaging scenarios.

The overall aim of this research was to adapt TFM for efficient inspection of complex components. A number of sub-objectives were identified to aid reaching the final goal:

- Progress the development of TFM accounting for refraction through an arbitrary interface.
- Develop a method for accurately extracting and reconstructing arbitrary surface profiles.
- Design and manufacture a sparse 2D array suitable for inspecting thick section stainless steel.
- Consider automation of the inspection of complex components using TFM and sparse 2D arrays.
- Formulate a method to evaluate the sensitivity in inspection of complex components using TFM and sparse 2D arrays.
- Consider application of this technique to an example component.

1.5 Contribution to Knowledge

In achievement of these objectives this Thesis documents several contributions to the field. The nature of an EngD means contribution to knowledge is demonstrated through scientific advances in the field and technology transfer to the industrial partner.

1.5.1 Scientific Knowledge Contribution

First, through a thorough understanding of the calculations involved in TFM, a routine for dealing with refraction through an arbitrary surface was developed. Dziewierz [3] and Lardner [4] led this advance in TFM, and the author assisted in the progress and implementation by working with these researchers to achieve the end goal. The author suggested that the most suitable method for defining the surface profile was by a grid of discrete points appropriate for interpolation. Furthermore, the author propelled the algorithm to be extended to handle surface profiles varying in all directions. Previous to this the TFM algorithm had only been demonstrated on surfaces varying in two axes. This is a substantial development towards industrial inspection with TFM, since components that have endured machining will vary in all axes.

Another significant contribution from this Thesis arises from the dynamic surface detection technique. While various other studies have addressed inspection of complex components of a known surface [5–7], this study focused on developing a robust and reliable method for detecting surfaces representative of in-service components. Such components have often undergone welding and subsequent machining which results in a smooth, undefined surface form. Typical curve fitting methods are not suitable for such geometries and so a new detection and reconstruction scheme is developed. This technique is successfully demonstrated to high accuracy on a purpose-designed test block. Supplementary demonstrations of TFM for inspection of complex components is achieved through ultrasonic modelling packages.

Further contribution to the field is achieved through investigation of inspection sensitivity when using sparse 2D arrays and TFM. This is particularly relevant to industrial applications due to the stringent requirements on inspection calibration. Data analysis techniques typically rely on predictable, reliable amplitudes and responses from any expected flaws. Current ultrasonic imaging methods make use of Distance Amplitude Correction (DAC) curves to regulate the response from defects over distance from the ultrasonic probe. However, this method would be computationally demanding and complex to employ in the case of undefined surface profiles, only becoming more challenging when employing new methods such as Full Matrix Capture (FMC) and TFM.

The ability to further enhance the efficiency of inspection is achieved through the design of a sparse 2D array. Volumetric imaging is one main advantage of 2D arrays but they are yet to be used widely due to design constraints applying to matrix arrays. Alternative designs encompassing random element distributions have been shown to offer equivalent imaging performance to matrix arrays, with a fraction of the elements [8]. A sparse 2D array was designed and successfully implemented for the efficient inspection of complex components, assisted by review of a prototype device.

1.5.2 Technology Transfer

Each of the scientific advances resulting from this Thesis contribute towards the initiation of a technique suitable for efficient inspection of complex components. Advanced signal processing algorithms have been adapted to efficiently handle refraction through an irregular surface. Dynamic detection and reconstruction of representative surfaces is demonstrated to high accuracy. Furthermore, this study highlights the use of sparse 2D arrays for enhancing inspection efficiency. Additional factors such as automation of the technique, image stitching, data collection, processing time and storage requirements are addressed. Ultimately the constituent components of this research are formed into an inspection technique that is demonstrated on an example component.

The author has addressed scientific challenges with industry in mind and these developments have been introduced to the industrial partner through technology transfer. This places the industrial partner in an ideal position to further develop and implement a replacement inspection for complex components. The work demonstrated in this Thesis provides the industrial partner with invaluable access to knowledge and technology that would be difficult to acquire otherwise.

1.6 Publications

The author has presented the findings from this work at two relevant, highly regarded conferences throughout the EngD. The following have been published in the proceedings of these conferences.

The author was presented with the William Gardner Award at BINDT 2014, for the best paper published in the Proceedings of the Institute's Annual Conference NDT 2014 by a person in the early stages of their career.

- A. McGilp, J. Dziewierz, T. Lardner, J. Mackersie and A. Gachagan, 'Inspection design using 2D phased array, TFM and cueMAP software', 40TH Annual Review of Progress in Qunatitative Nondestructive Evaluation, (Vol. 1581, No. 1, pp. 65-71). 2014, February. AIP Publishing.
- A. McGilp, J. Dziewierz, T. Lardner, A. Gachagan, J. Mackersie and C. Bird, 'Inspection of Complex Components using 2D Arrays and TFM', 53rd Annual Conference of the British Institute of NDT, 2014.

1.7 Thesis Structure

This structure of this Thesis aims to follow the methodology of adapting FMC and TFM for efficient inspection of complex components. The layout follows a typical technical procedure, starting with consideration of background theory and literature, followed by detailed analysis of the techniques applied, and concluding with the results of the research.

The Introduction given in this Chapter aims to present the EngD scheme and the motivation of the industrial sponsor to fund this research. The Introduction also sets out to clearly specify the objectives of the research presented in this Thesis, while specifying the author's contribution to the field.

The fundamental physics that provide the foundation of ultrasonic imaging is presented in Chapter 2. The development of UT from conventional probes through to phased arrays is presented. Gaps in current technology that are preventing widespread application of FMC, TFM and 2D arrays in industrial NDE are studied. The aim of this Thesis is to address these factors in a move towards achieving an efficient industrial inspection of complex components using TFM and 2D arrays.

A detailed breakdown of the calculations involved in realising an extremely efficient implementation of TFM is given in Chapter 3. The key aspects of employing GP-GPUs for this implementation are explored. Furthermore, the factors involved in extending TFM from a basic, single-medium, scenario to inspection of 3D arbitrary surface components is described. This Chapter forms the basis for the imaging algorithm and methodology to be applied throughout the work presented in this Thesis.

Chapter 4 details a procedure for dynamically detecting and then reconstructing arbitrary surface profiles. Various parameters are considered in order to establish a robust and reliable surface extraction. A number of curve fitting algorithms are also assessed for their ability to accurately reconstruct the surface. Comparison is made between the detected and true profiles. Detailed error analysis is performed to ensure the profile obtained is truly representative of the component.

Sparse 2D arrays are explored to further enhance the efficiency of the inspection in Chapter 5. The process followed to design and fabricate a prototype array is documented. A number of lessons are learnt upon evaluation of the prototype array, leading to a revised design. This improved final design of a sparse 2D array of 2MHz operating frequency is then evaluated on a purpose designed calibration block.

The constituent parts of the inspection system are brought together to form an automated inspection technique which is evaluated in Chapter 6. Automation of the inspection is considered, along with ensuring it is industrially robust, while assessing its repeatability and reliability. A procedure for establishing the relative sensitivity in inspection of complex components using FMC and TFM is formed. This is essential for industrial use of TFM and sparse arrays since defect detection and characterisation is highly dependent on the calibration of an inspection system. Finally, the inspection system is evaluated for its suitability to an example target component.

The conclusions of the work detailed in this Thesis are summarised in Chapter 7, with reference to technology transfer. An indication for possible work that would complement this research is also presented.

Chapter 2

Fundamentals of Ultrasonic Imaging Theory

Ultrasonic Testing is one of the major NDE methods used in industry [9]. It has been widely used since its introduction in the mid 20th century with its success due mainly to the ability to volumetrically inspect components. The fundamental theory behind ultrasonic wave propagation in a structure is explored in this Chapter. The features of probes commonly used in industrial UT, along with typical imaging conventions, are discussed. Finally, the current inspection of complex components, typical of the primary circuit in nuclear power plant, is reviewed. A solution for an efficient inspection system for such components is sought through the exploitation of innovative probe designs and advanced imaging algorithms.

2.1 Ultrasonic Wave Propagation

Ultrasonic imaging is a term used to describe interrogation of a body using acoustic energy of frequency greater than 20kHz. The practice was initially developed in Sound Navigation and Ranging (SONAR) [10], where it was employed to identify objects in water thus allowing vessels to navigate safely. Extensive research into ultrasonic wave propagation ensued and NDE using ultrasound to examine the structure of solids was established [11]. Along with the industrial developments, the use of ultrasound in medicine also evolved in both diagnostic and therapeutic applications [12]. Despite the diversity in these practices, they collectively rely on useful information about a medium being obtained through the propagation of ultrasound within it.

Considering conventional pulse-echo UT, an ultrasonic wave is transmitted into a component and is partially reflected upon interaction with the internal structure where there is a change in acoustic impedance [13]. The response can be analysed, and then used to construct an image of the internal structure of the component.

Figure 2.1 illustrates this, where the response is recorded as a time-amplitude signal [14]. Two indications are visible, one due to reflection from the Back Wall (BW) and the other from a flaw in the component. The arrival time, t, and amplitude of the reflected signals can then be used to interpret the structure using the acoustic velocity, c, where the distance travelled, d, is determined by Equation 2.1.

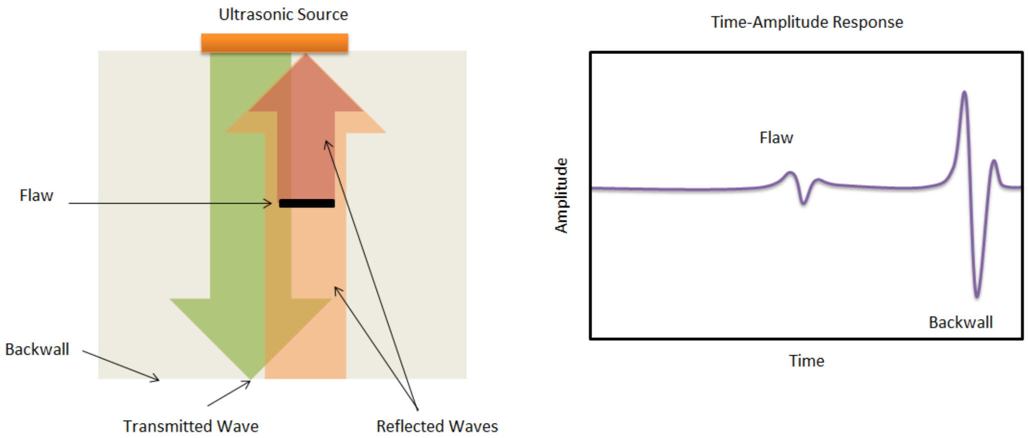

FIGURE 2.1: Ultrasonic beam transmitted and reflected in a structure containing a flaw. The time-amplitude response shows a small indication due to partial reflection from the flaw, and a large signal reflected from the BW of the component.

$$d = \frac{ct}{2} \tag{2.1}$$

Ultrasonic waves propagate with an associated amplitude and direction [13]. They propagate in various modes, of which the most widely used in NDE are longitudinal and shear waves. Longitudinal waves are referred to as compression waves, as they induce oscillation of the structure's particles in the direction of the wave propagation. Conversely shear, or transverse, waves cause particles in a solid to oscillate perpendicularly to the wave propagation.

The mode of propagation is determined by the ultrasonic source and the properties of the material through which the energy travels. These propterties include the density (ρ), Young's Modulus (E), Poisson's Ratio (μ) and acoustic velocity (c). Subsequently, the velocities of longitudinal (c_l) and shear (c_s) waves differ as determined by Equations 2.2 and 2.3 respectively [13]. As a general approximation, longitudinal wave velocities are around double those of shear waves.

$$c_l = \sqrt{\frac{E(1-\mu)}{\rho(1+\mu)(1-2\mu)}} \tag{2.2}$$

$$c_s = \sqrt{\frac{E}{2\rho(1+\mu)}} \tag{2.3}$$

Furthermore, the frequency (f) and wavelength (λ), of the ultrasound also influence ultrasonic propagation. They are related to the acoustic velocity through Equation 2.4.

$$c = f\lambda \tag{2.4}$$

Attenuation of the ultrasonic energy occurs as it propagates through a medium, thus the amplitude of the wave is reduced as a function of distance. The two main causes of attenuation are absorption over distance and scattering due to interactions with the internal structure of the medium [15]. Attenuation arising due to absorption increases with inspection range and operating frequency, as the ultrasonic energy is converted to heat through vibration of the material particles. Additionally, attenuation due to scattering occurs when the size of the grains in the propagation medium are comparable with the ultrasonic wavelength. This interrupts the intended propagation path as near specular reflection from the grain occurs, and causes the energy to scatter in various directions. Where the wavelength is much greater than the grain size diffuse scattering occurs, where little to no energy is scattered due to the grain. Both types of attenuation can therefore be curtailed by reducing the inspection frequency, which in turn increases the wavelength. However, the inspection resolution and sensitivity are consequently decreased, meaning that a compromise is generally required in practice.

2.1.1 Dual Media

It is common in UT for ultrasound to travel from one medium to another, and a number of effects are observed at the boundary between the two. Firstly, the amplitude of the ultrasonic energy is affected due to a change in the acoustic impedance (Z_a). Consider an ultrasonic wave passing through one medium to another, crossing an interface. Assuming the two media are not identical, their acoustic impedances will be different which initiates a reflected and transmitted wave at the boundary. As defined by Equation 2.5, the acoustic impedance is a function of density (ρ) and acoustic velocity (c).

$$Z_a = \rho c \tag{2.5}$$

Where the wave is at normal incidence to the boundary, the transmission (T_c) and reflection (R_c) are given by Equations 2.6 and 2.7 respectively [13]. Here Z_{a1} and Z_{a2} are the acoustic impedance of the first and second medium respectively. These coefficients represent the ratio of transmitted and reflected energy at the boundary.

$$T_c = \frac{4Z_{a1}Z_{a2}}{(Z_{a1}+Z_{a2})^2} \tag{2.6}$$

$$R_c = \left(\frac{Z_{a1}-Z_{a2}}{Z_{a1}+Z_{a2}}\right)^2 \tag{2.7}$$

Where normal incidence is not achieved, refraction occurs at the boundary. The incident and refracted beam angles are related through Snell's Law [16], as in Equation 2.8. This scenario is illustrated in Figure 2.2, where the refracted angle (θ_2) is determined by the ratio of velocities, in medium 1 (c_1) and 2 (c_2) and incident angle (θ_1).

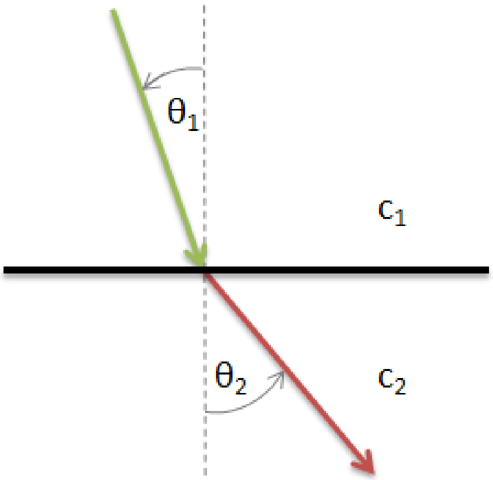

FIGURE 2.2: Illustration of refraction through an interface, as defined by Snell's law.

$$\frac{\sin(\theta_1)}{\sin(\theta_2)} = \frac{c_1}{c_2} \tag{2.8}$$

Furthermore, mode conversion can occur where a longitudinal wave converts to a shear wave [17] due to the incident angle. The angle at which mode conversion occurs can be predicted by substituting the shear velocity of medium 2 into Equation 2.8. An angle referred to as the first critical angle, depicts the incident angle at which only shear waves remain in medium 2. In a typical water to steel configuration, shear waves are generated at incident angles around 10° and become the dominant wave mode at incident angles above 30°. The refracted angle is therefore split into a longitudinal (θ_{2l}) and shear (θ_{2s}) component, for incident angles between 10 and 30°.

The transmission and reflection coefficients are also a product of the incident and refracted angle, since they must take account of more than one wave mode. Figure 2.3 demonstrates the effect of mode conversion on the transmitted and reflected wave. The transmission coefficients are separated into a longitudinal (T_{cl}) and shear (T_{cs}) component, given by Equations 2.9 and 2.10 respectively [13].

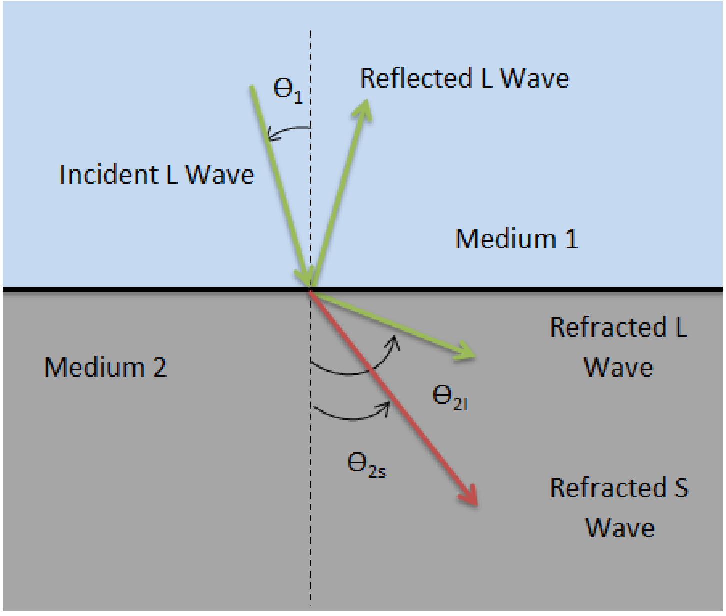

FIGURE 2.3: Illustration of mode conversion, arising from an incident beam at a boundary other than normal incidence.

$$T_{cl} = \frac{\rho_1}{\rho_2} \frac{2Z_{a2l} \cos(2\theta_{2s})}{Z_{Ra1} + Z_{Ra2}} \tag{2.9}$$

$$T_{cs} = \frac{\rho_1}{\rho_2} \frac{2Z_{a2s} \sin(2\theta_{2s})}{Z_{Ra1} + Z_{Ra2}} \tag{2.10}$$

Assuming a liquid to solid configuration, the densities of medium 1 and 2 are given as ρ_1 and ρ_2, while c_{2l} and c_{2s} are the longitudinal and shear velocities in medium 2. In addition, Z_{a2l} and Z_{a2s} are the longitudinal and shear components of the acoustic impedance in medium 2, given by Equations 2.11 and 2.12.

$$Z_{a2l} = \frac{\rho_2 c_{2l}}{\cos(\theta_{2l})} \tag{2.11}$$

$$Z_{a2s} = \frac{\rho_2 c_{2s}}{\cos(\theta_{2s})} \tag{2.12}$$

Accounting for refraction, the acoustic impedance in medium 1 is then Z_{Ra1} and the combined acoustic impedance in medium 2 is Z_{Ra2}, as in Equations 2.13 and 2.14.

$$Z_{Ra1} = \frac{\rho_1 c_1}{\cos(\theta_1)} \tag{2.13}$$

$$Z_{Ra2} = Z_{a2l} \cos^2(2\theta_{2s}) + Z_{a2s} \sin^2(2\theta_{2s}) \tag{2.14}$$

These coefficients are particularly important in developing a relative sensitivity map for inspections utilising FMC and TFM, as will be explored in Chapter 6.

In NDE the ultrasonic source is typically referred to as a probe, or transducer. The quality of an inspection is determined by a combination of the probe, imaging method and the component's material properties [18].

2.2 Ultrasonic Transducers

In NDE, the ultrasonic field is generated by a transducer containing an active piezoelectric element [19]. Certain materials, such as lead and quartz, exhibit the ability to convert an electrical voltage into a mechanical vibration and vice versa due to the piezoelectric effect. The thickness T_p of the piezoelectric material determines the resonant frequency (f) of the transducer, given by Equation 2.15.

$$f = \frac{c}{2T_p} \tag{2.15}$$

Traditionally, probes consisted of a single or dual element held within a probe housing. A schematic and photograph of a conventional probe is shown in Figure 2.4. They are typically comprised of the active piezoelectric material between a damping material at the back and a protective matching layer, sometimes referred to as the shoe, on the front. The active layer is the piezoelectric element that generates the mechanical vibrations and it is surrounded on either side by acoustically matched layers that optimise the performance of the element. The damping material on the back of the probe controls how long the active element vibrates for, known as the ring down time. It is also used to attenuate any energy travelling backwards in the probe housing and avoid any internal reverberations. A matching layer is often present on the front of the probe which acts as protection for the fragile active element and also aims to acoustically match the active layer to the load medium. Matching layers are generally of thicknesses in the order of $\lambda/4$ and typically fabricated from epoxy resins with some metallic additive. The aim of the matching layer is to optimise the acoustic energy being transferred from the probe to the inspection medium [20].

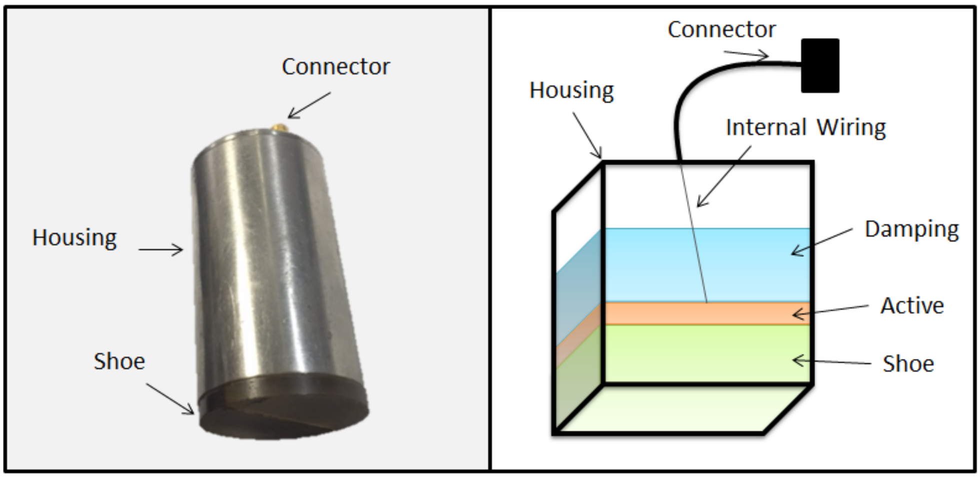

Figure 2.4: Photo (left) and schematic (right) of a conventional ultrasonic probe used in NDE.

Such probes would either be used for Pulse-Echo (P-E), where the element both transmits and receives, or Pitch-Catch (P-C), where one element Transmits (Tx) and the other Receives (Rx). Figure 2.5 illustrates P-E and P-C configurations, along with a probe on an angled shoe. An electrical excitation pulse is applied to the transmitter in the probe which generates a vibration within the piezoelectic material. This vibration is transferred to the inspection medium and effectively initiates ultrasonic wave propagation in the medium.

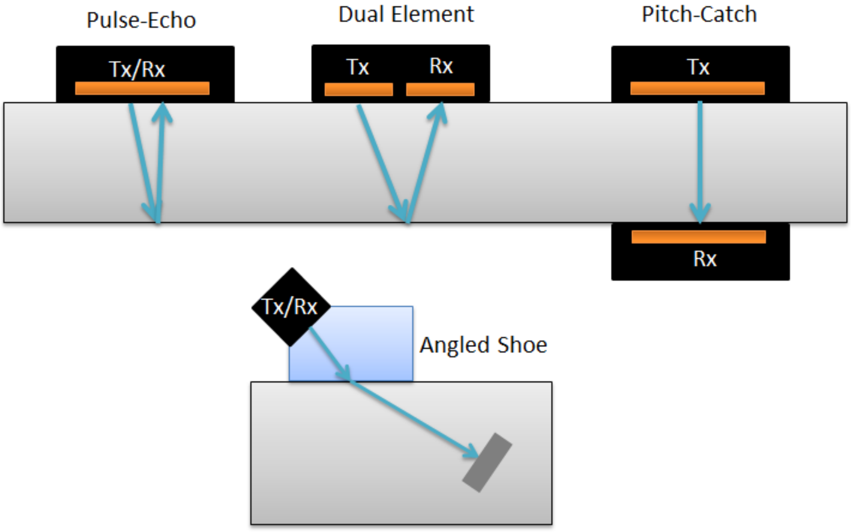

FIGURE 2.5: Demonstration of P-E, P-C and angled conventional probes.

The formation of the beam is determined by the size of the ultrasonic source, as well as the operating frequency and wavelength in the medium. A schematic and model of the ultrasonic beam assuming the diameter of the source is much larger than the wavelength are shown in Figure 2.6 and 2.7. There are two main regions observed as the beam extends with range, the Near Zone (Nz) and Far Zone (Fz). In the near zone, or Fresnel region the ultrasonic energy is fluctuating due to constructive and destructive interference. Beyond this, in the far field, or Fraunhofer region, the beam is stable and constantly diverging with range. The boundary between the near and far zones can be approximately calculated by Equation 2.16. Where R_{Nz} is the range of the Nz and D is the diameter of the ultrasonic source.

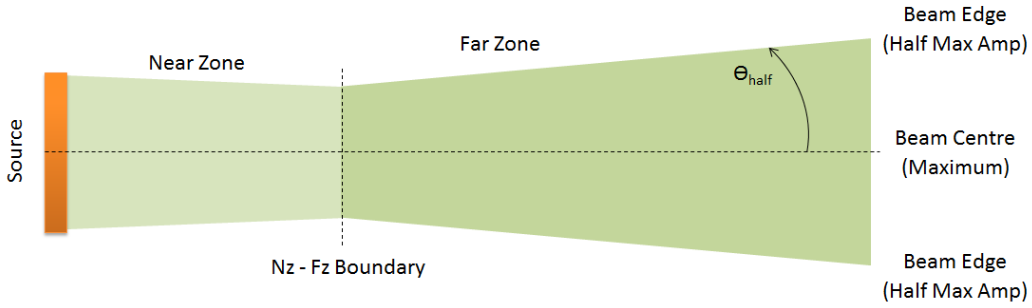

FIGURE 2.6: Diagram showing the ultrasonic beam shape, with the Nz boundary and beam spread visible.

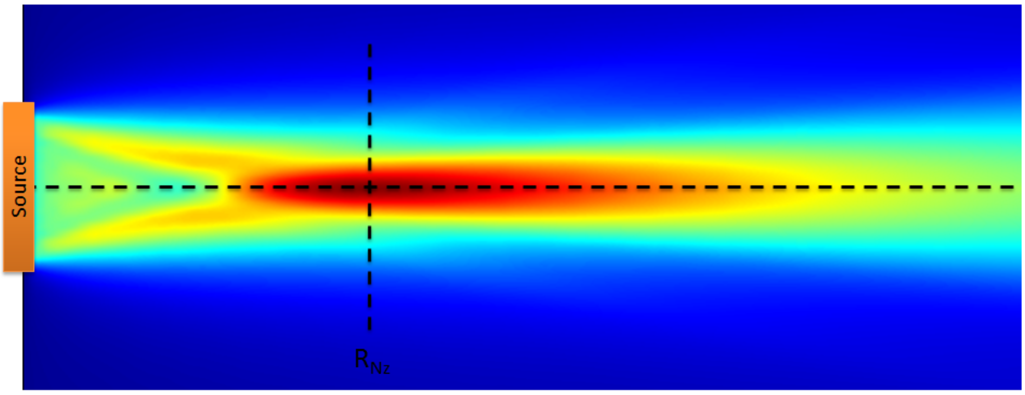

FIGURE 2.7: Ultrasonic beam simulation showing the Nz boundary, where red denotes high amplitudes and blue low.

$$R_{Nz} = \frac{D^2}{4\lambda} \tag{2.16}$$

Where the probe is operating in P-E, a small dead zone is present while the probe is ringing down from the initial pulse. This occurs due to the electrical signal that is initially applied to the piezoelectric material. The element vibrates due to this voltage being applied and it cannot detect features in signals being returned until it returns to equilibrium.

The amplitude of the ultrasonic beam peaks on the centre line, and gradually reduces as the beam diverges. The amplitude of the beam at angles spreading out from the central maximum can be determined using Equation 2.17, where θ_{half} is measured from the centre line of the beam to the edge at a certain amplitude. The factor k is specified according to the required amplitude and shape of the source, for example k is 0.51 for disk shaped sources and half the maximum amplitude [13].

$$\theta_{half} = \sin^{-1}\left(\frac{k\lambda}{D}\right) \tag{2.17}$$

An effect of beam divergence is a trend referred to as the inverse power law. It conveys the decrease in ultrasonic energy over range, due to the increase in area over which the beam is spread. It is inversely proportional to the distance travelled.

The natural focus of conventional ultrasonic transducers occurs at the edge of the near zone, R_{Nz}. Imaging in the near zone is not recommended due to undulations in the ultrasonic energy. Most inspections are therefore performed in the far field, where the response from abnormalities is predictable. When considering ultrasonic arrays imaging is typically performed in the far zone of each element where the energy is predictable, this may relate to the near zone of the overall aperture in large arrays.

A probe shoe, or wedge, is often used to angle a longitudinal probe such that it instigate mode conversion in the inspection medium. Some of the most popular wedges produce 45°, 60° or 70° shear waves in steel, while 0° longitudinal probes are also common. These angles are chosen to achieve near normal incidence with any expected flaws which would maximises their response in an inspection. This generates a specular reflection from the defect, where the energy is directed back in the direction from which it came. However, it is not always possible to achieve a specular response, and tip diffraction may be utilised instead. In this case, energy is reflected in various directions from the indication and as such, the signal amplitude is typically lower. A simple example of each of these responses is given in Figure 2.8, where green indicates the incident wave and orange is the reflected wave.

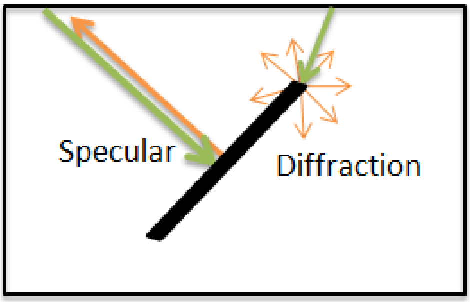

Figure 2.8: Example of specular reflection and tip diffraction occurring when an ultrasonic wave is incident on a flaw.

The wedge is often built into the probe housing, meaning it cannot be changed with ease. This restricts a single probe to one predetermined inspection angle, meaning they lack flexibility in practical applications. Consequently this means that a number of probes are required to achieve the desired coverage in an inspection [21].

In order to image a component conventionally, a probe is moved incrementally and the time-amplitude response is collected at each position. This is referred to as an A-Scan in NDE. An image of the component can then be built up by lining the A-Scans vertically, and converting the amplitude to a colour map. An example of this process is shown in Figure 2.9, using the arrangement in Figure 2.1. Here the probe is moved incrementally along the block from left to right, and A-scans are recorded at each position. Low amplitudes are generally indicated by blue, evolving through to high amplitudes in red. The BW is observed across the full block, while the extent of the flaw is visible in the central A-scans.

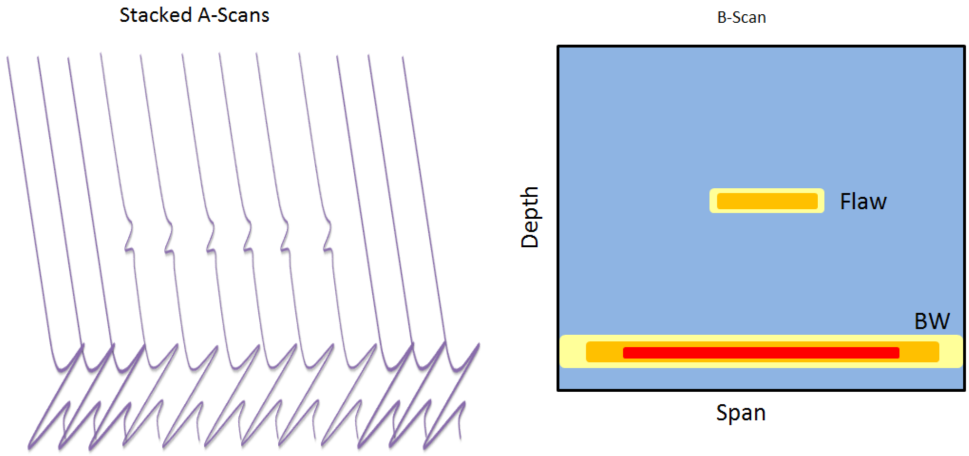

FIGURE 2.9: An example of the formation of a B-scan, using stacked A-Scans.

In order to achieve the required volumetric coverage, an assortment of probes is typically scanned over the component. This can mean that the inspection is repeated numerous times, and analysis of the data is performed for each probe individually. Finally, agreement between all probe inspections should be achieved to complete the inspection. This can be extremely time consuming, and thus expensive.

2.2.1 Arrays

Significant advances in manufacturing, electronics and computing technology have paved the way for the introduction of ultrasonic array transducers [22]. In principle they are equivalent to a group of small conventional probes, and hence offer a number of advantages. The main benefit of arrays is their ability to perform the job of numerous conventional probes. This means that equivalent inspections can be performed in a fraction of the time, since changing probes and repetition of scan plans is avoided. Consequently, through the addition of beam steering and signal processing it is anticipated that inspection data would be easier to interpret. Each of these factors mean notable reductions in time and cost for ultrasonic inspection. These benefits are deliberated against the fact that advanced instrumentation, training and inspection procedures are required for implementation.

Various array formations are possible, however linear arrays are the most widely used and are considered here first. A schematic of a 1D array is shown in Figure 2.10, with rectangular elements stacked vertically. Each element has a width (w) and length (L), separated by a gap (g). The pitch (p) combines the element width and gap in one measurement. The complete aperture size (A) is a measure of all elements in the array.

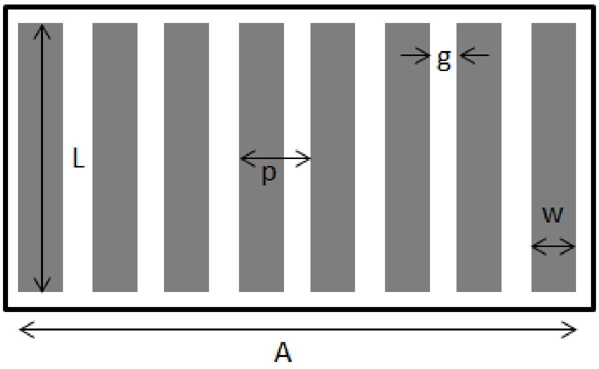

Figure 2.10: Schematic of the dimensions in a linear array, with stacked rectangular elements.

It is not always necessary for all elements in an array to be operational at once, which gives rise to an active aperture. The principles defined for conventional probes, also apply for formation of the ultrasonic beam with arrays. Instead of each individual element, the active aperture of the array dictates Nz and beam divergence using the previously defined relations.

Ultrasonic arrays are often referred to as phased arrays, as the beam they emit can be controlled by phasing the excitation of each element in the array [23]. This offers greater control over the beam formed by an array, compared with conventional probes. Two main uses for phasing the elements include controlling beam direction, and focusing at a specific range. Figure 2.11 demonstrates how phasing the excitation of each element can steer and focus the beam. In the case of beam steering, the time of excitation for each element is determined to produce a combined wave at the desired angle. Similarly, where focusing is requested, each element is pulsed such that their respective wavefronts arrive simultaneously at the specified range. Focusing is only possible in the near zone of the active aperture of the array.

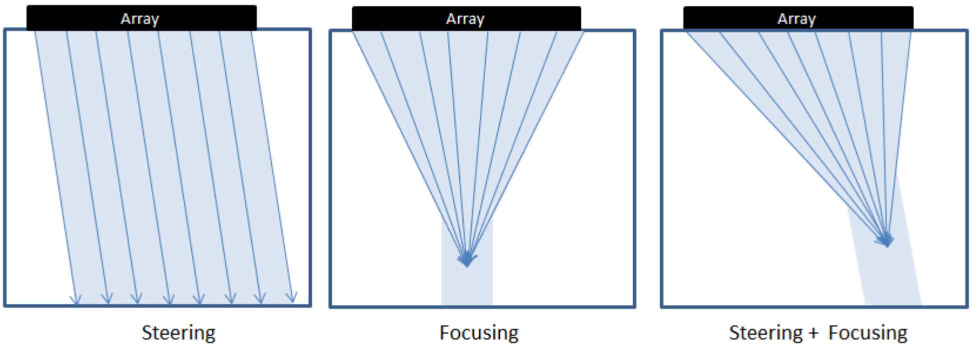

FIGURE 2.11: Phasing the excitation of elements in an array allows control over the angle of the overall beam, including steering and focusing.

Undesirable grating lobes due to spatial aliasing [24] can be generated when performing beam steering with arrays. They occur where the pitch between elements is equal to integer multiples of the wavelength and arise when steering the beam away from the natural angle due to the energy spreading out from the main beam. They can be avoided by maintaining a pitch of less than $\lambda/2$, and the amplitude of the grating lobe for pitches between $\lambda/2$ and λ is determined by the probe design and steering angle. Grating lobes often appear as a high amplitude beam in addition to the main beam, an example of this is shown in Figure 2.12. The maximum energy of the main beam reduces with increased steering angles, meaning the grating lobe becomes larger in relation to the main beam. This additional lobe can cause spurious signals, and should therefore be avoided where possible.

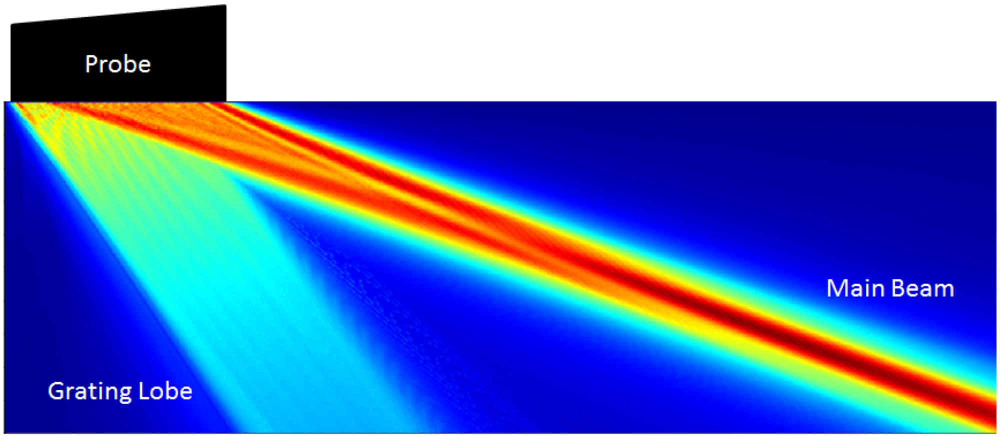

FIGURE 2.12: Simulation of an ultrasonic beam, where the main beam is present together with a lower amplitude grating lobe.

Array design often requires a compromise between various factors, including the array dimensions, operating frequency and sensitivity to flaws. It is therefore imperative to understand what is required of the inspection, and meeting this criterion as closely as possible. In general, large elements are most sensitive, however they must remain small compared with the wavelength to avoid narrow beam spread and grating lobes. The operating frequency is also constrained by the component material properties. It must be high enough to provide a reasonable resolution but sufficiently low to avoid excessive attenuation.

A number of array configurations are commercially available [25], and 2D matrix arrays are important with respect to this Thesis. The factors discussed so far for linear arrays extend to 2D configurations. Matrix arrays offer additional beam steering possibilities over linear arrays, inspiring their use in NDE and biomedicine. The elements are generally configured as a rectangular matrix, over a primary and secondary axis as shown in Figure 2.13. Now the element width, pitch and gap each have a primary and secondary component. This means that steering and focusing can be performed in both axes. Additionally, a volumetric image can be obtained from a single position [26]. However, the design restrictions outlined for linear arrays, also apply to 2D arrays. This means the number of elements required to achieve an equivalent 2D array is vastly increased compared with a linear array.

Despite the possible advantages they offer, they are not widely used in industrial NDE and have instead largely remained a topic for research thus far. Volumetric imaging can effectively be achieved by mechanically moving a conventional probe or linear array. Additional electronics coupled with substantial computational requirements would be required in order to achieve equal imaging performance with a 2D array.

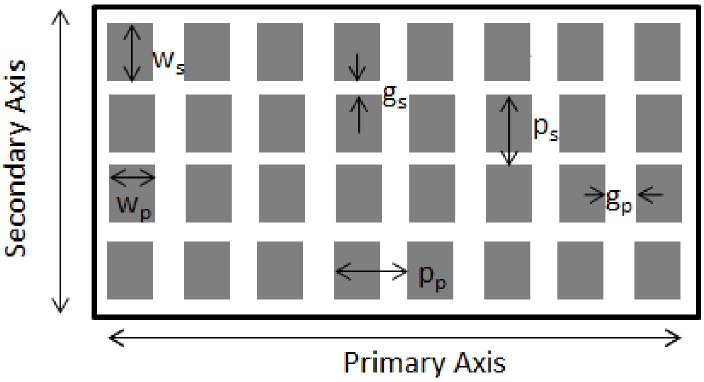

FIGURE 2.13: Schematic of 2D array, with elements arranged in a matrix with a pitch, element width and gap in both the primary and secondary axes.

An alternative layout for 2D arrays is therefore sought to minimise the number of elements over the aperture, without reduction in the imaging performance. The design and implementation of sparse 2D arrays is demonstrated in Chapter 5, aiding efficient volumetric imaging of complex components.

The design and selection of the probe plays a key role in ultrasonic inspections, as good quality data is required to provide optimal imaging performance.

2.3 Ultrasonic Inspection

The result of an ultrasonic inspection can be imaged in various ways. When using either conventional probes and arrays, the data is typically arranged into a B-scan, C-Scan and D-Scan. They portray a slice through the component, a top view and an end view respectively, as illustrated in Figure 2.14. Each of these views convert amplitude to colour, and a volumetric representation of the inspection can be constructed by considering all views. The A-scan is also routinely used, as it provides the raw amplitude response. The probe is typically moved in two directions, labelled the primary and secondary axes. When arrays are employed, the primary axis of the inspection is typically in line with the primary axis of the probe.

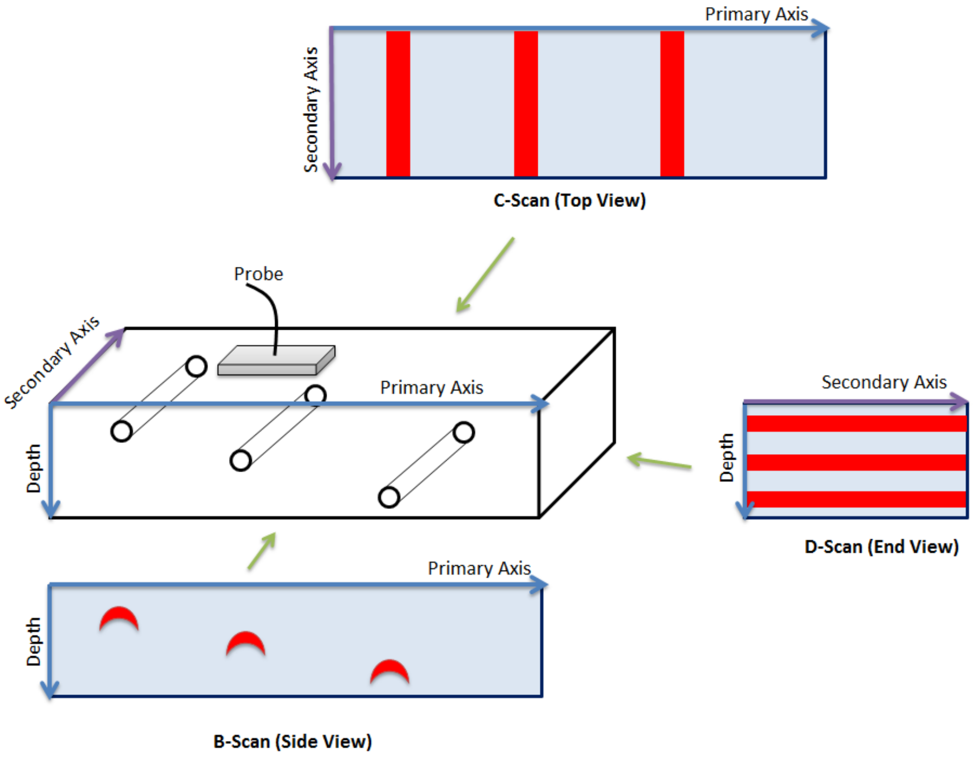

FIGURE 2.14: The typical views used in ultrasonic imaging, with B, C and D scans showing the side, top and end view respectively.

Furthermore, arrays can perform sectoral scans, where the beam is swept through a range of angles, instead of just one. This is achieved by specifying numerous focus points instead of one, as in Figure 2.15. Each of these array imaging systems make use of delay laws, which are a set of excitations for each element at specific times. The response is then summed upon reception, while taking account of the appropriate delays. This delay and sum approach is generally the technique applied when imaging with arrays. In more involved inspection scenarios where numerous angles or focus depths are required, the calculation and application of delay laws becomes increasingly complex, and therefore computationally intensive and time-consuming. These factors limit the functionality of inspection using arrays, and ultimately may require the inspection to be segmented into a number of runs to be performed separately.

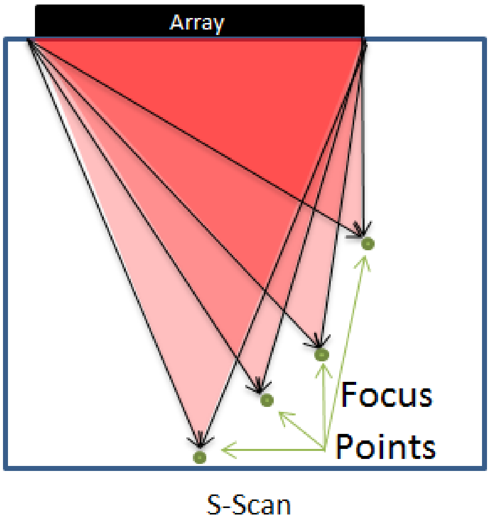

Figure 2.15: Focusing at numerous points to form a sectoral scan using an array.

Beamforming also requires prior knowledge of the component surface profile, to allow the delay laws to be calculated correctly. If the delay laws are incorrect then the angle and focus that was desired may not be achieved in the inspection. Capturing data without performing prior focusing or steering means that data can be collected from a known reference position (the probe) and processed after collection with signal processing algorithms. A variety of algorithms have been developed to replicate beamforming after data collection and TFM has emerged as surpassing beamforming in imaging performance. Chapter 3 explores the delay and sum methodology behind TFM and applies it to complex imaging scenarios.

2.3.1 Signal to Noise Ratio

The Signal to Noise Ratio (SNR) is an important aspect in UT. It quantifies the contrast between the background noise and response from an indication. The main unit for measuring SNR is the decibel (dB). Equation 2.18 is used to calculate the SNR of an indication of amplitude (S_i) against a reference amplitude (S_r). Some typical SNR values are given in Table 2.1, where the SNR relates to signals separated by the ratio in amplitude.

$$SNR_{dB} = 20\log_{10}\left(\frac{S_i}{S_r}\right) \tag{2.18}$$

SNR_{dB}	Ratio (%)
2	80
6	50
20	10

Table 2.1: Relation of SNR value to fractional amplitude of two signals.

Another convention used for displaying A-scans is the signal percent Full Screen Height ($\%FSH$), which is a linear representation of the signal amplitude. A simple example of the relationship between the SNR in dB and $\%FSH$ is shown in Figure 2.16. Two indications are visible on the orange trace, S_1 and S_2, at 50 and 100$\%FSH$ respectively, meaning S_1 is half the amplitude of S_2. Translating this to the dB scale using Equation 2.18, S_1 is 6dB less than S_2.

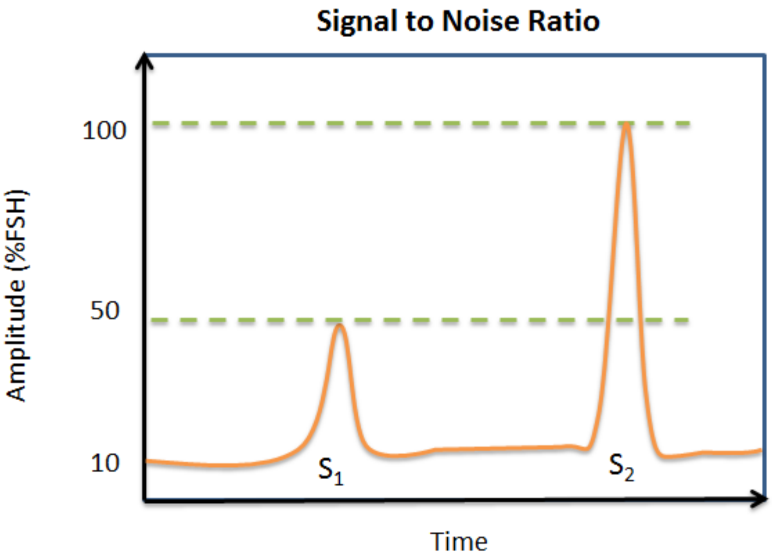

Figure 2.16: Simple A-scan to illustrate SNR, where S_1 and S_2 are indications on the orange trace at 50 and 100$\%FSH$ respectively.

The PAC performs an analogue to digital conversion [27], where a specific bit range must be specified. Current instruments typically offer bit depths in the range of 8 to 16. Smaller bit depths result in smaller data files, however it is important to ensure all data is accurately represented, and thus a higher bit depth may be required. Accurately capturing all features of FMC data is problematic when recording the interface and up to the BW in one A-scan. The acoustic impedance difference means that the interface signal is significantly stronger in amplitude compared with the BW of the component. This also means any internal features of the component may be difficult to represent. Figure 2.17 illustrates representing data using 8 bits compared with 16 bits on the left and right scales respectively. An 8 bit dynamic range offers 256 unique amplitudes whereas 16 bit offers more than 65 thousand. Using a higher bit depth when capturing the interface and BW of the component ensures all features are adequately recorded.

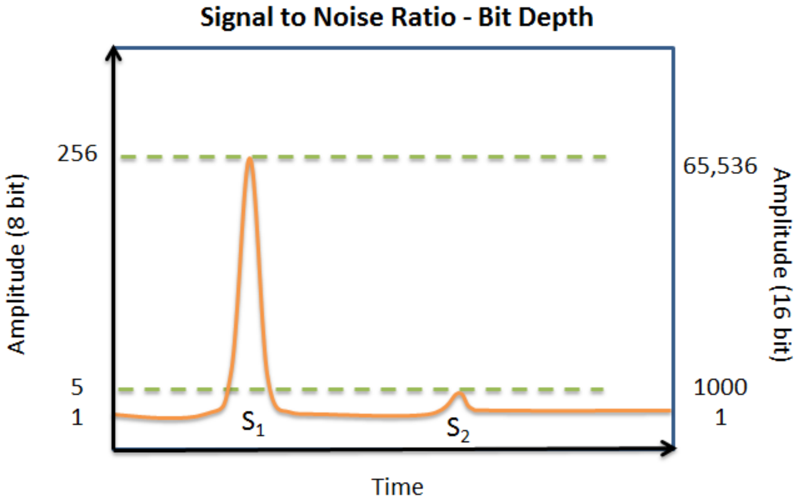

FIGURE 2.17: Importance of selecting appropriate bit depth for data acquisition, to allow all features to be represented with ease.

Care should be taken to avoid saturation of any signal, this occurs when the amplitude is too high to be correctly recorded by the instrumentation. Maximum signals of around $80\% FSH$ should be used to avoid saturation.

2.3.2 Instrumentation

Calculation of complex delay laws is often required when performing an inspection with ultrasonic arrays. Various software packages are available to automatically calculate the delay laws for a specific imaging scenario. This information is passed to the PAC which applies the excitation voltage to each of the array elements. A variety of PACs are available commercially, ranging from portable devices to those that require a fixed workstation. Generally, these PAC allow a selection of parameters to be set by the user, in particular the voltage and excitation signal can be altered.

The sampling frequency is an important aspect to consider when recording a signal [28]. It is essential to sample the data at a rate that accurately represents the true signal. An example of the effect of under sampling is shown in Figure 2.18, when too few samples are taken the signal form is incorrectly reconstructed. Conversely, if too many samples are taken, excessive data is stored which has no additional valuable information. A sampling frequency of 10 times the operating frequency is recommended for data acquisition where the raw signal is required.

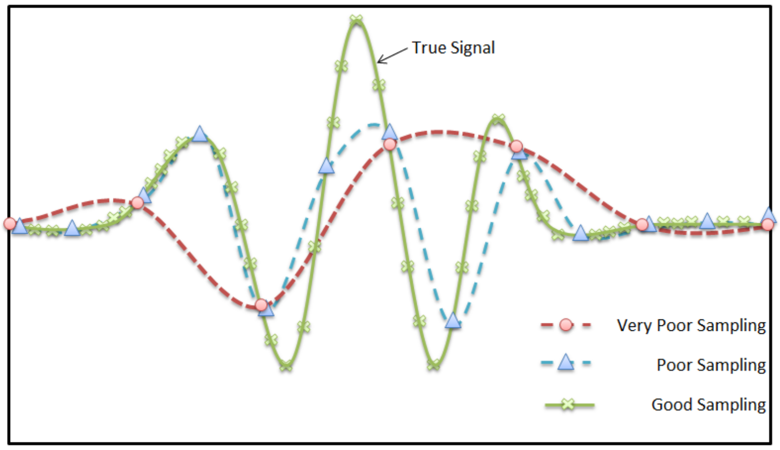

FIGURE 2.18: Example of the impact of sampling rate on signal reconstruction. Too low a sampling frequency results in incorrect form.

2.3.3 Calibration

It is important to perform calibration of an inspection using known reflectors. This ensures that the technique is performing as expected to a known sensitivity. Typically SDH are used to establish the sensitivity of an inspection [29]. The geometry of SDH means they reflect energy in all directions, as opposed to planar defects that depend highly on the angle of incidence. SDH at various depths in a component are used to set the sensitivity to a predefined level. This ensures the inspection is uniform over the full volume. A DAC curve may be employed here, to either increase or reduce the gain amplification factor applied to signals over range. The calibration process for an inspection should also ensure the PAC and probe are operating to a known performance and similarly for any additional equipment used.

Novel inspections techniques that require complex delay laws, data acquisition sequences or signal processing must also undergo calibration to be used in an inspection. However, applying a DAC to such inspections adds more complexity and computational requirements. A method for predicting the sensitivity in novel inspections is therefore required before it is likely to be implemented in industrial NDE. An approach for calculating the relative sensitivity in an inspection volume when employing FMC, TFM and sparse 2D arrays is explored in Chapter 6.

2.3.4 Inspection Technique

Industrial UT contributes towards the safety case of operational plant [30]. It is therefore imperative that the inspection is performed to a high standard, and that the inspection is reliable and repeatable over the lifetime of the plant. A diverse range of components and inspection requirements means extensive variation over the range of applications of UT. Consequently, each inspection is considered in its own right, focused on the objective of the inspection. It is essential to have an understanding of the component, including it's geometry and acoustic properties, and vitally, what flaws may be encountered in the inspection.

Prior knowledge of the component is then combined with experience from similar inspections, resulting in the development of the inspection technique. Computer simulation also plays a vital role in the development of new techniques, since test blocks are costly and experimental trials are time consuming [31]. Simulation bypasses the requirement for a large number of test blocks, with computational models utilised instead. These have been widely developed in recent years, and are therefore increasingly assisting inspection design. The modelling software package CIVA (conceived by CEA de France) has been built up over a number of years to simulate ultrasonic inspection. It forms an analytical solution based on beam propagation and defect interactions. Where more detailed simulation is required, Finite Element Analysis (FEA) can be utilised.

Generally, an inspection technique must be verified before it can be applied in practice with confidence. This involves a process referred to as qualification which aims to expose the variables in an inspection system and evaluate their impact on performance. A significant body that governs how qualification should be conducted is the European Network for Inspection Qualification (ENIQ) [32]. They set out guidelines that should be followed to reach inspection qualification and ultimately they must be convinced that the inspection is suitable for purpose in order to grant it qualification. The further work outlined in Chapter 7 leads into potential qualification of an inspection utilising FMC and TFM with sparse 2D arrays.

2.4 Complex Components

UT plays a vital role in assessing weld integrity in a component. While inspection is not exclusive to welds they are a key focus throughout industrial inspections due to the potential for structural unreliability [33]. An irregular surface profile can develop around the weld due to the manufacturing process. This often involves welding two or more parts together and then machining off the weld cap manually. There is no precise way to do this, resulting in undefined undulations on the surface. Engineering drawings of such components are often unable to fully quantify the irregular form of the surface and an approximation is taken instead.

Uneven surfaces present an issue for UT, as an uninterrupted path between the probe and inspection component is required for ultrasonic transmission. Wedges or shoes that support the probe in an inspection are typically made from perspex which provides a solid, fixed, footprint. This does not fit well with undulations on the surface and causes the probe to rock, in search for the best position. Two major effects are observed in this case: lack of ultrasonic transmission and beam deviations.

Firstly, lack of transmission typically occurs due to no direct path between the probe and component. This may be because of an air gap between the probe shoe and component surface. The acoustic impedance of air is a poor match for both perspex and steel. This results in poor transmission from the probe wedge, through air and into the steel. As a consequence, there will be regions of poor or no coverage which is detrimental to the inspection performance.

Secondly, beam deviations away from the expected beam angle may occur, due to misorientation of the probe. The skewed incident angle then creates an altered refracted angle. The probe and imaging system are not partial to this variation, thus resulting in spurious images. These issues will arise even when using a coupling medium that maintains full contact between the probe and component. This process only becomes more complex when considering arrays, since more than one incident angle is commissioned.

Ultrasonic inspection of components that exhibit an undefined surface is currently performed using numerous conventional probes. Water is employed to fill any unavoidable gaps between the probe wedge and component. This provides a better acoustic coupling than air, increasing the possibility of transmission. The surface profile can be recorded over the range of the inspection by a profilometer. A complex and lengthy data analysis process ensues the inspection, aiming to correct beam deviations. This process is time consuming and expensive as it requires the expertise of a well practised, technically competent, data analyst. A manual iterative process is followed, whereby the position of the probe is speculated for each incremental position. Indications in the inspection can then be traced back to find if they match with any given probe misorientation. This process is highly dependent on suitably experienced and qualified personnel.

These factors make reliable ultrasonic inspection of complex components extremely challenging. It is also particularly difficult to obtain a high level of repeatability, in such inspections. Collectively, this means inspection of complex components is expensive and time consuming. The aim of this study is to combine each of the advances in recent years to establish an efficient inspection of such complex components. This includes harnessing the potential of 2D arrays and efficient new PACs, while exploiting innovative signal processing methods and the latest computer technology to deliver immediate results. Each of these aspects are considered in their own right in the remaining Chapters of this Thesis, before being combined to establish the introduction of an efficient inspection technique for complex components.

2.5 Summary of Review

UT has a proven track record, making it a vital method in industrial NDE yet state of the art UT has largely remained in the laboratory. The inspection of complex components could significantly benefit from innovative signal processing algorithms and advances in ultrasonic array technology. This Thesis aims to develop an efficient inspection system for such components by exploiting the latest in signal processing algorithms and efficient computational methods, combined with 2D array design. Together, these factors offer the potential to result in a more effective, efficient and reliable inspection system.

Chapter 3

Efficient Implementation of TFM Incorporating Refraction

Industrial NDE often presents challenging inspection scenarios, specifically where the component is of complex, unknown geometry. Recent advances in computer technology have paved the way for novel imaging methods, using advanced signal processing algorithms. The Total Focusing Method (TFM) is currently considered as the gold standard in ultrasonic imaging [34]. Consequently, the methodology behind an extremely efficient implementation of TFM on Graphic Processing Units (GPU) is explored in this Chapter. The benefits and drawbacks of TFM, compared with conventional UT, are also discussed. The ultimate aim is to employ this algorithm for imaging components of unknown surface profile, which will be developed in the remainder of this Thesis. The mathematical calculations involved in imaging an arbitrary surface component with TFM are examined for 2D and 3D volumes.

3.1 Post-Processing Imaging Algorithms

Post-processing algorithms have gained popularity with the introduction of phased array transducers [34]. Conventional UT typically involved acquiring an A-Scan at each probe position, which could be stacked to form a B-Scan. As arrays are essentially composed of many small individual probes, the volume of data and potential imaging methods are therefore much greater. Beamforming is considered to be the physical steering and focusing of ultrasound, whereas post-processing imaging algorithms virtually replicate this process. Beamforming is commonly used with arrays, where the elements are pulsed in a sequence such that the ultrasonic beam transpires in a specified composition, as illustrated in Chapter 2. Advanced post-processing algorithms offer an alternative that avoids computation of a vast number of delay laws. Instead, imaging algorithms are applied to raw data that has not undergone beamforming. They have been demonstrated to offer equal performance to beamforming for various arrangements and mean that many imaging scenarios can be applied post-inspection without affecting the original data [2]. Ultrasonic arrays have permitted more efficient inspections by offering additional control of the ultrasonic energy [35]. Despite the introduction of arrays some 20 years ago, imaging techniques have remained relatively unchanged from conventional UT. Post-processing algorithms aim to improve the efficiency and performance of inspections by exploring new imaging techniques, many of which have been adapted from medical or SONAR disciplines [36].

As reviewed in Chapter 2, conventional imaging with arrays typically involves applying computed delay laws. This allows ultrasonic beam-steering, as illustrated in Figure 3.1. Here the elements are pulsed sequentially from left to right, resulting in a combined wave-front at the specified point of focus [37].

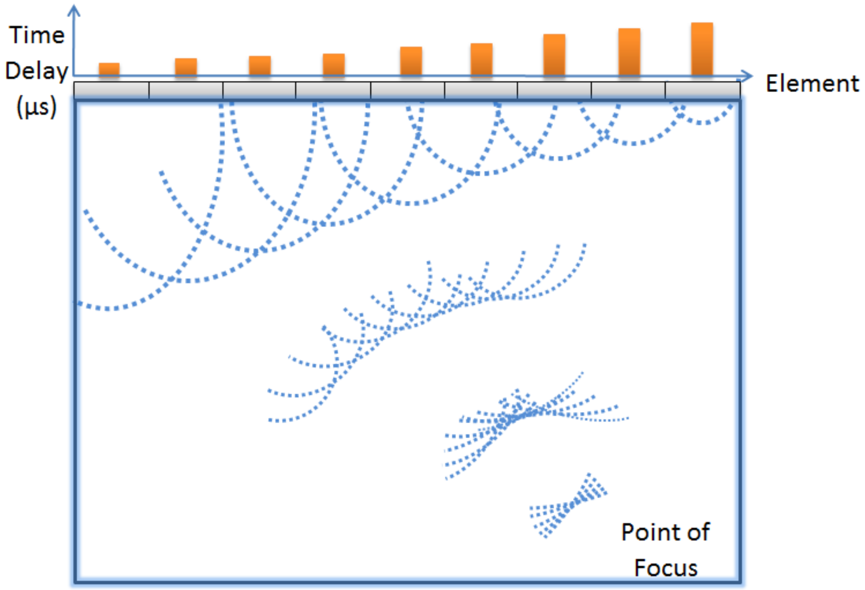

Figure 3.1: Conventional beamforming using a linear array. Each element is pulsed at a specified time to produce a combined wave-front, shown in blue, that is focused at a particular angle and range.

In contrast, imaging with post-processing algorithms involves collecting a full raw data set and processing the data afterwards. This data set is generally referred to as Full Matrix Capture (FMC). Unlike conventional imaging, no delay laws are applied to the elements in the array and all focusing occurs in the post-processing stage after data collection [38]. For FMC, each element is used as a Transmitter (Tx) in turn, while all elements simultaneously act as Receivers (Rx). FMC is therefore the complete set of amplitude-time signals, also known as A-Scans, for each Transmit-Recieve (Tx-Rx) pair in the array. So, for an array of N elements, the FMC would be NxN A-scans.

Figure 3.2 illustrates the process of FMC, transmitting on element 3 as an example, while receiving on all elements. The green wave-fronts represent the ultrasonic field from element 3 as the transmitter, while the orange wave-fronts represent the regions where all other elements are effectively listening for responses, as receivers. This process would be repeated for all elements in the array operating as transmitters to obtain the FMC. The ultrasonic energy is distributed relatively evenly over the whole inspection region in FMC, compared with conventional beamforming, since it is not focused at a pre-determined point in space.

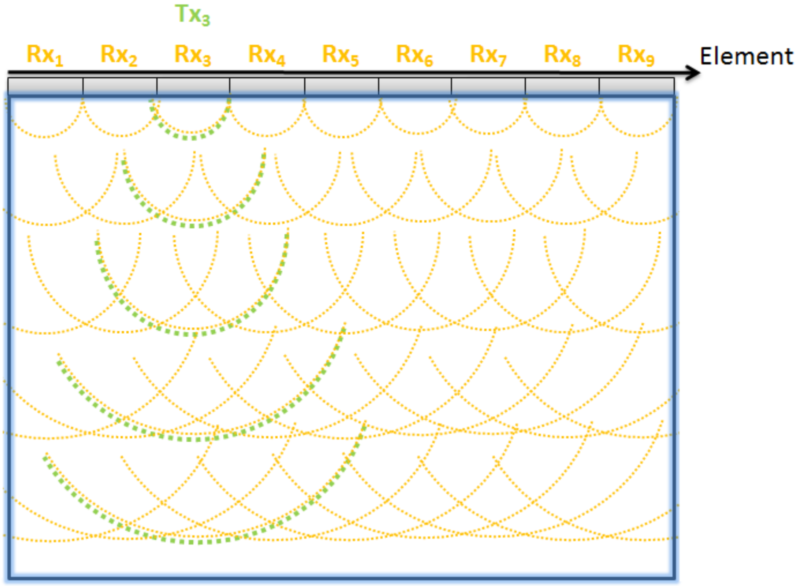

FIGURE 3.2: Illustration of FMC, transmitting on element 3 and receiving on all elements. This process is repeated, using each element in the array as a transmitter. The energy from the transmitting element is shown in green, while orange represents the field of each receiver.

Intrinsically, a FMC data set can be relatively large due to the number of elements in an array and the range of the inspection. Initially, this also meant FMC was time-consuming to collect. However, electronics have progressed in recent years, and many manufacturers of phased array controllers have invested in advancing their hardware and software for FMC. Efficient data collection is now possible with a number of commercial instruments [39, 40].

An alternative to FMC is Half Matrix Capture (HMC) which utilises redundancy due to reciprocity in the FMC data [41]. HMC can therefore be around half of the size of FMC data, while maintaining fidelity. Sparse Matrix Capture (SMC) is also common [42], where for each transmitting element, only specified elements in the array act as receivers. This can significantly reduce the amount of data stored but may result in loss in data quality for some applications. A visual representation of each of these data formats is shown in Figure 3.3.

FMC		Tx							
		1	2	3	4	5	6	..	n
Rx	1	$A_{1,1}$	$A_{2,1}$	$A_{3,1}$	$A_{4,1}$	$A_{5,1}$	$A_{6,1}$	$A_{..}$	$A_{n,1}$
	2	$A_{1,2}$	$A_{2,2}$	$A_{3,2}$	$A_{4,2}$	$A_{5,2}$	$A_{6,2}$	$A_{..}$	$A_{n,2}$
	3	$A_{1,3}$	$A_{2,3}$	$A_{3,3}$	$A_{4,3}$	$A_{5,3}$	$A_{6,3}$	$A_{..}$	$A_{n,3}$
	4	$A_{1,4}$	$A_{2,4}$	$A_{3,4}$	$A_{4,4}$	$A_{5,4}$	$A_{6,4}$	$A_{..}$	$A_{n,4}$
	5	$A_{1,5}$	$A_{2,5}$	$A_{3,5}$	$A_{4,5}$	$A_{5,5}$	$A_{6,5}$	$A_{..}$	$A_{n,5}$
	6	$A_{1,6}$	$A_{2,6}$	$A_{3,6}$	$A_{4,6}$	$A_{5,6}$	$A_{6,6}$	$A_{..}$	$A_{n,6}$
	..	$A_{..}$	$A_{..}$	$A_{..}$	$A_{..}$	$A_{..}$	$A_{..}$	$A_{..}$	$A_{..}$
	n	$A_{1,n}$	$A_{2,n}$	$A_{3,n}$	$A_{4,n}$	$A_{5,n}$	$A_{6,n}$	$A_{..}$	$A_{n,n}$

HMC		Tx							
		1	2	3	4	5	6	..	n
Rx	1	$A_{1,1}$							
	2	$A_{1,2}$	$A_{2,2}$						
	3	$A_{1,3}$	$A_{2,3}$	$A_{3,3}$					
	4	$A_{1,4}$	$A_{2,4}$	$A_{3,4}$	$A_{4,4}$				
	5	$A_{1,5}$	$A_{2,5}$	$A_{3,5}$	$A_{4,5}$	$A_{5,5}$			
	6	$A_{1,6}$	$A_{2,6}$	$A_{3,6}$	$A_{4,6}$	$A_{5,6}$	$A_{6,6}$		
	..	$A_{..}$	$A_{..}$	$A_{..}$	$A_{..}$	$A_{..}$	$A_{..}$	$A_{..}$	
	n	$A_{1,n}$	$A_{2,n}$	$A_{3,n}$	$A_{4,n}$	$A_{5,n}$	$A_{6,n}$	$A_{..}$	$A_{n,n}$

SMC		Tx							
		1	2	3	4	5	6	..	n
Rx	1	$A_{1,1}$	$A_{2,1}$	$A_{3,1}$	$A_{4,1}$	$A_{5,1}$	$A_{6,1}$	$A_{..}$	$A_{n,1}$
	2		$A_{2,2}$		$A_{4,2}$		$A_{6,2}$		$A_{n,2}$
	3	$A_{1,3}$		$A_{3,3}$		$A_{5,3}$		$A_{..}$	
	4		$A_{2,4}$			$A_{5,4}$	$A_{6,4}$		$A_{n,4}$
	5	$A_{1,5}$		$A_{3,5}$	$A_{4,5}$			$A_{..}$	$A_{n,5}$
	6		$A_{2,6}$	$A_{3,6}$	$A_{4,6}$	$A_{5,6}$	$A_{6,6}$	$A_{..}$	
	..	$A_{..}$		$A_{..}$	$A_{..}$		$A_{..}$		$A_{..}$
	n	$A_{1,n}$	$A_{2,n}$		$A_{4,n}$	$A_{5,n}$		$A_{..}$	$A_{n,n}$

FIGURE 3.3: Example of FMC, HMC and SMC, where $A_{Tx,Rx}$ represents the A-Scan for a particular Tx-Rx pair. FMC is the complete data set, HMC is the lower half of FMC. SMC is user specified for the required Tx-Rx.

The motivation behind post-processing algorithms comes from the desire to develop new and efficient imaging techniques, especially for components that are difficult to inspect conventionally [43]. Two of the main challenges tackled by signal processing algorithms for UT in industry are ultrasonically noisy materials with coarse grains, and components with complex or undefined geometry [44].

It is important to note that post-processing offers the added benefit of the raw data remaining unchanged, meaning new processing algorithms can be used as and when they become available, on previously collected data. Additionally, recent improvements in computing capabilities [45] have supported the success of post-processing algorithms, pemitting efficient implementations and allowing real-time applications.

A range of algorithms have been established to improve imaging performance, each with their own benefits and limitations. Of all of the algorithms developed, TFM has gained elite status, as it offers improved imaging performance over conventional beamforming methods [46]. It was developed from the Synthetic Aperture Focusing Technique (SAFT) [47, 48], which is ordinarily used in SONAR. Other post-processing algorithms are targeted at reducing noise, such as Phase Coherence Imaging (PCI) [49]. Generally, the purpose of such algorithms is to extract useful information about the component in an effective and efficient way, while ensuring the inspection is more reliable, repeatable and robust [50, 51]. TFM is the most widespread and general purpose of the algorithms recently developed.

3.2 The Total Focusing Method

TFM is a delay and sum post-processing algorithm, initially developed by Wilcox and Drinkwater [2]. It is widely accepted as the gold standard of ultrasonic imaging in NDE. The algorithm mimics focusing of the ultrasonic beam at each pixel in a specified imaging space. For simplicity, the 2D case is considered first, as illustrated in Figure 3.4. Other imaging arrangements are studied later in this Chapter. A linear ultrasonic array is considered to be in contact with the inspection medium, where the transmitter and receiver are located at y_{Tx} and y_{Rx} respectively, and each pixel, P, has co-ordinates (y_P, z_P). In Figure 3.4 the green line represents the ultrasonic path from the transmitter to the pixel, and conversely, the yellow lines indicate the paths from the pixel to each receiver. Note, this only represents a single column of the FMC data for one transmitter.

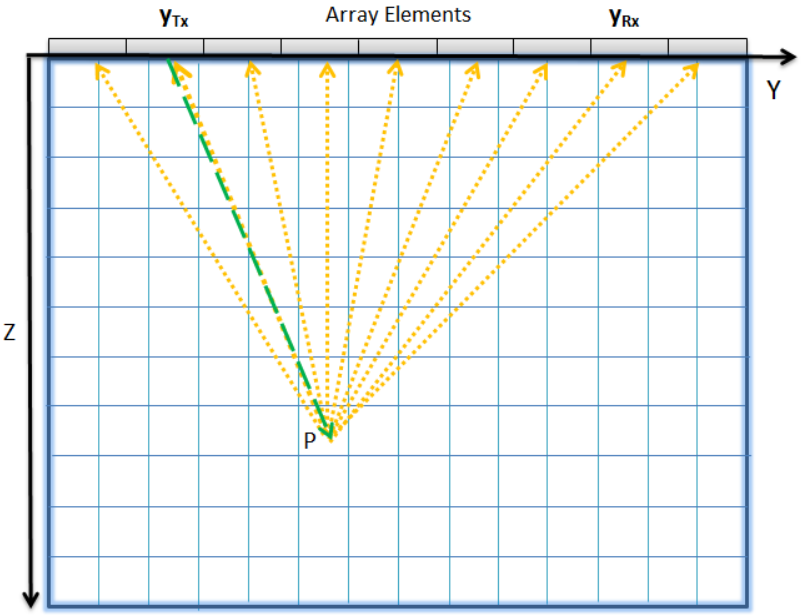

FIGURE 3.4: Representation of 2D TFM image structure, where the image space (y, z) is split into a grid of pixels. A linear array is placed in line with the y-axis of the image.

Focusing at each pixel is determined by summation of the amplitude from each Tx-Rx A-Scan in the FMC, at the time appropriate to each pixel location. This is achieved by calculating the Time of Flight (ToF) from the transmitter to the pixel and back to the receiver. The respective amplitudes for every Tx-Rx pair are then accumulated, and the total is assigned as the final amplitude of the pixel. This is repeated for every pixel in the image to build a map of relative intensity over the inspection region. The amplitude of any given pixel in the image can be found using Equation 3.1. Referring to the co-ordinate convention used in Figure 3.4, and where c_l is the longitudinal acoustic velocity in the inspected medium.

$$I_{y,z} = \left| \sum i_{Tx,Rx} \left(\frac{\sqrt{(y_{Tx} - y_P)^2 + z_P^2} + \sqrt{(y_{Rx} - y_P) + z_P^2}}{c_l} \right) \right| \tag{3.1}$$

As an example, an image with a resolution of 1mm over an area of 50 x 50mm would hold 2,500 pixels, and therefore require 2,500 iterations of Equation 3.1 for each Tx-Rx pair of elements, or A-Scan in the FMC. This is a very conservative case, and in practice the resolution is likely to be sub millimetre, with around 16,000 Tx-Rx pairs. Therefore, this approach to TFM requires considerable computing power and is unlikely to realise real-time imaging. In the context of this work real-time imaging is considered to provide the operator with a live updating image, with a frame rate in the order of seconds deemed acceptable. Significant data processing times of an hour or longer are not desirable.

A number of studies have considered how to accelerate the TFM process in a move towards real-time imaging. These studies include executing TFM on Graphic Processing Units (GPU) [52], Field Programmable Gate Arrays (FPGA) [53], or altering and condensing the required calculations. At the time the work for this Thesis was completed, Dziewierz [3] and Lardner's [4] implementation of TFM was established as offering the most efficient performance. A thorough understanding of mechanisms involved in this efficient execution of TFM is required as the background to the work undertaken in this Thesis. The remainder of this Chapter therefore outlines the theory and methodology behind this implementation of TFM and extends it to a range of inspection scenarios.

3.3 Efficient Implementation of TFM

An increase in the efficiency of TFM from its traditional implementation is essential in order to extend it to more complex inspection scenarios. The number of calculations required for a relatively simple inspection is already substantial and can be expected to significantly increase as practical, often intricate, inspections are considered. Two major confines of the original version of TFM were considered to be the computational expense, and the restraint to a single load medium. Both limitations are problematic in realising an industrial application of TFM since inspections through more than one medium are common and real-time results are desirable.

A group of researchers in CUE, including the author, lead by Dziewierz and Lardner embarked on developing a suite of ultrasonic imaging algorithms with an efficient implementation of TFM at the core. The key focus was condensing the computational expense of such algorithms while extending them to fit typical inspection scenarios. The most important result from this work was an efficient execution of TFM capable of handling refraction through an interface [54].

3.3.1 Graphics Card Processing

GPUs have recently been recognised as a diverse and powerful processing tool [55]. Most commonly associated with rendering the display in computers, they are increasingly being used in place of traditional Central Processing Units (CPU). Various scientific research projects have harnessed the potential of GPUs, for both modelling and data processing purposes [56–58].

Parallel processing has been identified as one key attribute of GPUs [59, 60], making them especially suited for executing TFM. The ToF can be calculated independently for each pixel in a TFM image, meaning they can be calculated in parallel. One drawback of GPU computing is the latency in accessing and transferring data stored on the GPU. With this is mind, operations are mainly completed on the GPU and data transfer is kept to a minimum to avoid loss in efficiency. An added advantage of GPU computing is that the CPU is free to run other applications, such as a motor-controller, as would often be required in an industrial inspection. A comprehensive narrative of GPU handling of data is out-with the scope of this Thesis, but more information can be found in [61].

A version of TFM was established on NVidia GPUs using the CUDA programming language [62]. This move provided additional processing power, and considerably reduced the computational expense. Moreover, a tactic to reduce the number of ToF calculations required was considered highly desirable.

3.3.2 ToF Sampling

The processing demand of TFM can be significantly reduced by considering the ToF for only a sample of pixels in the image. This is achieved by splitting the image into Z-lines, as shown in Figure 3.5, and calculating the ToF to only a small number of pixels along each of the lines. In a 2D TFM image there is a Z-line at each increment in the y-axis.

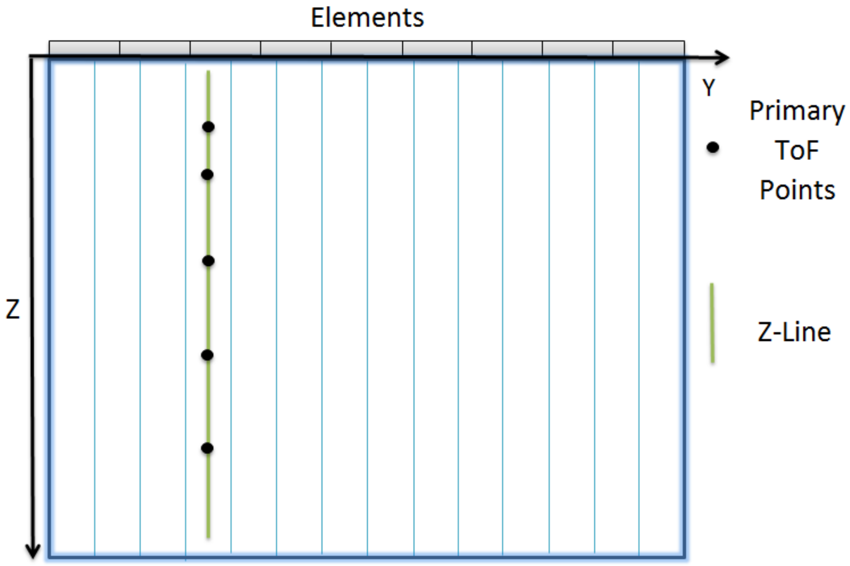

FIGURE 3.5: The image is split into Z-lines, at increments consistent with the y-axis, and the ToF is calculated for only a sample of points in the z-axis. A mathematical description is then used to describe the ToF for all pixels.

These calculated ToF are known as the primary ToFs, and can be used to produce a mathematical function that represents the ToF for the extent of the Z-line. Although the ToF may be a linear relation for a contact inspection, it may be non-linear for more complex scenarios. An interpolating polynomial was chosen to be a suitable function for describing the ToF per Z-line [3, 4]. This method is well suited to GPU architecture and the calculations for each Z-line can be computed in parallel. The interpolating polynomial has been demonstrated to be stable and well conditioned, delivering small numerical errors between the actual ToF and interpolated value. This process is markedly more efficient than calculating the ToF for each pixel in the image, without any distinguishable reduction in image quality.

3.3.3 Evaluation

A simple inspection was performed to evaluate the GPU TFM implementation. The experimental set up is shown in Figure 3.6, with the GPU TFM image shown in Figure 3.7. A single FMC was obtained using a 5MHz linear array, with an element pitch of 0.7mm, and a sampling frequency of 50MHz. The imaging parameters were set with a resolution of 0.5mm in both axes, over an area of 90mm in length by 60mm in depth. The array was placed in contact with a flat stainless steel test block of thickness 60mm. The block contains four 3mm SDH at various depths, as noted on Figure 3.6, where the dimensions are in millimetres. The image is set with a dynamic range of 26dB, where red denotes a high amplitude and dark blue is a low amplitude. This scale is used throughout this Thesis, unless otherwise stated.

The FMC data was processed using the GPU verison of TFM and result is shown in Figure 3.7. The image shows the SDH are positioned correctly, along with the BW. This image is equivalent to that achieved with a basic CPU implementation of TFM, however, the GPU TFM image was obtained in less than a second, whereas an equivalent CPU version could take up to around 20 hours. It is noted that there may be more efficient editions of TFM on the CPU, nevertheless, this is a significant reduction in time while maintaining equivalent imaging performance.

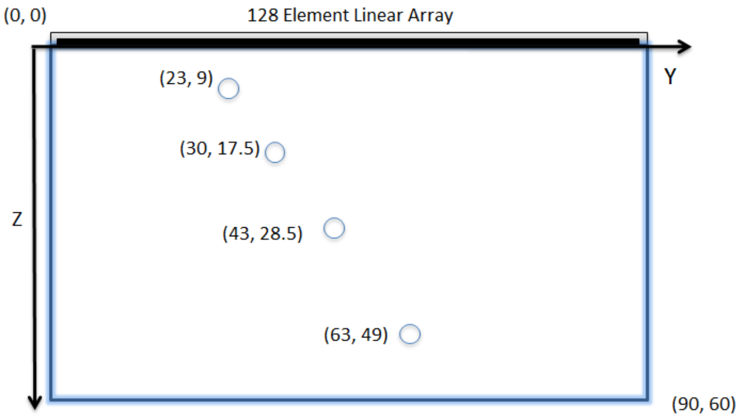

FIGURE 3.6: Schematic of TFM inspection using a linear array, in contact with a 60mm thick stainless steel test block. Four 3mm SDH at various depths, are located within the block.

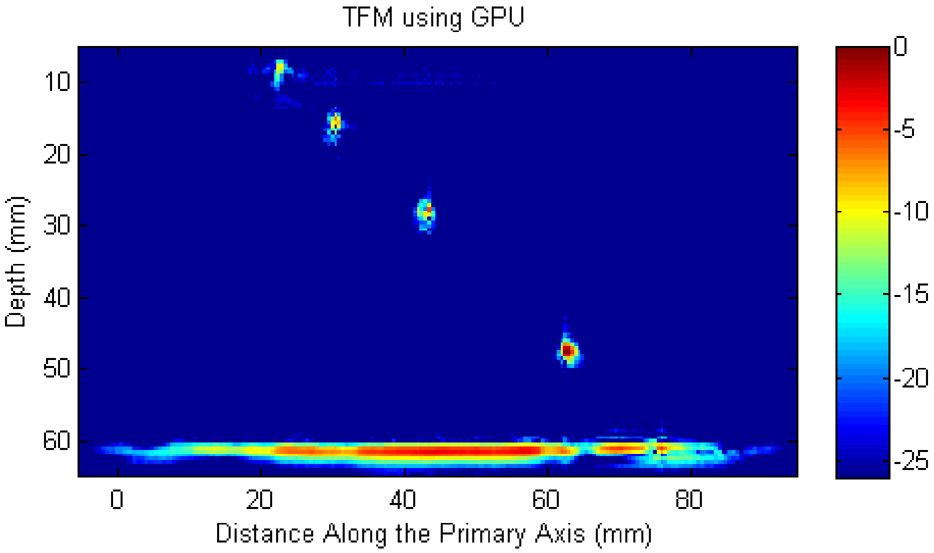

FIGURE 3.7: TFM image created to evaluate the GPU version developed by Dziewierz and Lardner.

This result means TFM is no longer constrained to research laboratories, and may be suitable for industrial NDE. The methodology of this efficient implementation also means more complex imaging circumstances may be realised with ease. For the remainder of this Thesis, only this GPU execution of TFM is considered.

3.4 TFM with Refraction

To extend TFM to a wider range of NDE applications, it is important to manage refraction. When an ultrasonic beam passes from one medium to another, refraction occurs at the interface as defined by Snell's Law and explained in Chapter 2. Industrial inspections often use angled wedges to direct the ultrasonic beam. In conventional UT, delay laws are calculated according to the geometry of the probe, wedge and component being inspected. These delay laws account for the change in material properties between the wedge and component, and adjust data accordingly in the imaging process [63]. This is a relatively straightforward, non-expensive operation for conventional transducers, however, it becomes a more involved process for arrays and complex imaging scenarios.

Refraction must be taken into account even with a flat wedge in TFM, due to the nature of FMC. Observing Figure 3.8, refraction occurs at the interface between the two media, in the path between the transmitter and the pixel. Initially, a linear array and 2D image space (y, z) are studied, and the ultrasonic path is regarded as a ray. The interface is assumed to be planar, and can therefore be described by the equation $z = 0$. The probe is assumed to be above $z = 0$ and the image space is below, in negative z. Although the position of the surface is known, the point where the ultrasonic ray passes through the surface is unknown. In TFM, the point where the ray passes through the interface, referred to as the Point of Refraction (PoR), changes depending on the pixel, and Tx-Rx pair contributing towards that pixel.

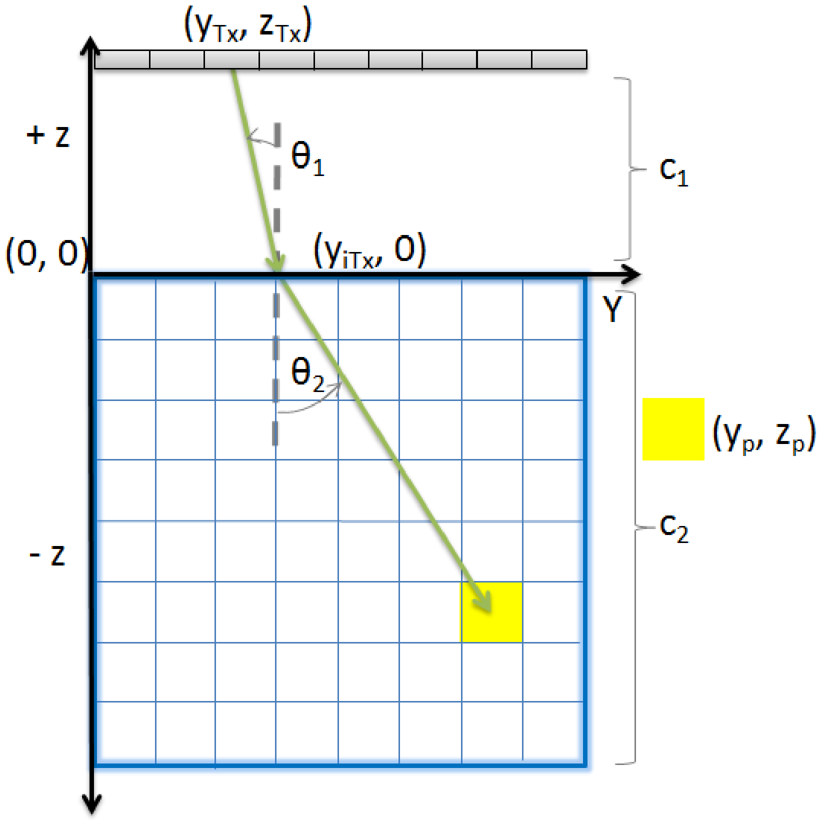

FIGURE 3.8: Illustration of ultrasonic path from Tx to the pixel highlighted in yellow. The location of the Tx and pixel can be used to determine the PoR at the surface.

Taking the Tx position as (y_{Tx}, z_{Tx}), the PoR on the interface as $(y_{iTx}, 0)$ and the pixel location as (y_p, z_p), a solution can be derived to locate y_{iTx}. First, the angle in medium one can be defined by trigonometry as

$$sin(\theta_1) = \frac{(y_{iTx} - y_{Tx})}{\sqrt{(y_{iTx} - y_{Tx})^2 + z_{Tx}^2}} \tag{3.2}$$

Similarly, the angle in medium two can be defined as

$$sin(\theta_2) = \frac{(y_p - y_{iTx})}{\sqrt{(y_p - y_{iTx})^2 + z_p^2}} \tag{3.3}$$

These definitions of $sin(\theta_1)$ and $sin(\theta_2)$ can then be substituted into Equation 2.8 for Snell's Law defined in Chapter 2, to give

$$\frac{(y_{iTx} - y_{Tx})/\left(\sqrt{(y_{iTx} - y_{Tx})^2 + z_{Tx}^2}\right)}{(y_p - y_{iTx})/\left(\sqrt{(y_p - y_{iTx})^2 + z_p^2}\right)} = \frac{c_1}{c_2} \tag{3.4}$$

The PoR, y_{iTx} can then be found by solving Equation 3.4 for y_{iTx}, where z_{iTx} is already known to be zero. Since Equation 3.4 is a double-quadratic, there are four solutions for y_{iTx}. Two of the solutions represent a non-physical situation, as they contain imaginary numbers. The other two form the solution where $y_p > y_{Tx}$ and $y_p < y_{Tx}$, which is known. There is one unique solution to this system, where $y_{Tx} = y_p$, which results in $y_{iTx} = y_{Tx} = y_p$. This occurs due to $\theta_1 = 0$, so there is no change in angle between the media, meaning $\theta_2 = 0$ also.

In TFM, utilising FMC data, the transmitting element is often not at the same position as the receiving element. Therefore, the PoR from the transmitter will be different from that of the receiver. A new point for the receiver position is defined as (y_{Rx}, z_{Rx}). The PoR $(y_{iTx}, 0)$ must also be found for the path from the pixel-receiver, defined as $(y_{iRx}, 0)$. This configuration is shown in Figure 3.9. Equation 3.4 can determine y_{iRx} in the same way as it was used to determine y_{iTx}.

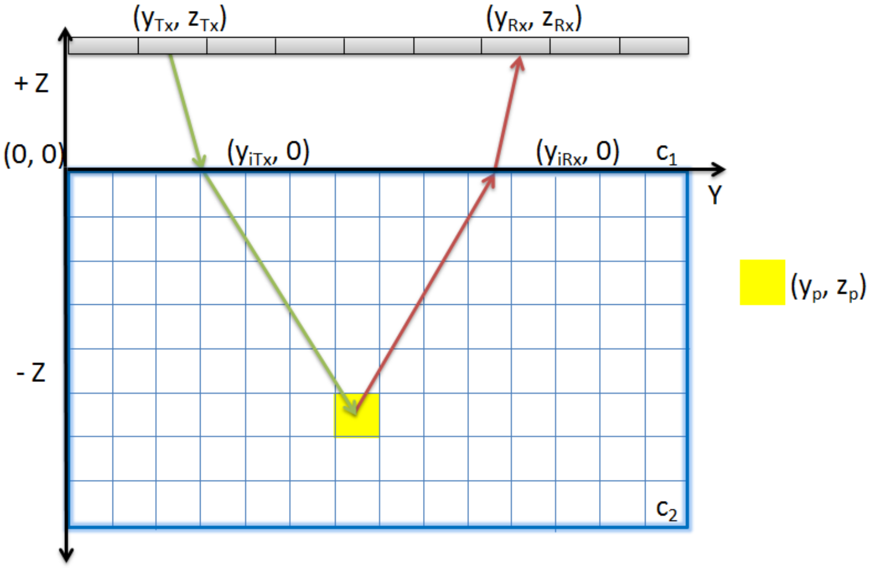

FIGURE 3.9: Calculating the ToF of the ultrasonic path from Tx to pixel to Rx, through an interface.

Now that the PoR is known, the ToF from the transmitter through the interface, to the pixel and back through the interface to the receiver can be calculated. The calculations are separated into τ_{Tx-p} and τ_{p-Rx} for the ToF from the transmitter to the pixel and, conversely the ToF from the pixel to the receiver.

$$\tau_{Tx-p} = \frac{\sqrt{(y_{iTx} - y_{Tx})^2 + (z_{iTx} - z_{Tx})^2}}{c_1} + \frac{\sqrt{(y_p - y_{iTx})^2 + (z_p - z_{iTx})^2}}{c_2} \tag{3.5}$$

$$\tau_{p-Rx} = \frac{\sqrt{(y_{iRx} - y_p)^2 + (z_{iRx} - z_p)^2}}{c_2} + \frac{\sqrt{(y_{Rx} - y_{iRx})^2 + (z_{Rx} - z_{iRx})^2}}{c_1} \tag{3.6}$$

Adjusting Equation 3.1 to perform TFM though an interface at z = 0 then becomes

$$I_{y,z} = \left| \sum i_{Tx,Rx} \left(\tau_{Tx-p} + \tau_{p-Rx} \right) \right| \tag{3.7}$$

An example of this routine is shown in Figure 3.10. The test block used is the same as that in the contact case, in Figure 3.7, with the probe now separated from the surface by a coupling medium of a specified height. The 5MHz linear array was used as before and it was placed 25mm above the test block with the gap filled with water. The resolution of the TFM image in y and z was set to 0.2mm. The image is now centred at the middle of the array in the y axis. The SDH and BW are accurately identified in this image, proving the algorithm is operating correctly. As with the contact case, this TFM image was constructed in less than 1 second.

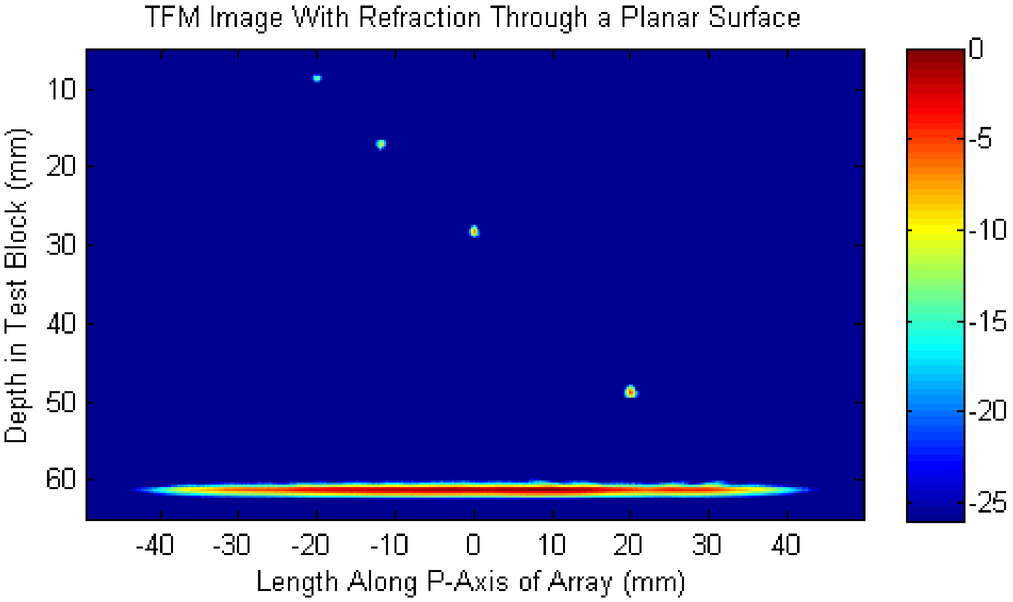

FIGURE 3.10: TFM image constructed from FMC data collected with the probe parallel to the surface, at a height of 25mm in water.

3.4.1 3D TFM

One significant advantage 2D arrays offer is volumetric imaging [64], which TFM can facilitate. A 3D co-ordinate system is now considered, as shown in Figure 3.11. In addition to the system used previously, the x-axis represents the secondary axis of the array.

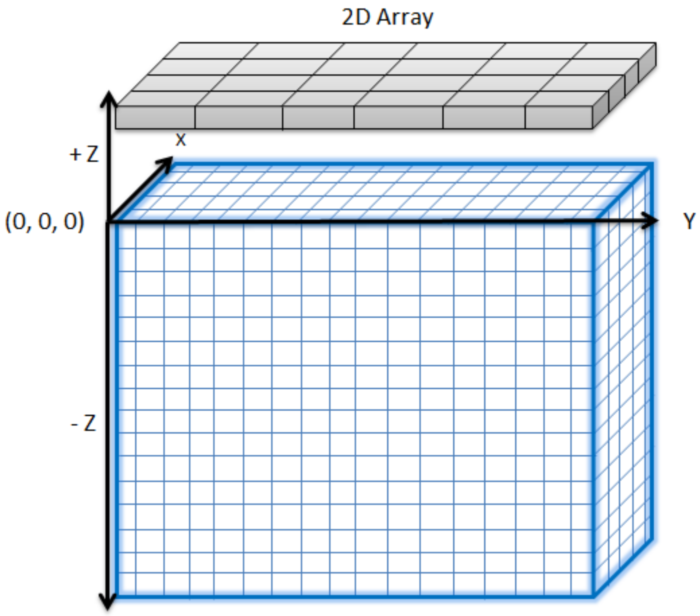

FIGURE 3.11: Co-ordinate convention for 3D imaging space using TFM. The y-axis is in line with the primary axis of a 2D array, the x-axis is in line with the secondary axis of the array and the z-axis is image depth.

A contact inspection is considered first, where the transmitter and receiver are positioned at zero on the z-axis. They are defined as $(x_{Tx}, y_{Tx}, 0)$ and $(x_{Rx}, y_{Rx}, 0)$ respectively, and each pixel in the image is (x_p, y_p, z_p).

The distance from transmitter to the pixel is then

$$d_{Tx-p} = \sqrt{(y_{Tx} - y_p)^2 + (x_{Tx} - x_p)^2 + z^2} \tag{3.8}$$

Similarly, the distance from the pixel to receiver is

$$d_{p-Rx} = \sqrt{(y_{Rx} - y_p) + (x_{Rx} - x_p)^2 + z^2} \tag{3.9}$$

Equations 3.8 and 3.9 can then be combined in Equation 3.1 to evaluate the pixel amplitude

$$I_{x,y,z} = \left| \sum i_{Tx,Rx} \left(\frac{d_{Tx-p} + d_{p-Rx}}{c_1} \right) \right| \tag{3.10}$$

It is typically most convenient to construct 2D images, in (y, z) at specified intervals in x and then combine the data to produce a 3D image. The increments in x then represent the resolution in the x-axis. Evaluation of this process was achieved by collecting FMC data in contact with the test block with a 1MHz 2D matrix array [Appendix B], as shown in Figure 3.12. The array has 18 elements in the primary axis and 7 elements in the secondary axis, with a pitch of 3.35mm and 3.85mm in the primary and secondary axis respectively.

The 2D TFM images obtained at three increments of 5mm at the centre of the x-axis are shown in Figure 3.13. Each image was created with a resolution of 0.2mm over a depth of 100mm and y-axis length of 60mm, coincident with the primary axis of the array. A 3D representation of this data is shown in Figure 3.14, obtained with a resolution of 0.2mm in the x-axis.

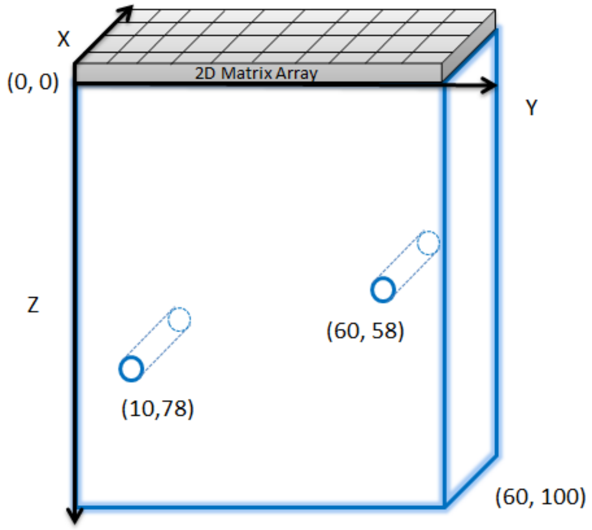

FIGURE 3.12: Experimental set-up for 3D TFM example, using a 2D matrix array in contact with a 100mm thick stainless steel test block. Two 3mm SDH at z= 58mm and 78mm are present.

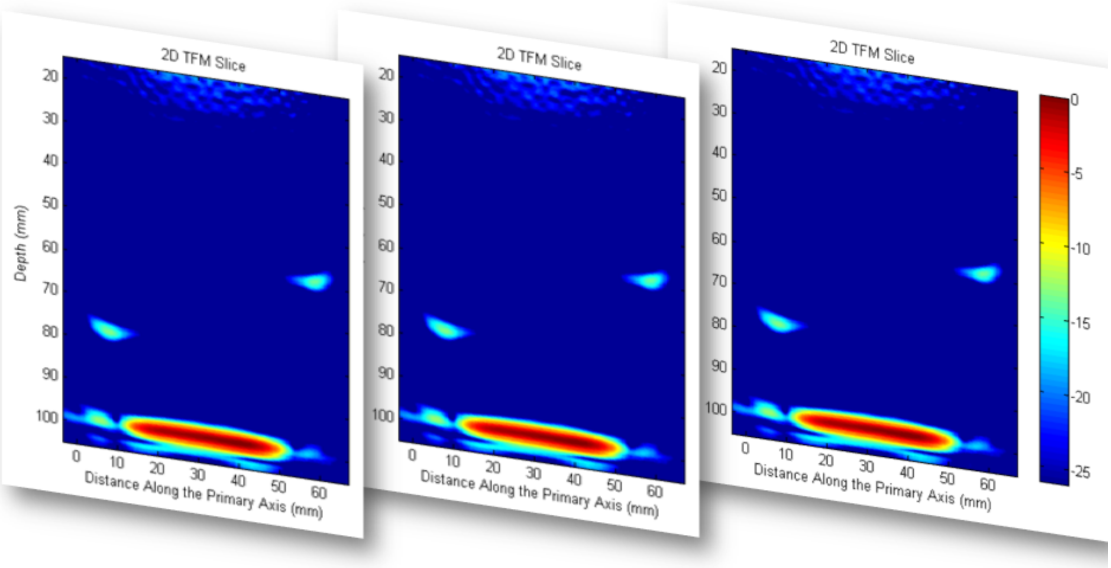

FIGURE 3.13: 2D TFM slices at increments in the x-axis, which can be combined to create a 3D TFM image.

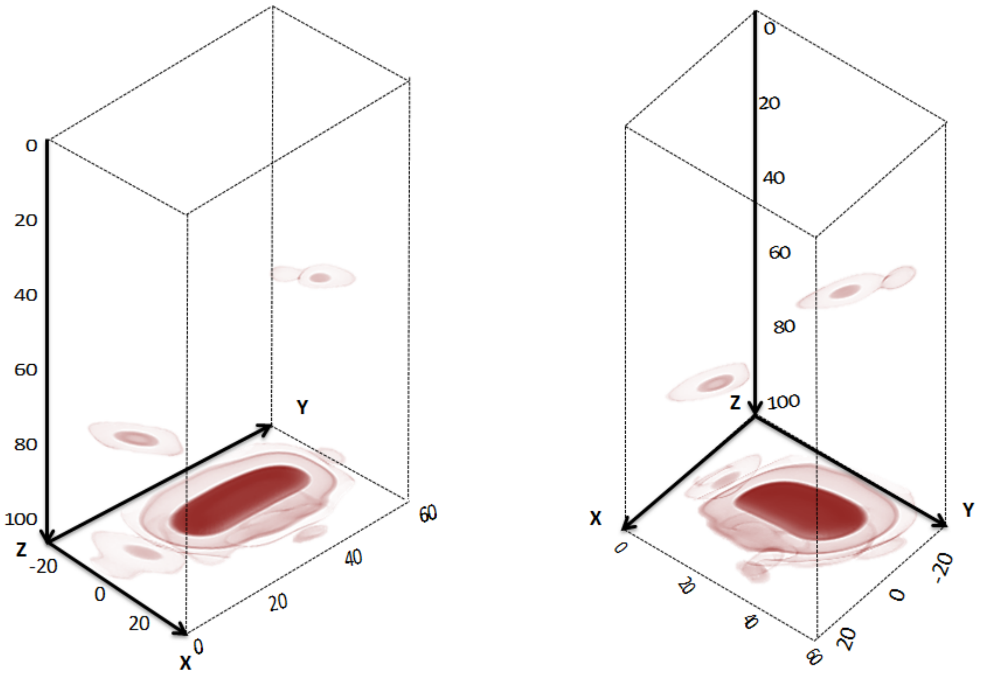

Figure 3.14: 3D TFM image obtained by combining numerous slices of 2D TFM data in the x-axis. High amplitudes are represented in dark red.

Following the same methodology, 3D imaging through a planar interface can be performed. Points P_1, P_i and P_2 are used to generalise the start point of the ray, the refracted point and then the end point. First, the co-ordinate system is shifted by a vector $(x_s, y_z, 0)$ such that its origin is centred on P_1 in the x and y axes, and zero in the z-axis. A rotation, represented by α is applied to the co-ordinate system, such that P_1, P_i and P_2 all lie within the same plane, obeying the laws of refraction. Figure 3.15 illustrates the shifted and rotated co-ordinate system, represented by (x_s, y_s, z_s).

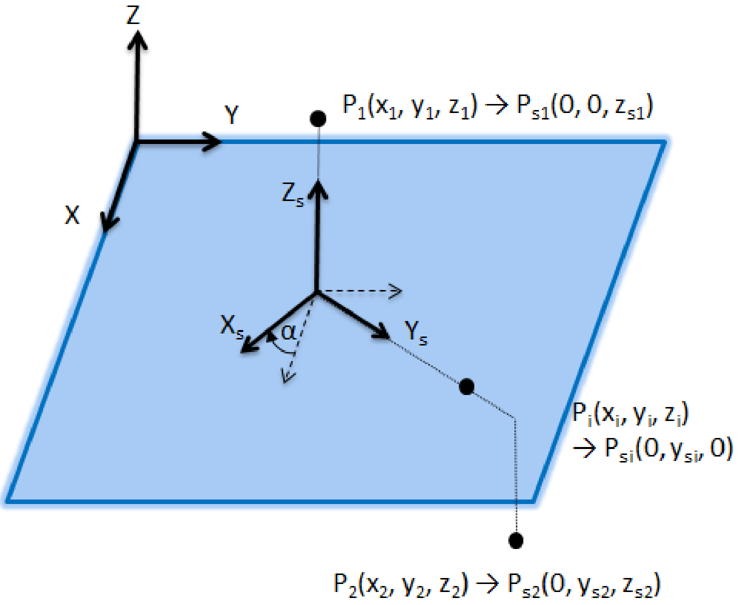

FIGURE 3.15: Illustration of shifted and rotated co-ordinate system used to find the point of refraction in 3D.

Equation 3.4 can then be used to find the PoR, as in the 2D case [3]. As noted on Figure 3.15, the points P_1, P_i and P_2 are translated into the new co-ordinate system to become

$$P_1(x_1, y_1, z_1) \rightarrow P_{s1}(0, 0, z_{s1})$$

$$P_i(x_i, y_i, z_i) \rightarrow P_{si}(0, y_{si}, 0)$$

$$P_2(x_2, y_2, z_2) \rightarrow P_{s2}(0, y_{s2}, z_{s2})$$

The PoR can then be translated back to the original axis by

$$P_i(x_i, y_i, zi) \rightarrow P_{si}(x_1 + x_{si} sin(\alpha), y_1 + y_{si} cos(\alpha), 0)$$

Now, to account for the ToF, Equation 3.5 is separated into the ultrasonic path in medium 1 and medium 2 for the 3D case, to become

$$\tau_{Tx-iTx} = \frac{\sqrt{(y_{iTx} - y_{Tx})^2 + (x_{iTx} - x_{Tx})^2 + (z_{iTx} - z_{Tx})^2}}{c_1} \tag{3.11}$$

and

$$\tau_{iTx-p} = \frac{\sqrt{(y_p - y_{iTx})^2 + (x_p - x_{iTx})^2 + (z_p - z_{iTx})^2}}{c_2} \tag{3.12}$$

In parallel, Equation 3.6 is separated into

$$\tau_{p-iRx} = \frac{\sqrt{(y_{iRx} - y_p)^2 + (x_{iRx} - x_p)^2 + (z_{iRx} - z_p)^2}}{c_2} \tag{3.13}$$

$$\tau_{iRx-Rx} = \frac{\sqrt{(y_{Rx} - y_{iRx})^2 + (x_{Rx} - x_{iRx})^2 + (z_{Rx} - z_{iRx})^2}}{c_1} \tag{3.14}$$

The amplitude of a pixel located in a 3D co-ordinate system, when imaging through a planar surface is then

$$I = \left| \sum a_{Tx,Rx} \left(\tau_{Tx-iTx} + \tau_{iTx-p} + \tau_{p-iRx} + \tau_{iRx-Rx} \right) \right| \tag{3.15}$$

This is an important module for TFM, and is essential for imaging with 2D arrays. Demonstration of the execution of this algorithm for the configuration shown in Figure 3.16 is shown in Figure 3.17. A 5MHz 2D matrix array was used to inspect the component with a 25mm water gap. The array has a pitch of 1mm in both the primary and secondary axis, with 32 and 4 elements in the primary and secondary axis respectively. The image in Figure 3.17 is a 2D slice constructed at the centre of the secondary axis of the array, as highlighted in orange in Figure 3.16. All three SDH and the BW are identified and positioned correctly, confirming the algorithm is successfully accounting for refraction through the interface.

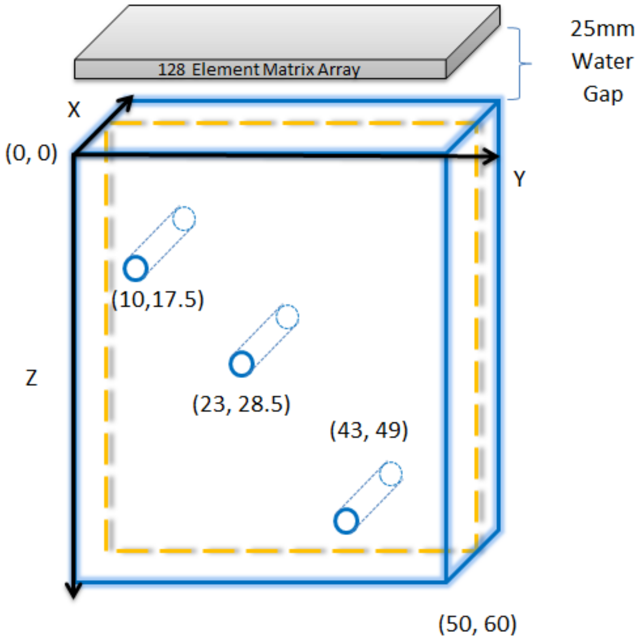

Figure 3.16: Experimental set-up to demonstrate TFM using a 2D array with refraction. Three SDH at various depths are imaged by a 2D matrix array. The region in orange highlights the 2D slice shown in Figure 3.17.

In Figure 3.17 the probe is positioned between -12 and +12mm and the imaging window is slightly wider than directly below the probe in this image to allow all 3 SDH to be detected. The best imaging performance is directly below the probe and outside of this region the performance degrades slightly. This is recognised through curving of the BW and skewed SDH responses at the edges of the image.

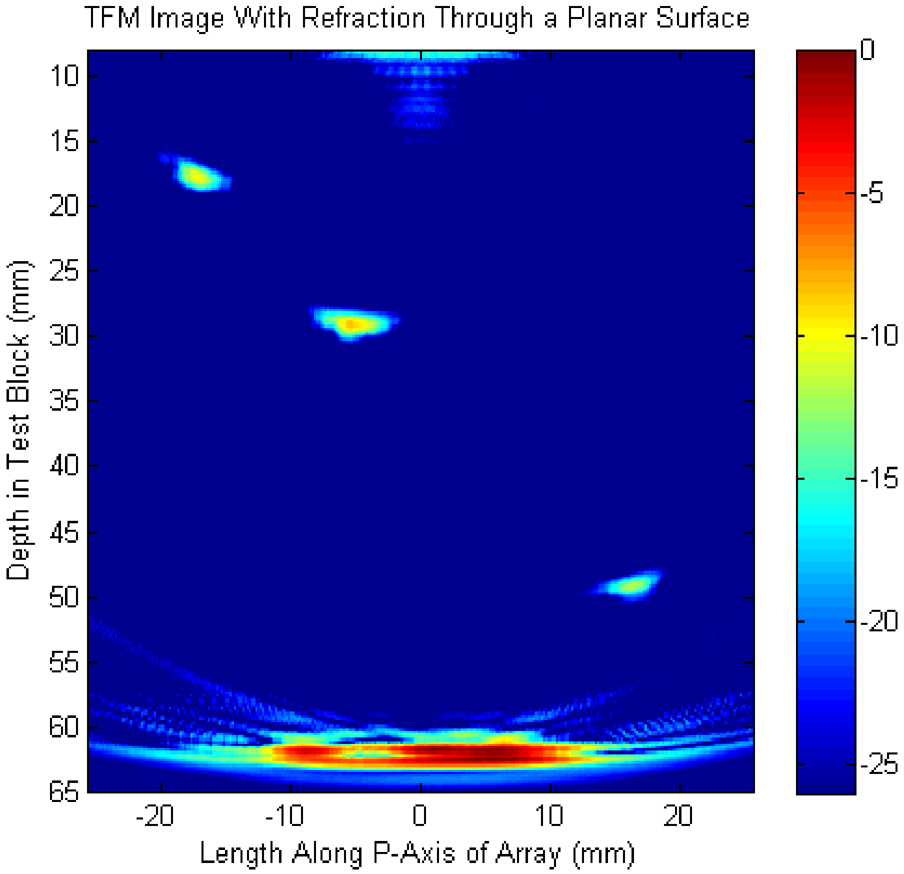

FIGURE 3.17: 2D TFM Slice at the centre of a 2D matrix array resulting from the experimental set-up in Figure 3.16.

3.4.2 TFM Through an Arbitrary Interface

Inspections are not restricted to components with planar surfaces, and so TFM must be able to deal with refraction through an arbitrary interface [65]. Unlike the planar case, there is no closed form solution to locate the point of refraction. Instead it is an iterative process, and can therefore be computationally expensive.

Fermat's Principle explains that ultrasound takes the shortest path from any given start to end point. In this context this relates to the shortest time from one point to another through an interface. An efficient solver, harnessing the power of GPU, has been developed to identify the point of refraction according to this principle. A mathematical description of the surface is required, to inform the algorithm where the interface lies. The author helped establish that the most stable manner of representing the surface for this process as a height map at specified increments along the y-axis. The process involves iteratively seeking the PoR by evaluating the ToF at a range of points on the surface. Figure 3.18 illustrates the initialisation of routine, where an initial guess at the PoR y_{PoRg} on an arbitrary surface is taken as the midpoint of the y-axis position of the transmitter and pixel, referred to as y_{PoR1} and y_{PoR2} on the diagram. Interpolation is used to approximate the surface height where is it not stipulated by the height map. The solver continues to search for the PoR by iteratively checking positions on the surface between y_{PoR1} and y_{PoR2} until the minimum ToF between start and end point is achieved, returning the identified PoR. Once the point of refraction is located, the algorithm operates as described for the planar surface.

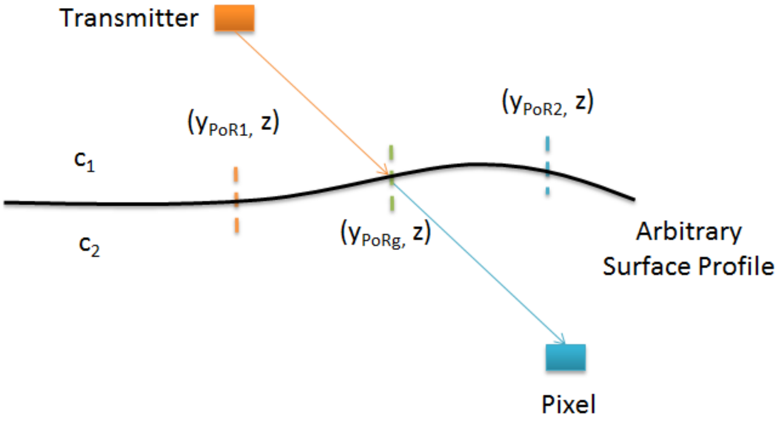

FIGURE 3.18: Initial guess of the PoR in the case of an arbitrary surface profile (in 2D).

An example of TFM through a known arbitrary interface is demonstrated using the experimental set up in Figure 3.19. The TFM image in Figure 3.20 was achieved using the 1MHz 2D matrix array to collect FMC data in immersion, with a 35mm water gap between the probe and surface. The surface profile was defined from engineering drawings of the test block and subsequent measurements. The profile was articulated to the TFM algorithm in increments of 0.5mm along the y-axis. The surface form was concave with respect to the probe, with a dip of around 2mm in the centre of the probe as illustrated on Figure 3.19. The TFM image in Figure 3.20 displays the geometry of the surface, at a depth of 0mm, and correctly positions the 2 SDH and BW in the component. This result confirms correct implementation of TFM incorporating refraction of a known surface and also indicates that the surface geometry can be imaged using TFM.

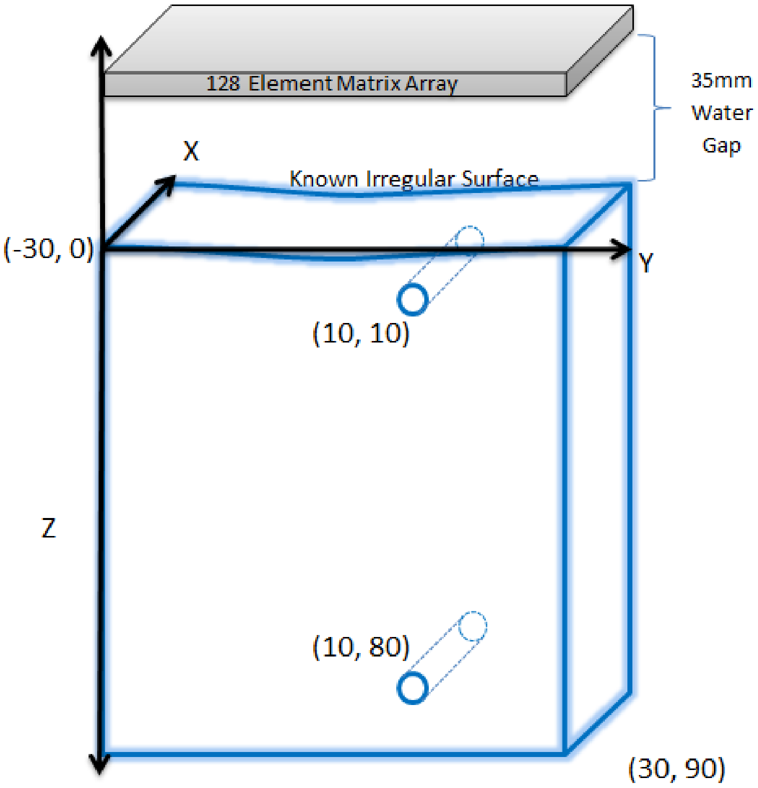

FIGURE 3.19: Experimental set-up for TFM through a known arbitrary surface. A 90mm thick test block with a known surface profile and two 3mm SDH is inspected with a 2D array.

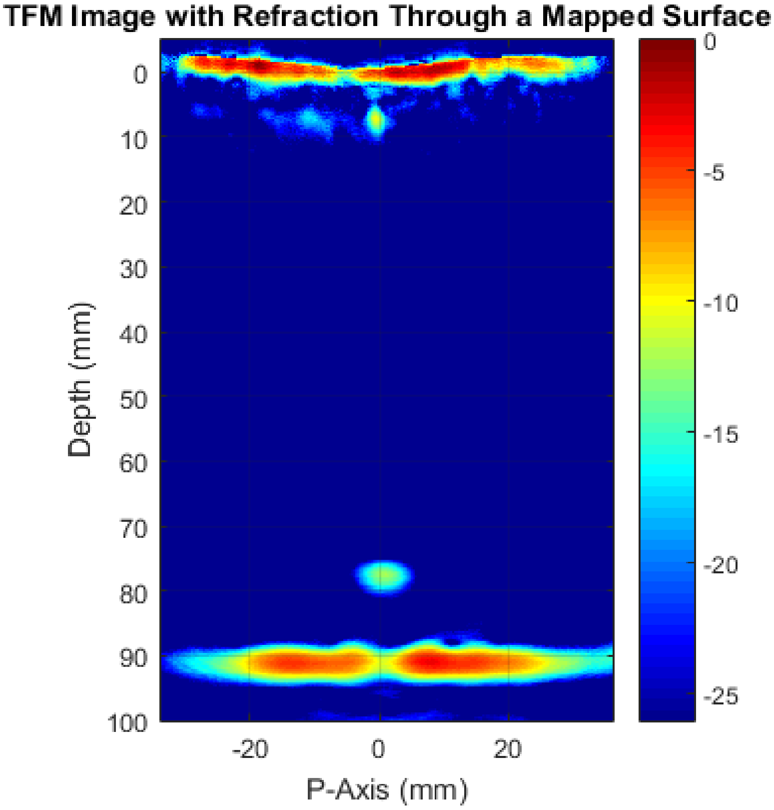

FIGURE 3.20: TFM image for experimental set-up shown in 3.19. Two SDH and the BW are image correctly.

Imaging through a surface evolving in all 3 dimensions is possible following the same methodology used in the 2D case. A height map of the surface over x and y is required and 2D interpolation is used instead of linear interpolation to identify the PoR. In this case the ToF solver is iterated over an area on the surface, as highlighted in green on Figure 3.21. The 4 corners on the surface are defined by the x and y locations of the transmitter or receiver and the pixel. Using Figure 3.21 as an example, the four corners of the area would be (x_{Tx}, y_{Tx}), (x_{Tx}, y_P), (x_P, y_{Tx}) and (x_P, y_P). This relates to the area on the surface enclosed by the transmitter and the pixel. The same is true for the pixel and receiver.

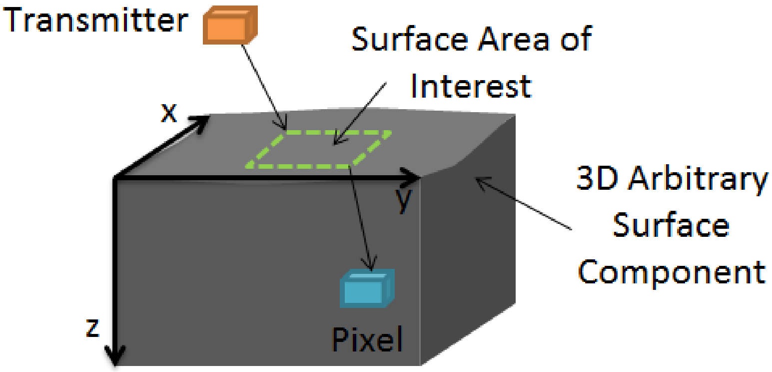

Figure 3.21: Illustration of how the PoR is determined in the case of a fully 3D arbitrary surface.

A model incorporating the surface profile of an in-situ component with a surface form varying in all directions was created in CIVA and used to validate this method for imaging through a fully arbitrary surface. A 2MHz matrix array of 2.5mm element pitch, with 16 and 8 elements in the primary and secondary axis respectively was specified. The model of the component used surface profile data obtained from previous inspections and three 3mm SDH were placed throughout the component as in Figure 3.22. The surface profile for the region under the probe was specified to the TFM algorithm. A slice through the centre of the secondary axis of the array is shown in Figure 3.23, where the BW and SDH positions are indicated by the white overlay. Each of the SDH are identified and positioned correctly, however the shape of the response from each of the holes is different. It is expected that this is due to the varying surface creating a focusing or defocusing effect. The impact of the surface profile on imaging with TFM is considered further in Chapter 6.

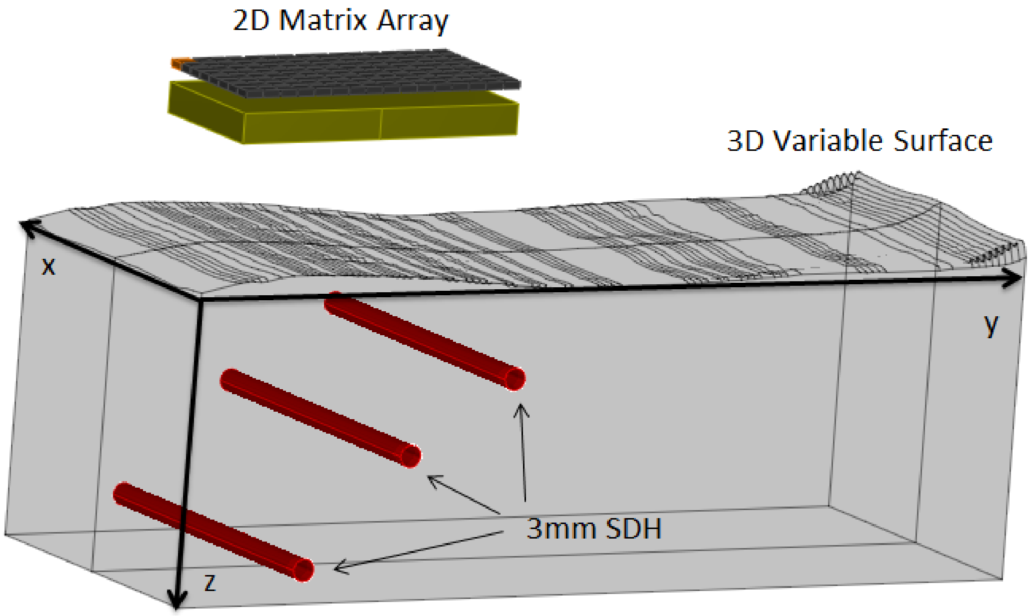

FIGURE 3.22: Model of component with a surface evolving in both the primary and secondary axes. Three 3mm SDH are placed throughout the component as it is inspected using a 2D matrix array.

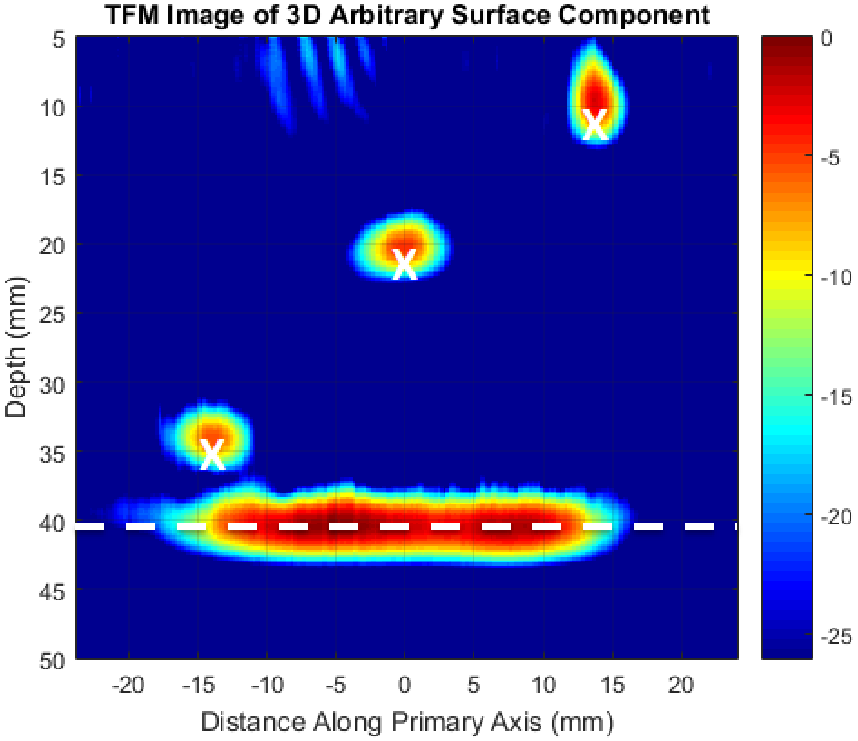

FIGURE 3.23: TFM image of the component shown in Figure 3.22 with a 3D variable surface. Three SDH and the BW are correctly identified.

3.5 Discussion

A thorough account of the mathematical calculations involved in creating a TFM image has been given. The steps taken to achieve an economical execution of TFM are identified and documented. The algorithm has been implemented systematically for various inspection scenarios, from the simplest where a linear probe is in contact with the component, to the most complex where a 2D array is used to image a component of a known, irregular surface profile. A comprehensive understanding of the inner mechanisms of TFM on GPUs has been achieved by the author, providing a foundation for the work completed in the remainder of this Thesis. The author contributed towards the development of this implementation of TFM mainly through the handling of surface geometry. The author played a vital role in the development through trials and demonstration of the technique using experimental data. Furthermore the author established a method for imaging through surfaces varying in all directions, which is essential for applying TFM to real components.

The TFM algorithm is now suitable for imaging components of irregular surface profile. However, a known profile has been assumed thus far. It is not always feasible to have a true representation of the surface profile of in-situ industrial components. The following Chapter examines surface detection methods and mathematical descriptions of the surface. Moving forward this allows on-the-fly inspection of components with an unknown surface profile.

Chapter 4

Dynamic Surface Detection and Reconstruction

Components requiring inspection often present irregular and complex surfaces and a dynamic method for detecting and reconstructing such interfaces is sought in this Chapter. Innovative imaging algorithms, such as TFM, offer a solution to inspecting complex components. However, an accurate description of the inspection surface is required for these algorithms to operate effectively. A double TFM system is presented here, whereby a TFM image is initially created around the component surface, followed by surface extraction. This is then relayed to the algorithm to create a corrected TFM image of the component.

The bespoke test block introduced in Chapter 1 is shown again in Figure 4.1. This block has a specific surface profile intended to represent the worst acceptable error of form for a component requiring ultrasonic inspection [66]. The error of form refers to undulations in the surface height of 2mm over 60mm in length. Three regions are identified on the test block in Figure 4.1 and these are used throughout the Chapter to identify areas of the block for which imaging has been performed.

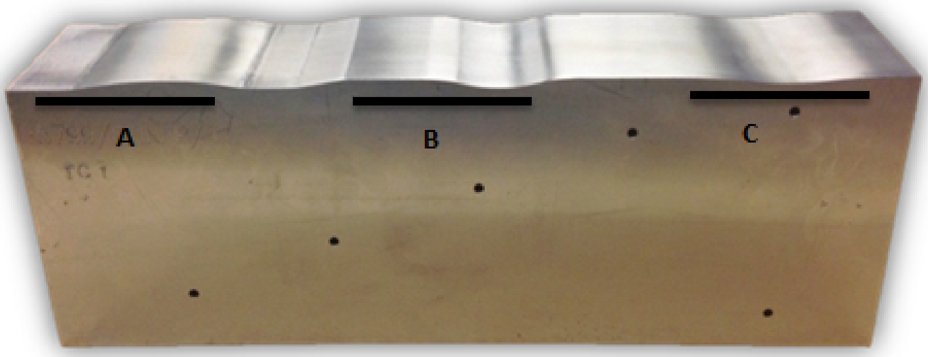

FIGURE 4.1: Bespoke test block with positions A, B and C highlighted for use in this Chapter.

Unless otherwise stated, the data presented in this Chapter was collected using this test block in an immersion tank, using an automated X-Y scanner to position the probe. A 1MHz 128 element, 2D matrix array was used to collect FMC data parallel to the flat BW of the test block. Appendices A and B provide more detail on this test block and probe respectively. The Micropulse 5 (MP5) PAC (Peak-NDT, UK) was used for excitation and data collection, with a sampling frequency of 10MHz.

4.1 On-the-fly Surface Detection

A cost-effective technique for determining the surface profile of a component is sought to permit automatic correction of the ToF calculations in TFM. There are a number of possible approaches to establish the surface profile, each with their own benefits and limitations. Preferably the method should not significantly increase inspection or data processing time and additional apparatus should be kept to a minimum.

One accessible and proven method would be to employ a profilometer [67], which is a commercially available instrument that measures the surface profile by utilising either a stylus or optical methods [68, 69]. Potentially, the profilometer could scan the surface alongside the ultrasonic inspection, with the profile being conveyed to the ultrasonic imaging algorithm in parallel. However, this would mean extra apparatus in the region of the inspection, which can be restricted. Additionally, there is a risk of errors being introduced when referencing the profilometer with respect to the inspection data. The probe is often positioned manually by the operator at the start of a scan and the exact reference position may vary slightly from one inspection to another. Furthermore the probe or profilometer may displace with respect to one another.

Several studies have considered flexible ultrasonic probes that conform to the surface [7, 70], removing the requirement to know the surface profile. These have been demonstrated successfully in the laboratory environment but may be lacking the robustness and flexibility required for an industrial inspection. They rely on advanced electronics to account for changes in the surface geometry, with pistons pressing the elements on to the surface. The extent to which they can conform to the surface is limited by the element size and configuration. Additionally, it can be difficult to generate shear waves with such probes, restricting the inspection possibilities.

Ideally, the surface profile should be determined from the data collected for the inspection. Initially, the Pulse-Echo (P-E) data is considered. In the FMC this relates to the diagonal within the matrix, where the transmitting and receiving elements are the same. P-E is typically used in ultrasonic thickness gauges [71, 72], therefore potentially offering a straightforward solution to surface profile detection. This works well when the inspection surface is planar. However, it collapses for the geometries considered in this study due to both the gradient of the surface and the beam-spread of the ultrasonic energy. These predicaments are illustrated in Figure 4.2. Two P-E scenarios are shown, with their transmitted and reflected beams shown in orange and green respectively. On the left of Figure 4.2, the energy is reflected to the element and the surface profile may be detected as in the illustrative time domain response shown in Figure 4.3. However, in the case to the right of Figure 4.2, where the gradient of the surface is extreme, no energy is returned to the probe and the surface cannot be detected at that point.

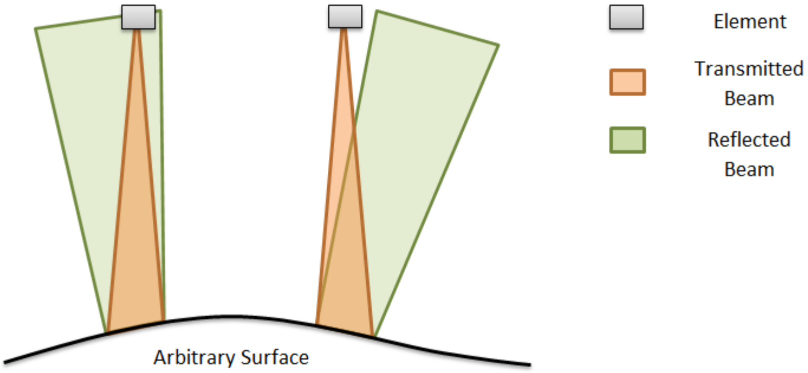

Figure 4.2: Illustration of two main issues using P-E to detect an arbitrary surface profile. On the left, the peak energy returning may not be from the point on the surface directly below the element. On the right, no energy may return to the element for extreme surface gradients.

An amplitude trace can be represented either as the raw response, rectified signal or envelope as shown in Figure 4.3. Where the amplitude of various peaks in the response are similar it becomes difficult to distinguish where exactly to take a measurement from. In particular beam-spread can induce ambiguity, since the strongest response may not arise from the surface directly beneath the element. Analysis of where the point arising from the surface is becomes open to user interpretation due to various peaks at a similar amplitude. A number of methods may be used including using a threshold or taking the peak of the envelope.

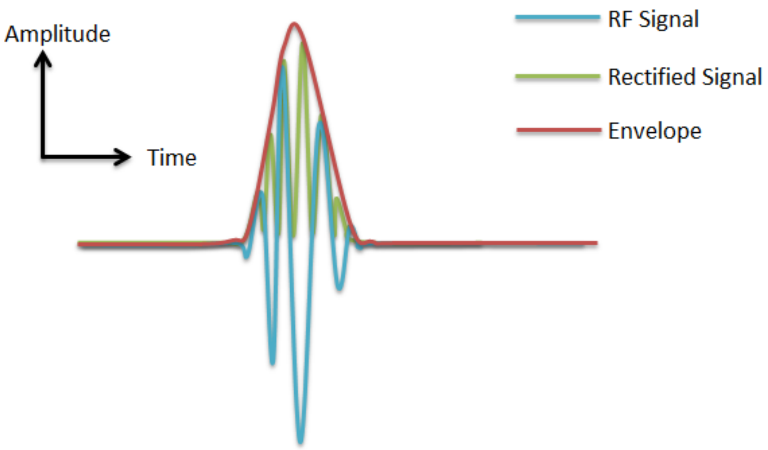

FIGURE 4.3: Example A-Scan representations including RF, rectified and the envelope allowing the signal to be interpreted in a number of ways.

4.1.1 Surface Extraction with TFM

An efficient method for determining the interface is accomplished by constructing a TFM image of the surface, as a reflector in the coupling medium, and subsequently extracting the profile. This is achieved using a portion of a single FMC data set acquired in an inspection, meaning no additional data or apparatus is required. This also avoids any referencing errors between instruments. This method is similar in principle to a SONAR voting system [73], which is successfully used to determine topography of unknown structures.

A small window of 10mm in height and the Primary Axis (P-Axis) length of the array is set to construct the TFM image of the surface. An example of this arrangement is shown in Figure 4.4. Here a dual media inspection is considered, where the probe is coupled by medium 1 through an interface to medium 2. An estimate of the offset between the probe and component surface is required, to position the surface at approximately zero in the z-axis. The TFM image is constructed using the velocity of medium 1 only, and no reference is made to the second medium at this point. The surface profile marked on Figure 4.4 for illustrative purposes only to indicate where the surface may be and no default surface profile is assumed.

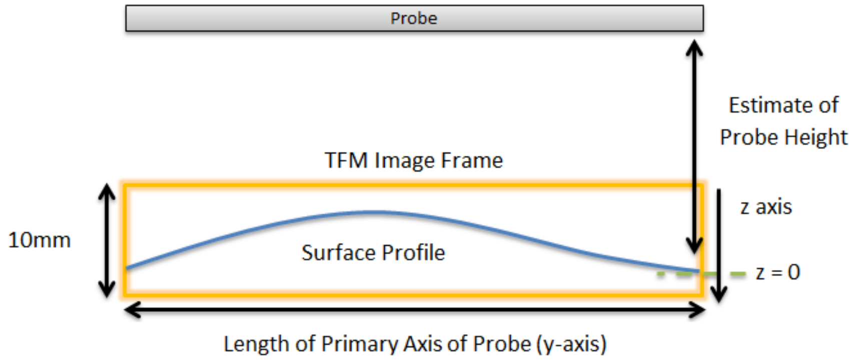

Figure 4.4: Schematic for creating a TFM image of the surface. An estimate of the probe height is required to position the surface at approximately zero in the z-axis.

Figure 4.5 shows the TFM image of the surface at position A on Figure 4.1. A resolution of 0.2mm was used in both the y and z axes, and the probe was positioned approximately 38mm above the test block in water. The region above the surface suffers from large artefacts which obscure the profile. Figure 4.6 shows the TFM image of a flat surface, the artefacts still arise in this case and it becomes clear that they arise due to the sidelobes from elements with large separations.

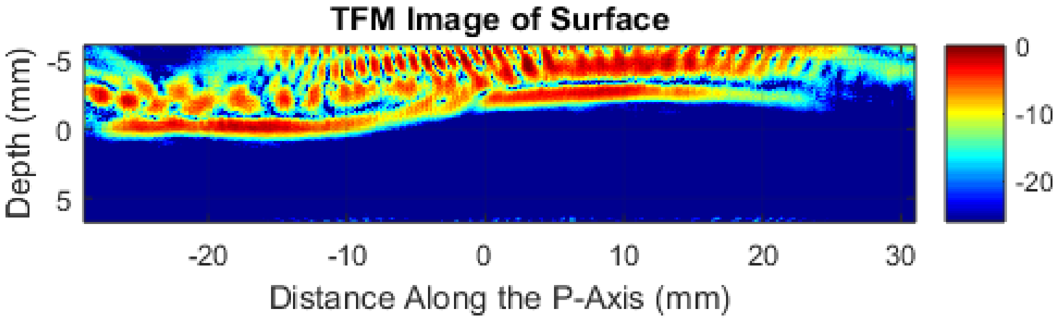

Figure 4.5: TFM image of the surface at position A on the test block. where the scale is in dB. Extensive reverberations obscure the surface profile.

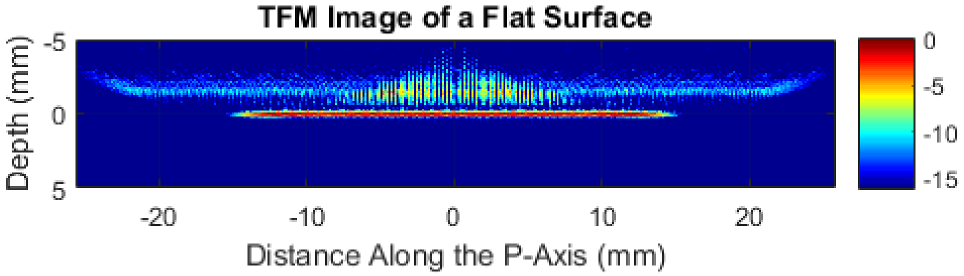

FIGURE 4.6: TFM image of a flat surface, illustrating artefacts arising above the surface due to the sidelobes from elements with large separations.

These artefacts can be avoided by effectively windowing the elements that contribute towards each pixel in the surface TFM image. Equation 4.1 defines the angle θ_{pixel} that arises due to setting W between 0 and 1, reducing the window from 90° to 0°. Figure 4.7 illustrates the windowing process in 2D with a linear array, and then Figure 4.8 extends this to 3D with a 2D matrix array. Here large angles relate to a greater number of elements in the window.

$$\theta_{pixel} = cos^{-1}(W) \tag{4.1}$$

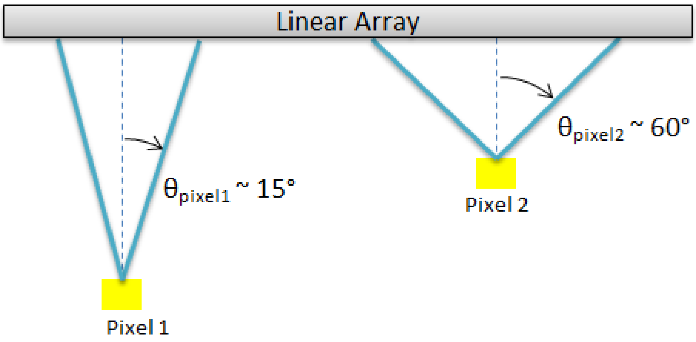

FIGURE 4.7: Illustration of the windowing process for surface TFM images. The 2D case is shown using a linear array.

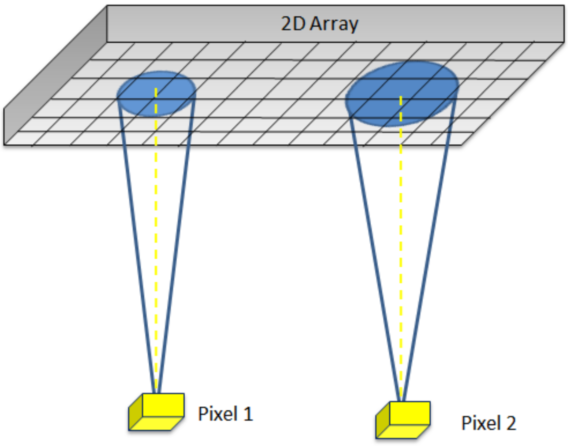

FIGURE 4.8: Example of pixel windowing in a 3D volume using a 2D matrix probe.

This routine means that only the FMC data from Tx-Rx pairs within the cone, specified by the angle limit, contribute towards the amplitude of a specific pixel. The elements, and therefore Tx-Rx pairs, change for each pixel in the image. The reasoning behind this method is that useful information is retained from elements directly above the surface, while interference from additional reverberations is avoided. This is effectively the Synthetic Aperture Focusing Technique (SAFT) [74], since only a portion of the available aperture contributes to each pixel in the image. Figure 4.9 gives an example of four stages of windowing, ranging from 25°, 15°, 10° and 5°. At angles above 25° very small effects due to the window are observed, and below 10° the surface profile begins to degrade significantly.

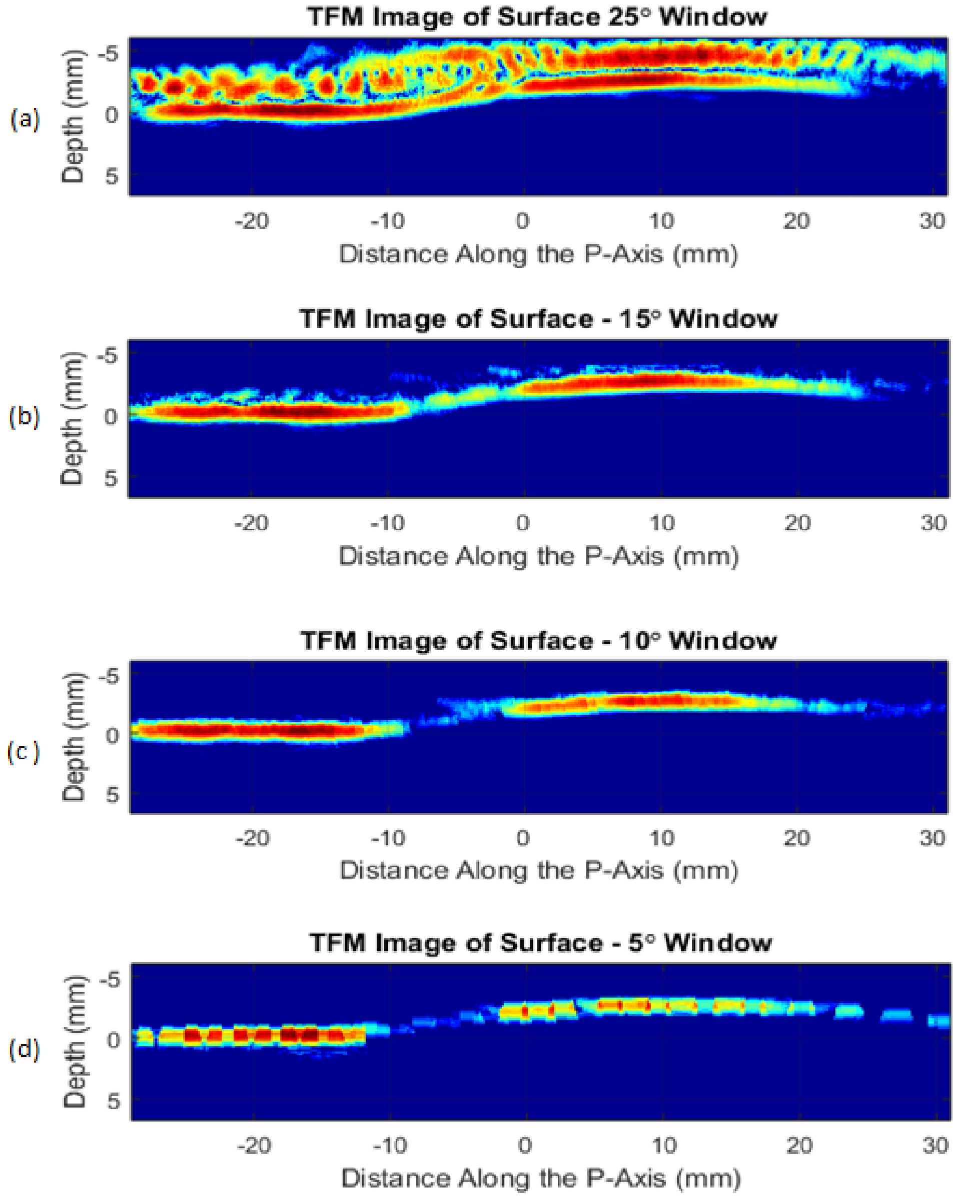

FIGURE 4.9: Four grades of pixel window ranging from 25° to 5°, where the interference from reverberations is removed to reveal the surface profile.

The best imaging performance occurs at 10° on Figure 4.9, where the reverberations have been removed and the surface profile is clearly visible. Windows 15 and 25° suffer from reverberations while the 5° window results in inconsistent amplitudes along the surface. A window of 10° relates to a value of $W = 0.9848$ and is the window chosen for this particular inspection set-up. This corresponds to around 12 elements, out of 128, contributing towards the amplitude of each pixel in the TFM image. These parameters may require modification for a different arrangement due to a number of variable parameters, including the probe used, coupling medium and probe height. As such the settings would be dealt with as part of the calibration process for each new inspection.

Now that the TFM image gives a good representation of the surface profile, the extraction method and threshold must be optimised to lead to an accurate reconstruction of the interface. First, considering the extraction method, three techniques were considered including the first peak, the mid-point and the strongest peak. Each of the methods handle data at each increment in the y-axis, and do not report a depth where no pixel exceeds the specified threshold. Pixels in the z-axis are defined as increasing away from the probe face, with first pixel closest to the probe. Initially, the first peak method returns the depth of the first pixel exceeding the threshold. For the mid-point case the first and last pixel exceeding the threshold are returned, and their centre is taken as the surface point. Finally, the strongest peak returns the depth of the pixel with the maximum amplitude. Figure 4.10 gives an example of these surface extraction methods at position A on the test block (see Figure 4.1). In general they are in agreement with the surface profile, however there are subtle differences. In comparing the extracted data with the actual surface profile, over a range of surfaces, the mid-point system performed best. The first peak appeared slightly too high at around 1mm closer to the probe than expected. The strongest peak method experienced spurious surface points at 0mm and 20-30mm along the primary axis.

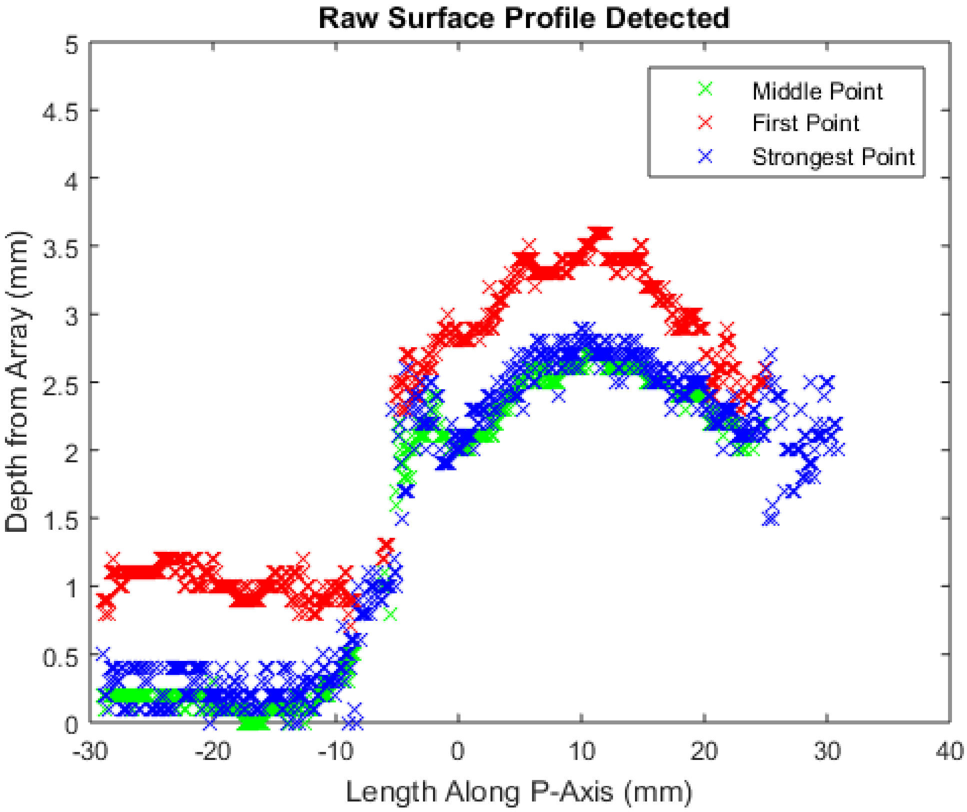

FIGURE 4.10: Comparison of methods for extracting the surface profile from the TFM data.

The choice of threshold at which to extract the surface also impacts on the quality of reconstruction. In this work, the dynamic range of the surface TFM images is set to 26dB, where the scale ranges from strongest peaks at 0 decreasing to -26dB. Figure 4.11 presents the raw surface points extracted from the TFM image using a range of thresholds from -6dB to -20dB. The extracted profile is consistent over the range of thresholds, however the extent of the profile is dependent on the threshold. At the lower thresholds, from -20dB to -16dB, good coverage is achieved but an artefact that does not appear on the real surface is detected in the centre. At the highest threshold, -6dB, poor coverage is achieved, meaning a large portion of the surface is not detected. The remaining thresholds both perform well, with -14dB giving slightly better coverage than -12dB.

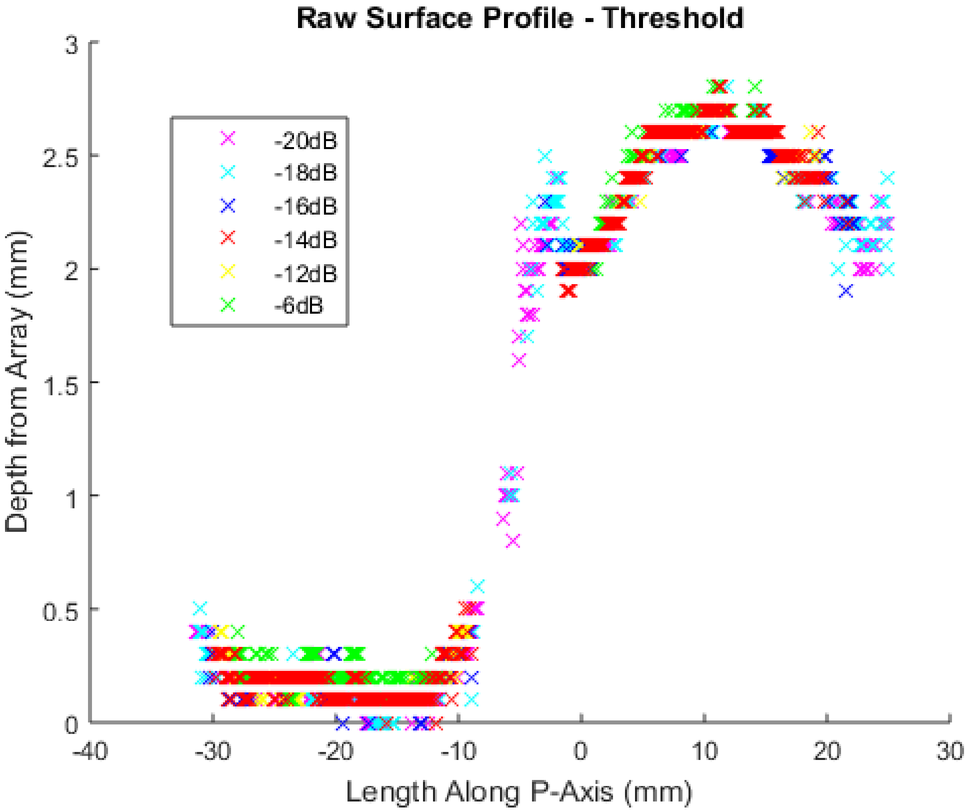

FIGURE 4.11: Comparison of the extracted profile using a range of thresholds, -6dB to -20dB.

The final extraction settings are therefore a pixel window of 10°, using mid-point extraction and a threshold of -14dB. Figure 4.12 shows a comparison of the extracted profile and real surface at position A, B and C.

The red crosses indicate the detected profile and the blue line is the true surface. It is noted that the surface detected at position C does not match the true surface form at the top left and dip in the middle. This may be explained by poor alignment of the probe above the surface, demonstrating the requirement of accurately representing the position of the elements in the probe. Overall, the extracted and real surface profiles are in good agreement, however there are sections where no interface was detected. Generally these relate to large gradients on the surface, which are intrinsically difficult to detect as mentioned previously.

Since this is a matter relating to the form of the surface, it is still relevant in the case of TFM and surface extraction. The following section employs mathematical approximations to complete the reconstruction of the surface profile.

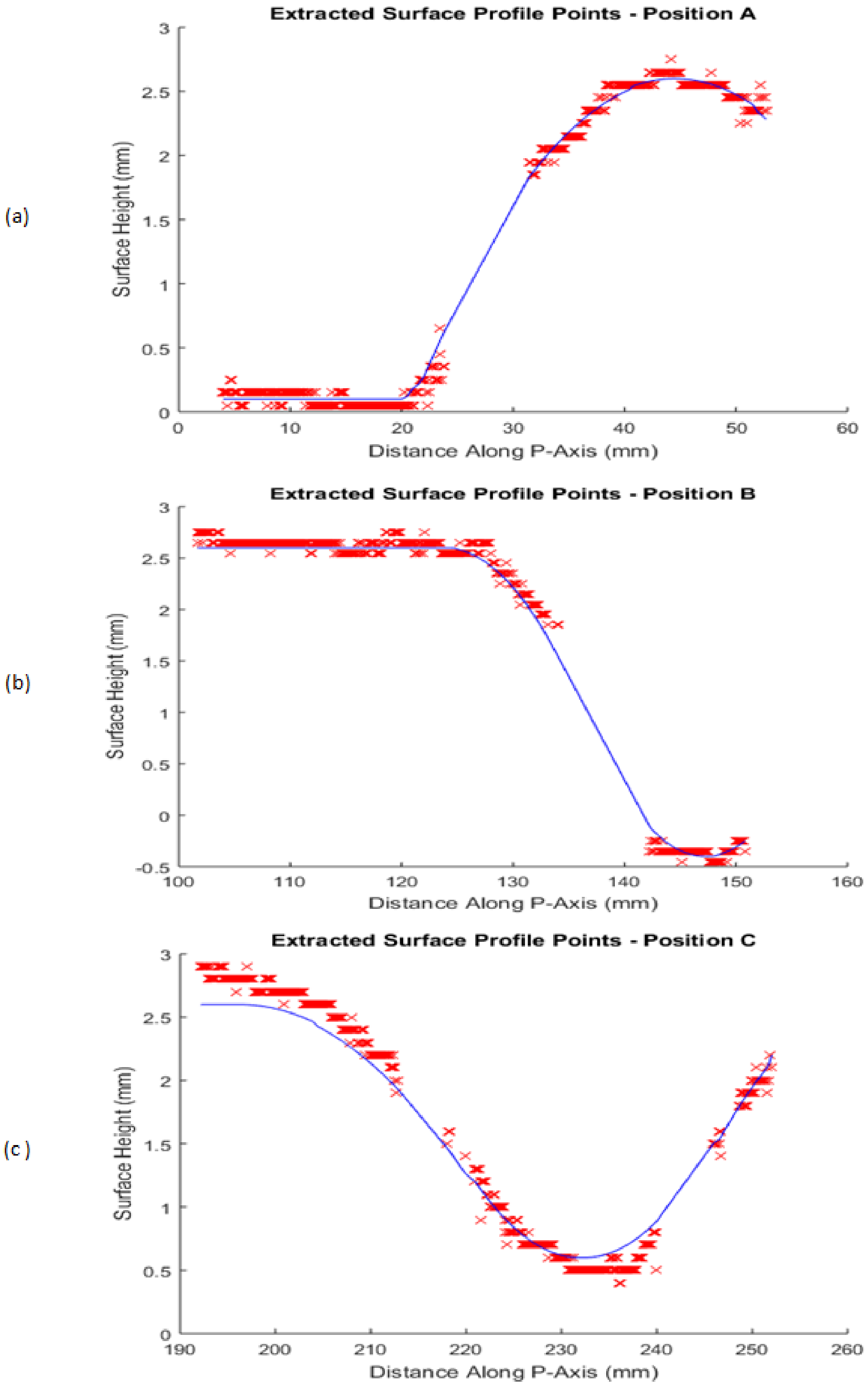

FIGURE 4.12: The raw extracted surface profile points (red) at positions A, B and C, compared with the true surface profile (blue).

4.2 Mathematical Description

A mathematical approximation is required to ensure a smooth and continuous profile. Previous studies relating to this topic have demonstrated the use of higher order polynomial equations for this purpose [5]. However, without known boundary conditions, these can tail off at the edge meaning the surface form is not correctly represented. Since no previous knowledge of the surface is assumed in this study, the edge conditions are unknown. This causes significant errors in the ToF calculations with the efficient TFM algorithm used here, due to the shortest path solver. This method also suffers where breaks in the raw surface data appear, often resulting in steps between known points, rather than smooth continuous profiles. An example of these issues is given in Figure 4.13, where an example surface profile is shown in green and the polynomial representation is shown in red. The problem areas are circled.

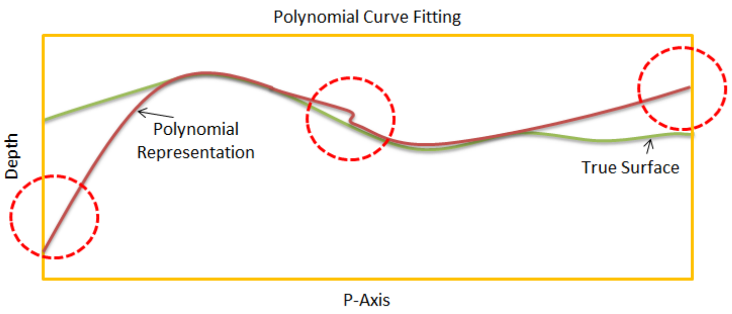

Figure 4.13: Illustrative example of the issues arising when using a polynomial description of the surface, including a step in the profile and tailing off at the edges.

4.2.1 Curve Fitting Methods

As introduced in Chapter 1, the surfaces considered in this study are polished smooth and continuous with relatively small undulations (less than 2mm). Various curve fitting methods were assessed for their suitability to such surface profiles, using the three positions indicated on Figure 4.1. These encompass the general and extreme behaviour of the surfaces considered, including convex, concave and planar regions. Out of the conventional curve fitting methods, combination sine waves, Fourier series and polynomials suit this problem most intuitively. Initially, trials using sections of the surface profile were performed to settle on the number of combination sine waves, Fourier series and order of polynomial to use, for the respective methods. These trials concluded that a three sequence sine combination and Fourier series, and 4th order polynomial present the best solution to such profiles. Their respective constructions are given in Equations 4.2 - 4.4, where y_i corresponds to the fit output for the input x_i of a typical function $f(x, y)$. The parameters M, N, ω, t and q relate to amplitude, frequency, offset and polynomial coefficients in turn. These parameters are dictated automatically using widely available curve fitting optimisation algorithms [75].

$$y_i = M_1 Sin(\omega_1 x_i + t_1) + M_2 Sin(\omega_2 x_i + t_2) + M_3 Sin(\omega_3 x_i + t_3); \tag{4.2}$$

$$\begin{aligned} y_i = M_0 + M_1 Cos(\omega x_i) + N_1 Sin(\omega x_i) + M_2 Cos(2\omega x_i) \\ + N_2 Sin(2\omega x_i) + M_3 Cos(3\omega x_i) + N_3 Sin(3\omega x_i) \end{aligned} \tag{4.3}$$

$$y_i = q_4 x_i^4 + q_3 x_i^3 + q_2 x_i^2 + q_1 x_i + q_0 \tag{4.4}$$

Figure 4.14 shows the fit from these 3 methods, referred to as Sine3, Fourier3 and Poly4, along with the raw extracted data points and the true surface profile. Overall, the three methods perform well in reconstructing the surface profile at each of the three positions, with sub-millimetre errors reported, with the exception of the maximum error at position B. A summary of the RMS error for each of the fit methods at each position is given in Table 4.1, and similarly with the maximum errors in Table 4.2.

Analysing these errors and the fit of the curves on Figure 4.14, it appears all three methods reconstruct the profile reasonably well without contradiction. Overall, the curves provide a good fit except for where the surface is flat, where the fit incurs numerous undulations around the raw data points. This effect is noticed particularly in plot (a) and (b) in Figure 4.14, where the extracted profile is reasonably flat, however the respective fitted curves are wavy. Although the errors between the fitted and true profile are small, the form of the surface is lost between the raw points that are extracted and the fit. Large errors in the surface profile would result in errors in the ToF calculation during the TFM processing and therefore image plotting. It was observed throughout this study that incorrect surface form resulted in higher image degradation than small errors in the surface height. The priority was therefore deemed to be on representing the surface form correctly, with sub-wavelength errors in the surface height considered acceptable. An alternative to curve fitting is sought to better represent the surface form by using a system that approximates the height of the surface at increments in the y-axis using the raw extracted points.

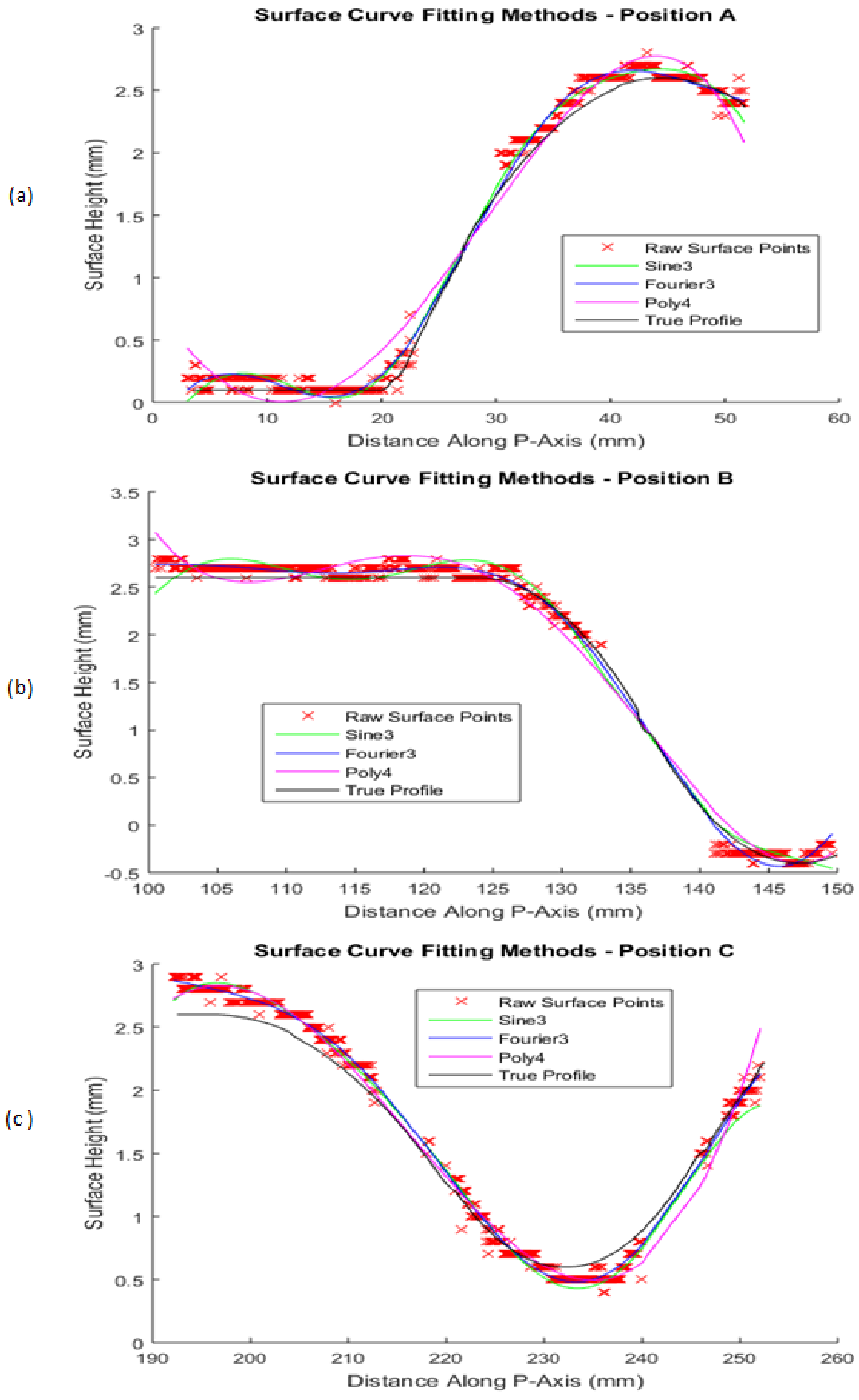

FIGURE 4.14: Comparison of curve fitting methods, Sine3 - green, Fourier3 - blue and Poly4 - magenta, at positions A, B and C. The raw extracted profile is marked by red crosses and the true profile is marked in black.

Method	**Position A (mm)**	**Position B (mm)**	**Position C (mm)**
Sine3	0.25	0.50	0.39
Fourier3	0.25	0.49	0.37
Poly4	0.20	0.44	0.38

Table 4.1: RMS error between the true surface profile and Sine3, Fourier3 and Poly4 curve fit solutions for positions A, B and C on the test block.

Method	**Position A (mm)**	**Position B (mm)**	**Position C (mm)**
Sine3	0.44	0.39	0.48
Fourier3	0.38	0.42	0.47
Poly4	0.45	0.49	0.51

Table 4.2: Maximum error between the true surface profile and Sine3, Fourier3 and Poly4 curve fit solutions for positions A, B and C on the test block.

4.2.2 Approximation Method

The approximation of the surface is performed in steps, starting with taking the mean height at specified increments in the y-axis, ignoring points where no surface point was detected. Interpolation is then used to fill in the missing surface points, and finally the surface profile is smoothed by using the 5 nearest neighbours on either side of each height point, to ensure a smooth continuous profile is achieved. This method is demonstrated on positions A, B and C in Figure 4.15, as before the raw extracted points are shown in red and the true profile is in blue. The approximation of the surface profile is then marked by green circles. This method performs well at all three positions, and avoids the unwanted undulations observed with the curve fitting methods. A summary of the RMS and maximum errors using this surface approximation is given in Table 4.3.

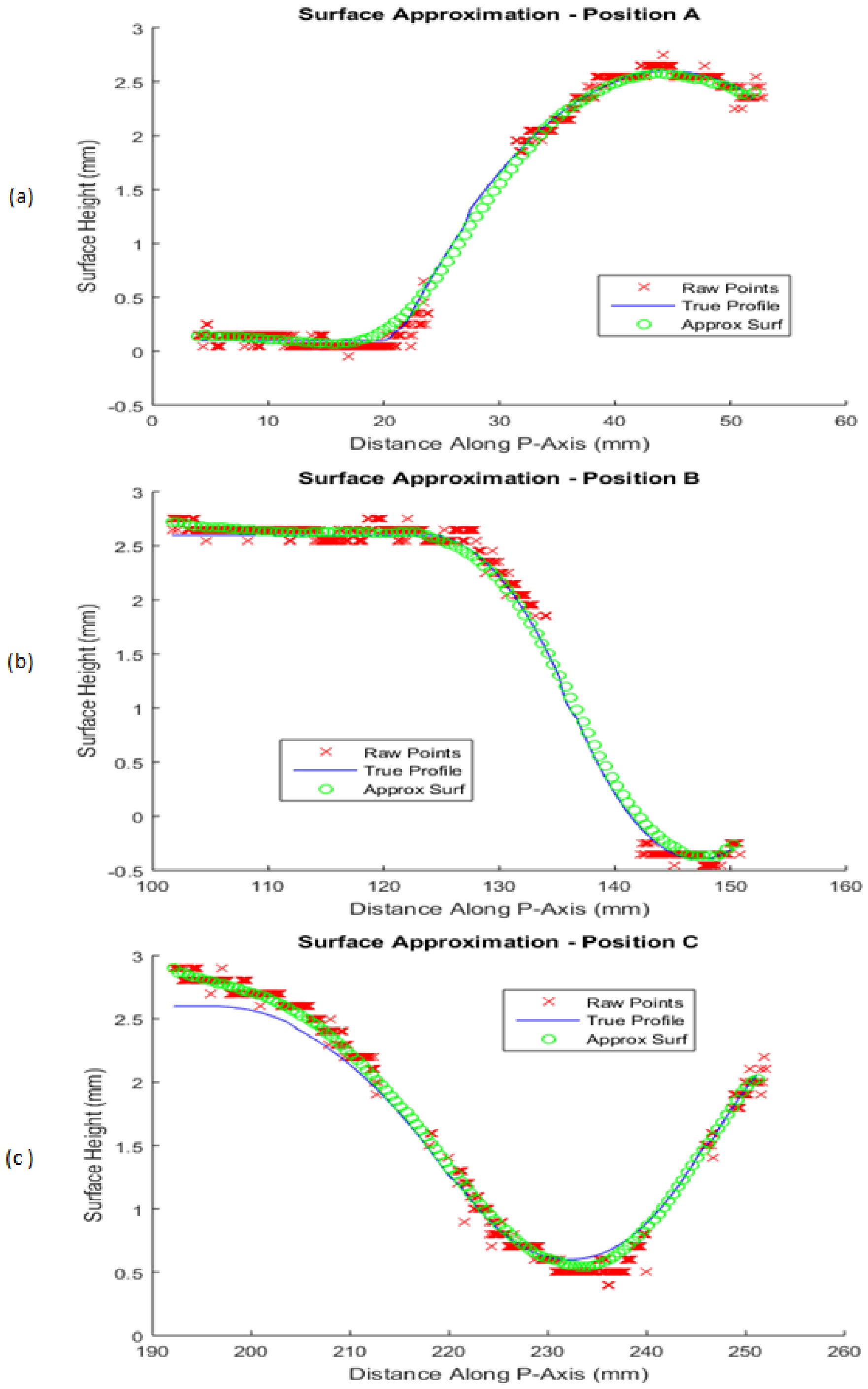

FIGURE 4.15: The surface profile achieved using the raw data (red) and then approximation method (green), at positions A, B and C.

Error	**Position A (mm)**	**Position B (mm)**	**Position C (mm)**
RMS	0.05	0.06	0.10
Maximum	0.11	0.13	0.30

Table 4.3: The RMS and maximum errors between the true surface profile and the approximation method for positions A, B and C on the test block.

Error	**Position A (mm)**	**Position B (mm)**	**Position C (mm)**
RMS	0.01	0.02	0.01
Maximum	0.20	0.24	0.26

Table 4.4: The RMS and maximum errors between the raw extracted profile and the approximation method for positions A, B and C on the test block.

The approximation method provides an exceptional representation of the true surface profile. The errors observed are significantly smaller than those obtained using any of the three curve fitting methods. The RMS errors for all three surface conditions using the conventional curve fitting methods was around 0.4mm whereas they are at most 0.1mm with the approximation method. Similarly, the maximum errors between the true surface and curve fitting methods are much larger than with the approximation method, decreasing from around 0.7mm for the curve fitting methods to around 0.2mm for the approximation method. It is therefore chosen as the method to transform the raw extracted profile points into a complete surface profile. The three positions that this method has been demonstrated on thus far were chosen due to their complexity, meaning they encompass the most difficult forms of surface this method will be required to deal with in the practical industrial environment associated with this EngD. Therefore, providing that a reasonable view of the surface can be obtained in the TFM image, this method should perform well on all similar surfaces encountered in practice.

4.2.3 Reconstruction Evaluation

In order to evaluate this surface detection and approximation method, the full length of the test block in Figure 4.1 was interrogated. Where 0mm refers to the left-hand side, and 255mm is the right-hand side. The result is shown in Figure 4.16, where the profile approximation is shown in green and the true surface profile is shown in blue. This demonstrates that the method is suited to surfaces typical of those represented by the bespoke test block. The resulting profile is in good agreement with the true surface over the full length of the block. A summary of the RMS and maximum error along the complete block is given in Table 4.5, where the mean maximum error was 0.21mm and the mean RMS error was 0.09mm. These considerably small errors confirm the surface detection and approximation method is suitable for purpose, as it is able to reconstruct the surface profile with a high level of accuracy.

Y Axis Position (mm)	**RMS Error (mm)**	**Maximum Error (mm)**
0 - 60	0.07	0.16
15 - 75	0.07	0.15
30 - 90	0.10	0.22
45 - 105	0.24	0.40
60 - 120	0.06	0.16
75 - 135	0.06	0.15
90 - 150	0.06	0.14
105 - 165	0.10	0.18
120 - 180	0.14	0.34
135 - 195	0.05	0.10
150 - 210	0.07	0.21
165 - 225	0.14	0.26
180 - 240	0.08	0.19
195 - 255	0.07	0.14
Mean	**0.09**	**0.21**

TABLE 4.5: The RMS and maximum errors between the true surface profile and the approximation method along the length of the test block. The mean of each of the errors is then given across the complete inspection range.

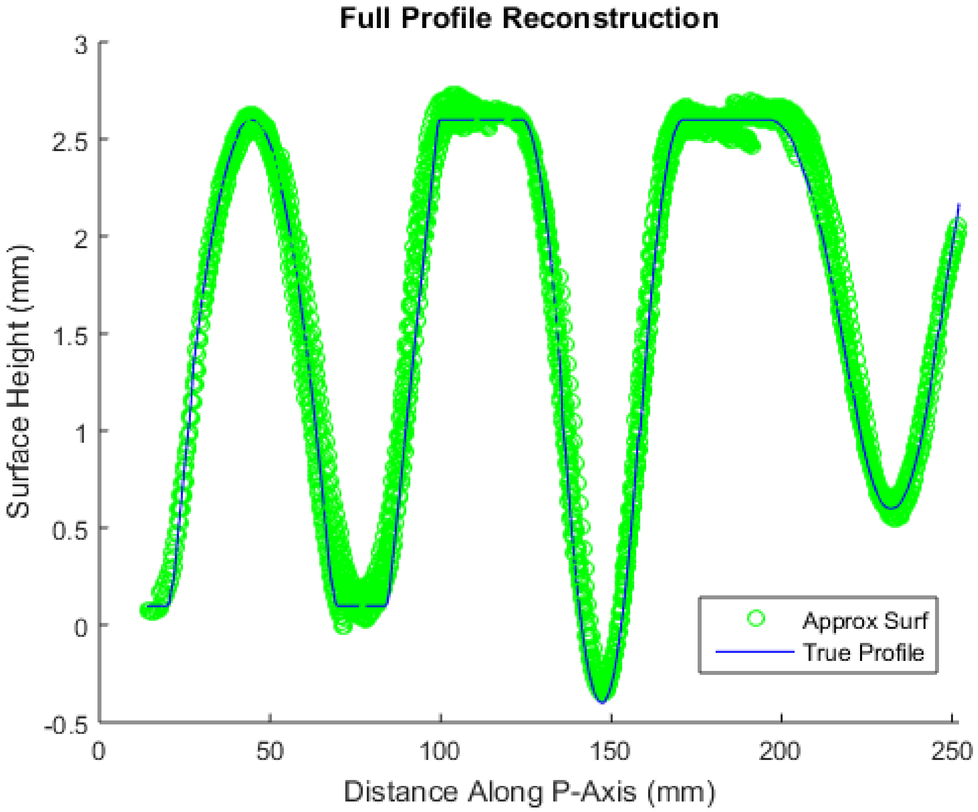

FIGURE 4.16: Reconstruction of the surface profile along the complete length of the test block. The approximation of the profile is shown in green, and compares well with the true surface profile (in blue).

4.3 Automatic Correction TFM

Automatic correction of the TFM image can now be achieved using the extracted profile. No additional user control is required for this correction, since the method only requires an approximate offset of the probe from the component. Figure 4.17 shows the TFM image of the surface at position A, B and C on the test block, respectively. The black dashed line indicates the extracted profile in each case, which is in good agreement with the profile visible on the TFM image, as predicted.

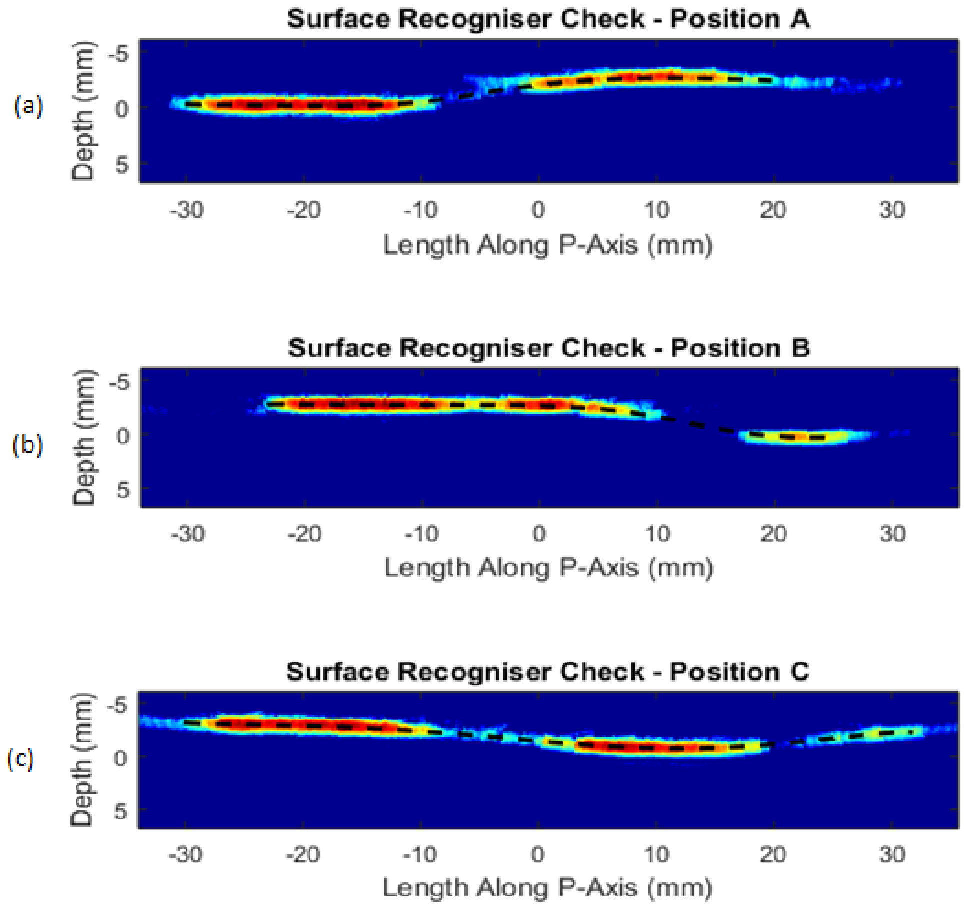

Surface Recogniser Check - Position A

Surface Recogniser Check - Position B

Surface Recogniser Check - Position C

FIGURE 4.17: TFM image of the surface at position A, B and C, where the black, dashed line indicates the extracted profile.

Figures 4.18 - 4.20 each show the TFM image at their respective positions on the test block where (a) a planar interface is assumed and (b) where the extracted surface is corrected for. In all 3 (a) images, the BW is obscured and it would be difficult to analyse the number and position of the flaws in the image. Conversely, the (b) images each show a flat BW and the SDHs that should appear in line with their positions indicated on Figure 4.1. The BW appears correctly at 93mm in each of the images. In Figure 4.18 one SDH appears just below 70mm. In Figure 4.19, one main SDH appears at around 35mm, with another just on the left hand edge at 50mm. Finally in Figure 4.20, two SDHs appear, one near the surface at approximately 5mm and another close to the BW at 80mm. These images were obtained using the automatic detection and approximate profile correction and thus confirm the method executes correctly.

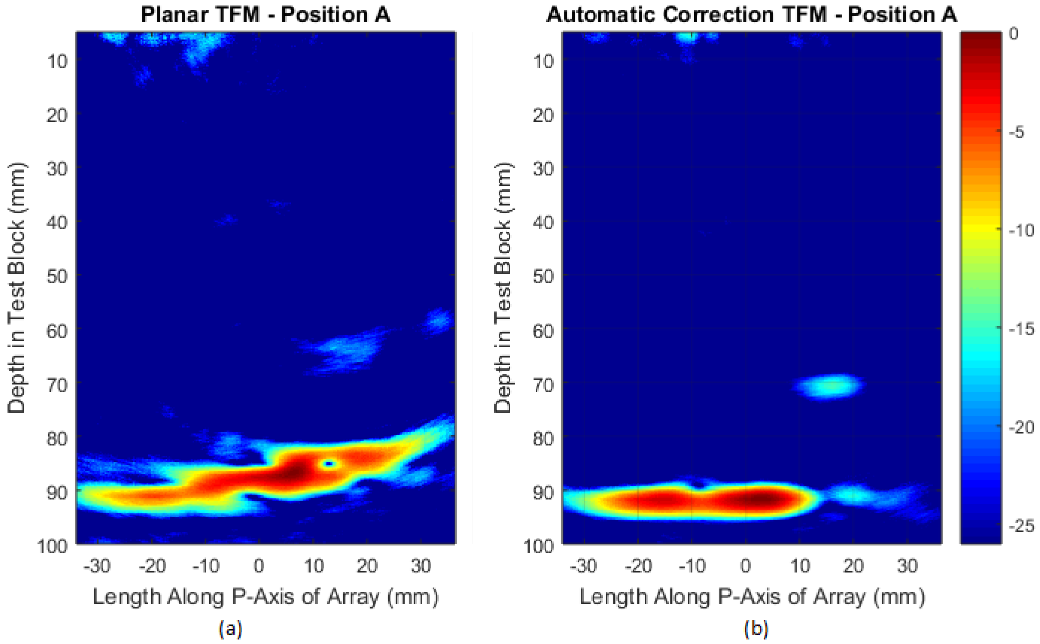

(a)

(b)

Figure 4.18: TFM images using a (a) planar surface (b) corrected surface at Position A on Figure 4.1.

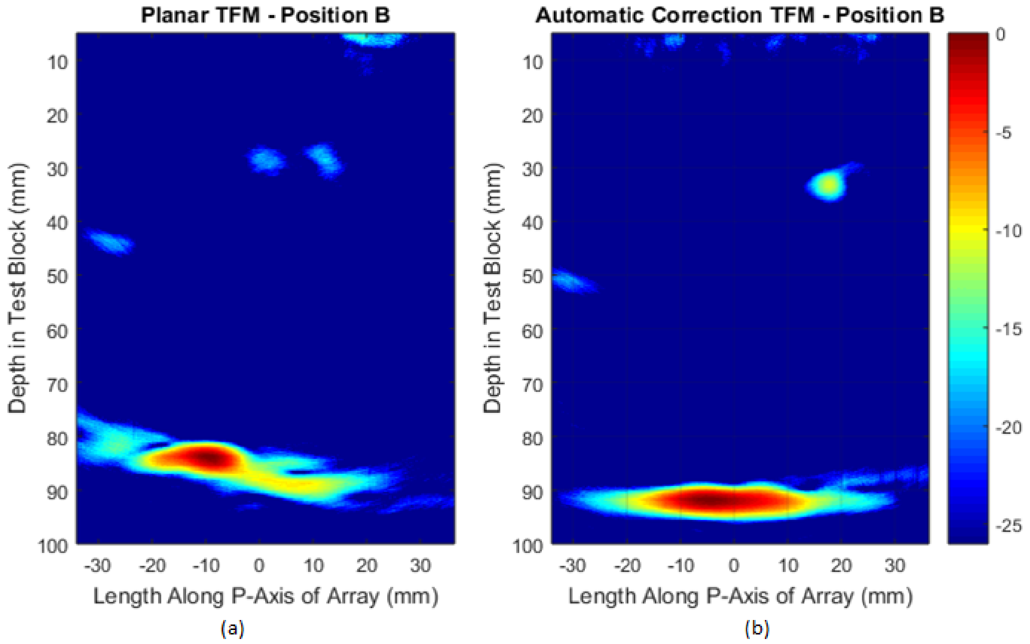

(a)

(b)

FIGURE 4.19: TFM images using a (a) planar surface (b) corrected surface at Position B on Figure 4.1.

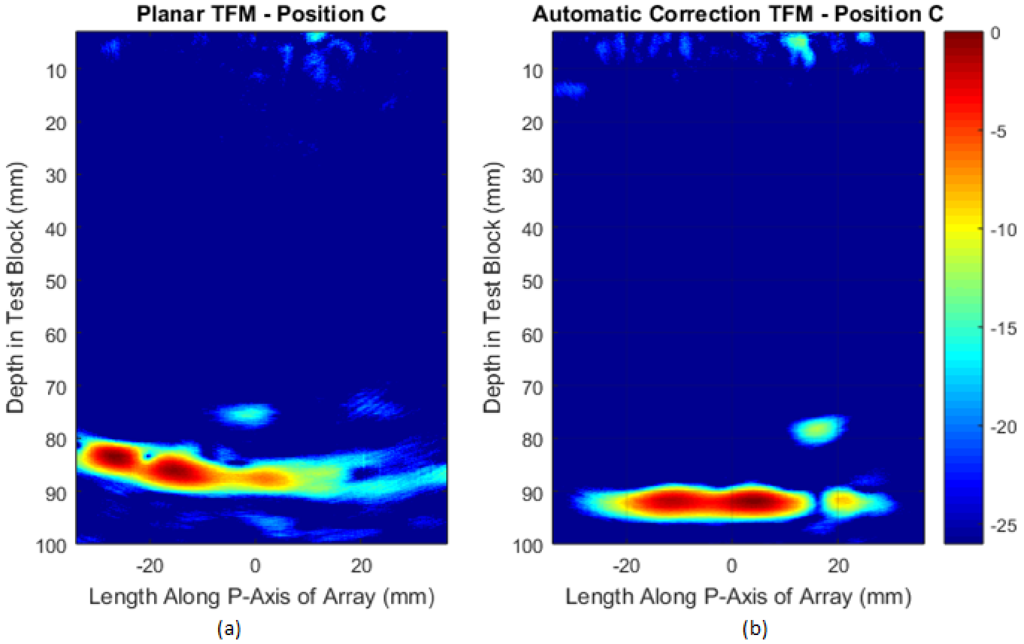

(a)

(b)

FIGURE 4.20: TFM images using a (a) planar surface (b) corrected surface at Position C on Figure 4.1.

4.4 3D Surfaces

Until now, only surfaces that vary along the primary axis of the probe have been considered, where the profile is effectively extruded in the secondary axis. Interestingly, the methods used to perform the automatic correction of TFM in 2D can be easily extended to include the 3rd dimension. The process followed is as described in Chapter 3, when creating 3D TFM images using slicing in the 3rd dimension. In this case, the surface profile is extracted at each increment in the x-axis, as a function of z and y. A complete map of the surface over the inspection region is then achieved. The approximation method is applied as in the case of the 2D surface to ensure full reconstruction of the surface profile in the y-axis. Smoothing is then performed over the surface profile in the x-axis to ensure a complete representation of the surface is achieved. The TFM process is then performed as described in Chapter 3 for the case of a fully variable surface.

The surface profile extracted using a 2D matrix array operating at 2MHz, with a pitch of 2.5mm in both the primary and secondary axes of 16 and 8 elements respectively, is shown in Figure 4.21. The CIVA model shown in Figure 3.22 in Chapter 3 was used to simulate FMC data for this case and demonstrate surface extraction in the primary and secondary axes, and subsequent automatic correction of the TFM image. A colour map of the surface height over the primary and secondary axes is shown in Figure 4.21, where the surface follows a smooth curve from around 0.25mm to -2mm over 40mm in the primary axis. A cross section of this data is shown for clarity in Figure 4.22. The main change in the surface profile is in the direction of the primary axis of the probe, however small undulations are noted along the secondary axis.

The extracted surface was compared with the true surface profile with the result shown in Figure 4.23 over the primary and secondary axes. The surface extraction method performs well with errors mainly in the rage of 0.1mm, illustrated by the accompanying colour map. Although this is an idealised case due to a simulated model, this result is encouraging and illustrates that full 3D surface extraction and replication with high accuracy is feasible. The corrected TFM image is shown in Figure 4.24, which is in good agreement with Figure 3.23 where the true profile was used.

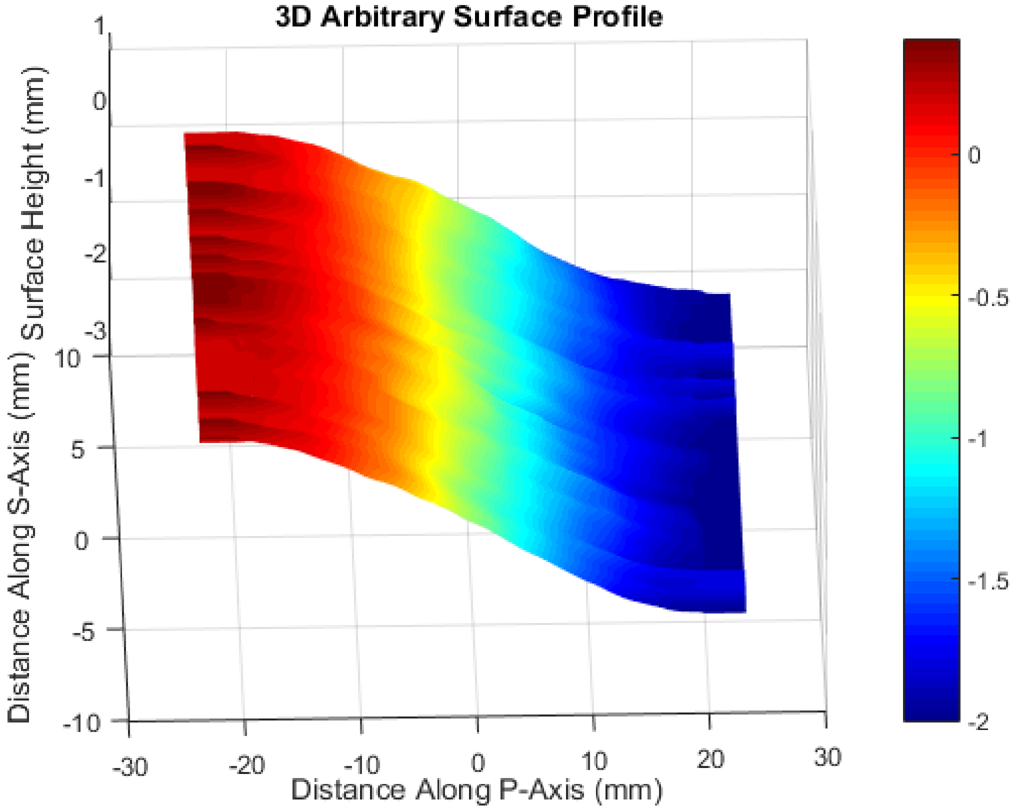

FIGURE 4.21: Colour map of the 3D surface extracted for the model shown in Figure 3.22. The scale is in mm.

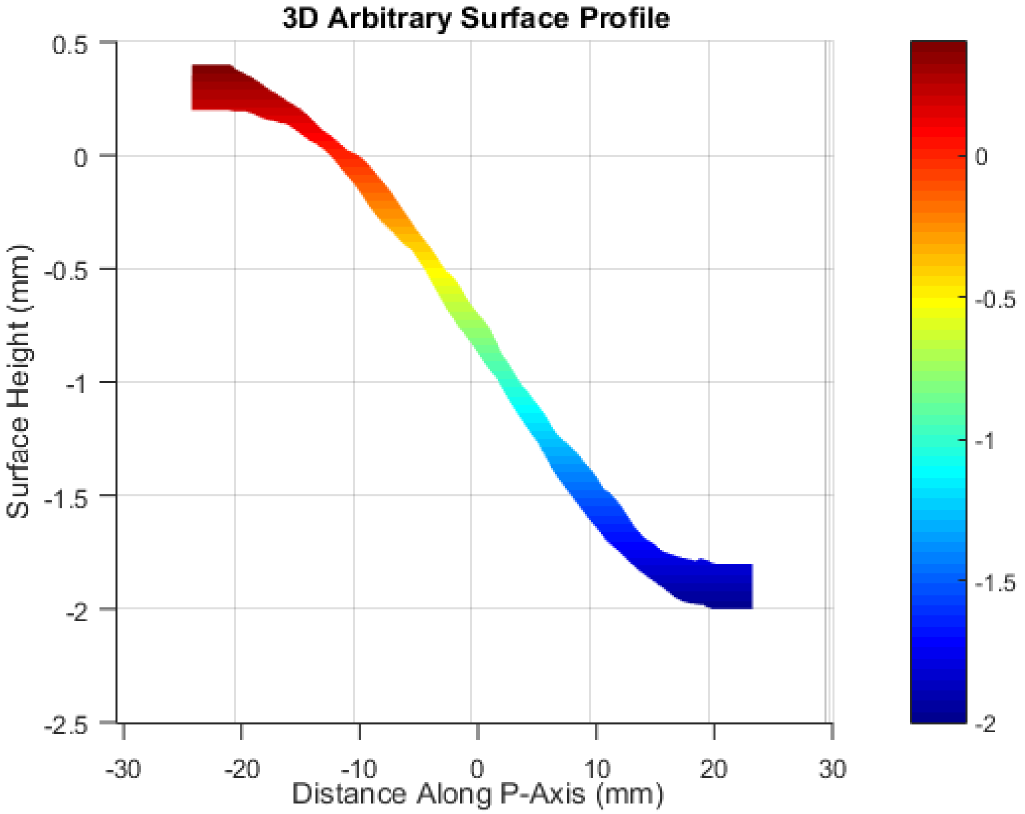

FIGURE 4.22: Side view of the 3D surface extracted shown in Figure 4.21.

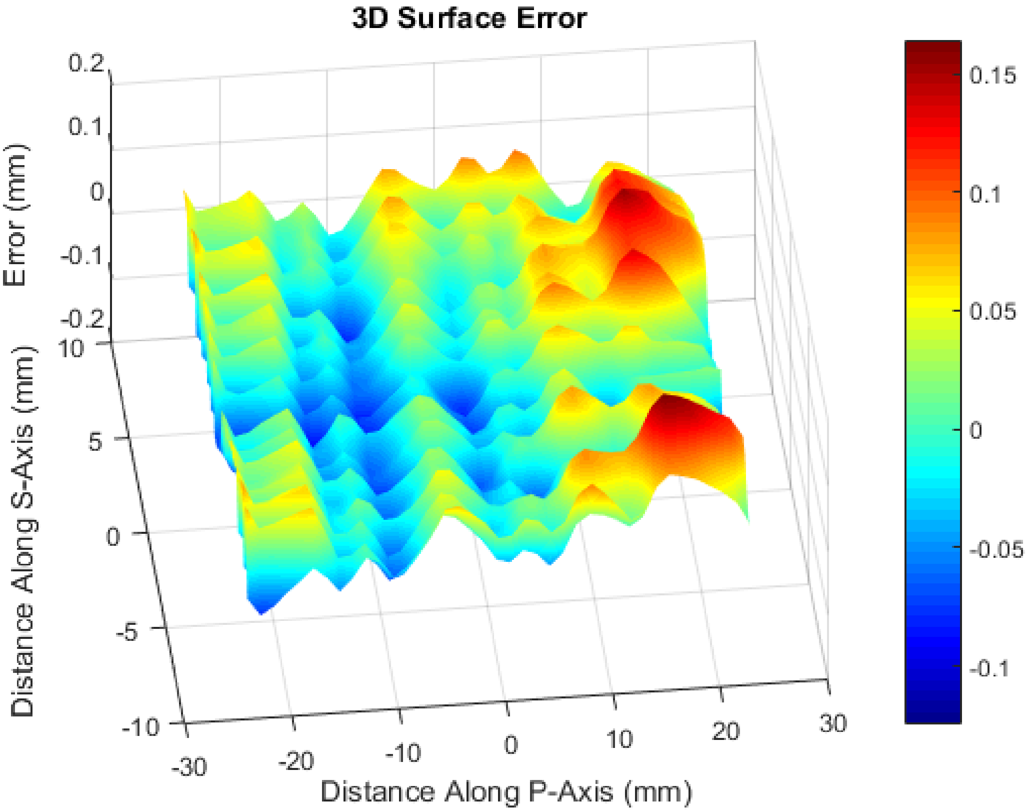

FIGURE 4.23: Error between the extracted and true 3D surface using the component modelled in Figure 3.22. The scale is in mm.

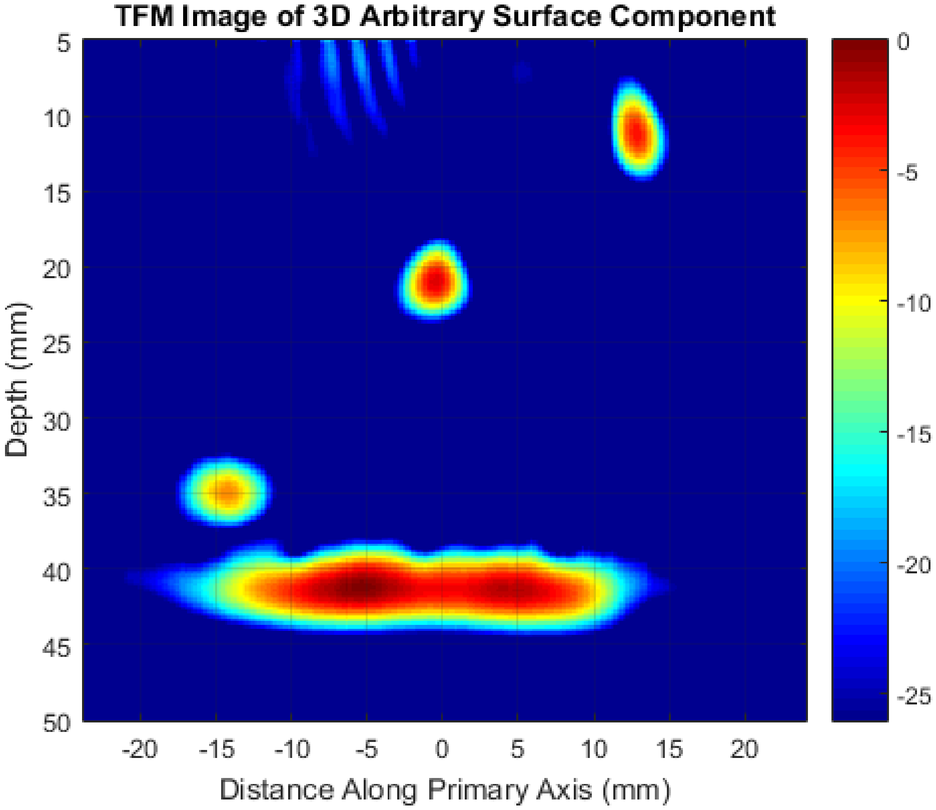

FIGURE 4.24: Corrected TFM image of the component in Figure 3.22 using the 3D extracted surface profile.

4.5 Discussion

An efficient method for detecting and subsequently reconstructing arbitrary surface profiles encountered in ultrasonic inspection has been demonstrated. This process fits naturally with the TFM method, where no additional user intervention is required for automatic correction of TFM due to complex components. A two pass TFM system is presented, where the surface TFM image uses a 10° pixel window to remove interference. The surface profile is then extracted using a mid-point method for pixels above a threshold specified as -14dB. A routine referred to as the surface approximation is then used to reconstruct the surface profile for the extent of the inspection, such that it can be relayed to automatically correct the TFM image of the component. The method has been demonstrated successfully, with high accuracy, across a range of surface profiles typical of those encountered in ultrasonic inspection in the nuclear industry. This surface detection method does not require additional instrumentation, neither does it add significantly to the processing time of conventional TFM. Using FMC data and TFM to detect and subsequently relay the surface profile removes the necessity for additional profilometry scans to be performed, instead allowing a single dataset to be collected for any single position.

The surface profiles considered in this work are limited to those encountered on the primary pipework of nuclear plant. Such components exhibit a smooth profile that may undulate due to grinding and polishing, further investigation would be required for surfaces taking other forms, especially those with sharp edges or rough surfaces.

The benefit of using 2D arrays for inspection of complex components is that the surface can be fully mapped over a 2D area, this would not be possible with a linear array, perhaps resulting in errors in the surface and therefore ToF calculations and TFM imaging.

Chapter 5

Design of a Sparse 2D Array for Complex Components

The probe plays an vital role in ultrasonic inspection performance, affecting the time and cost, as well as quality of data recorded. Sparse 2D arrays have been demonstrated to offer comparable imaging performance over an inspection volume with a smaller number of elements, compared with conventional fully-populated matrix arrays [76]. Their design and performance are investigated here in order to realise an efficient, high-quality, minimal cost inspection system. A concept probe design is established, with consideration of the inspection requirements and array design parameters discussed in Chapter 1. Initially a 1.5MHz concept probe was manufactured and evaluated as a prototype array, suited to inspections in the scope of work in this Thesis. A review of this probe then lead to a final design, of a 2MHz sparse 2D array. The performance of both the prototype and revised array was evaluated by analysis of their respective characterisation checks. Furthermore, their performance when inspecting regions A, B and C on the bespoke test block, illustrated in Figure 4.1 in Chapter 4, is presented.

5.1 Design Specification

No specific set of rules exist for ultrasonic inspection design, instead it often involves various compromises in both the probe and inspection specification to meet the desired requirements. It is therefore important to understand the intention of the inspection before establishing a probe and inspection design. This includes prior knowledge of any expected flaws to be detected, and their approximate size and orientation. Additionally, it is essential to appreciate the physical limitations of the inspection with respect to the component material properties.

Summarising the component, as detailed in Chapter 1, the main factors to consider are that it is thick section (40 - 100mm), coarse grain stainless steel. This restricts the inspection frequency to low ultrasonic frequencies for NDE of 1-2MHz. For the purpose of comparing probe performance, 3mm SDH are used since they are known reflectors and representative of the size of defects to be detected in the context of this EngD. Also, the probe's ability to image the surface, for profile reconstruction was considered.

TFM has already been demonstrated successfully for inspection of the bespoke test block, using a 1MHz 2D matrix array, as in Chapters 4. It continues to be the chosen imaging method here. Initially a zero degree inspection is considered, where the probe face is parallel to the flat BW of the test block. A water gap of 35mm is used throughout in order to separate repeat interface signals from the BW of the component.

Inspection performance is highly dependent on the probe used, and often there is a trade-off between parameters is required for optimisation. The main factors to consider are the element configuration and complete aperture size, element size, shape and pitch, the number of elements and operating frequency.

5.1.1 Element Layout

Ultrasonic arrays offer a number of advantages for NDE, as introduced in Chapter 2. Linear arrays are increasingly replacing conventional probe inspections, however the uptake of 2D arrays in industry has been much slower. One main drawback of 2D arrays is the vast number of elements required to achieve similar imaging performance to a linear array, over an inspection volume. Currently, phased array controllers accommodate 128 to 256 channels in general, which is in line with linear arrays routinely consisting of up to 128 elements. As an example, considering a 2MHz linear array with 16 elements and a pitch of 1.4mm, and a length of 10mm, the equivalent 2D matrix array would require 112 elements over the same aperture. This is because steering in either the primary or secondary axis requires the probe to meet the $\lambda/2$ criteria in order to avoid spatial aliasing [77]. Figure 5.1 shows that a substantial increase in the number of elements is required to achieve a 2D array equivalent to a linear array.

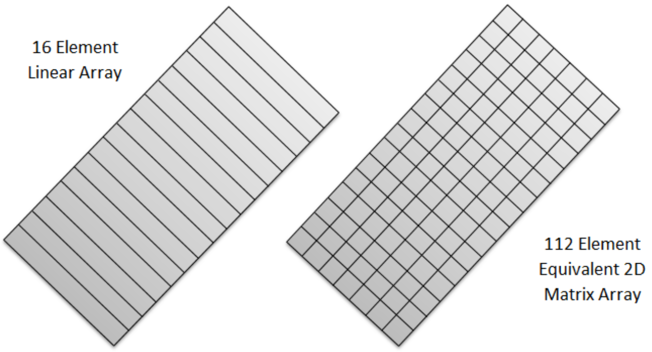

FIGURE 5.1: 16 element linear array, and 112 element 2D matrix array with the same overall aperture, obeying $\lambda/2$ criteria.

One way to overcome this negative aspect is to use an eccentric element layout, where instead of creating a fully populated matrix, the elements are arranged randomly. Various studies have considered reducing the number of elements in 2D arrays, either by removing elements from a periodic grid or creating an aperiodic structure. One major drawback of sparse arrays is the large amplitude of side lobes, that arise in beam steering. This is not so problematic in this study, as angled inspection is not considered, however it is important to acknowledge. Several aperiodic element configurations have demonstrated suitable imaging performance, comparable that of a fully populated matrix array, with a smaller number of elements or larger aperture.

Various alternatives to 2D matrix arrays have been sought in the form of fully random distributions or distinctive layouts. Fully random layouts are difficult to control since there is no specification or restriction on the distribution of the elements. This can result in regions of many elements close together, or very far apart. A number of studies have therefore considered controlled aperiodic array configurations by employing conformal mapping theory or geometric designs such as spirals [8, 78]. Such layouts allow for greater spacing between elements compared with matrix arrays while avoiding periodicity. It is therefore possible to achieve inspection performance comparable to fully populated arrays only with a reduced number of elements, and thus less data volume. This includes beamforming and post-processing abilities.

One successful method for aperiodic element distribution is the Poisson disk [79]. This can be thought of as a dart throwing system, where the darts relate to the elements. There is then a minimum spacing criteria that ensures no two elements are too close. Figure 5.2 illustrates the Poisson disk layout, with elements in black and their satellites in orange, indicating the minimum separation between neighbouring elements.

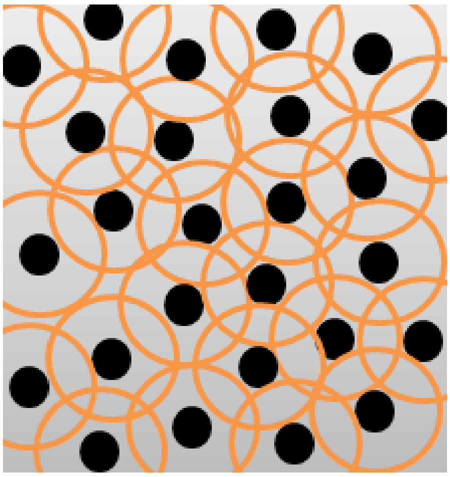

FIGURE 5.2: Example of Poisson disk distribution, where elements (black) are placed at random, but cannot be closer than the minimum spacing (orange).

This system provides a layout similar to a matrix array, but removes the periodicity while allowing a greater area to be covered by a set number of elements. Various studies document the ability of ultrasonic probes exhibiting a Poisson disk element distribution. The Poisson disk distribution is therefore the chosen element layout for both the prototype, and revised sparse 2D arrays in this work.

5.1.2 Frequency and Aperture

The frequency, number of elements and complete aperture size are all related parameters, and dictate how an array performs overall. As stated previously, the components considered in this work require ultrasonic frequencies, in the range of 1-2MHz. Such frequencies are still able to propagate a reasonable range in a highly attenuative medium, while providing suitable resolution. Current inspections of the components considered in this work employ conventional probes in the range of 2MHz, verifying this range of frequencies is appropriate.

In conventional phased arrays, the complete aperture of the array determines the Near Zone (Nz) of the ultrasonic field. The relationship between aperture and Nz is given in Equation 2.16 in Chapter 2. The same principle is applied in TFM, since the full array is used in data collection. As the algorithm is synthetically focusing everywhere in the image, it is desirable to have the Nz beyond the imaging range. An aperture in the range of 40-50mm is therefore sought, to achieve a Nz in the range of 100-150mm in steel.

Finally, the number of elements in the array also impacts on the efficiency of the inspection. As too many elements results in a large volume of data, and too few elements would result in poor coverage. A total number of elements in the range of 64-128 for an aperture of around 50mm was deemed appropriate. This was based on the 1MHz matrix array, with 128 elements over an aperture of 60mm by 40mm. Trials proved that when randomly removing elements from the array, the imaging performance did not significantly deteriorate until half of the elements were removed. Figure 5.3 illustrates the impact removing elements from the array has on the imaging performance. Three TFM images are shown where 90, 70 and 40% of the 128 elements were used respectively. The image maintains its integrity until removal of approximately 50% of the elements, where the SNR becomes poor and the image becomes blurred.

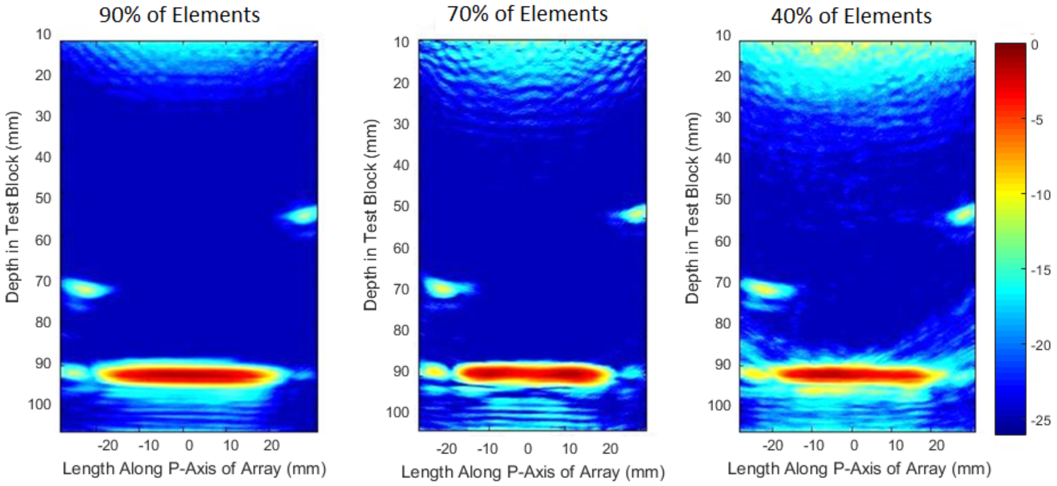

Figure 5.3: TFM images created using 90, 70 and 40% of the 1MHz matrix array. Image quality is maintained until around 50% of the elements are removed.

The aim in this study is to improve the inspection performance, through increased sensitivity and resolution, while remaining efficient. This means that although the overall objective is to reduce the number of elements, a compromise is required due to the increase in frequency. The exact number of elements in the array is specified by the complete aperture and element pitch.

5.1.3 Element Pitch

The element size, shape and pitch all contribute towards the formation of the ultrasonic field. In both conventional linear arrays and 2D matrix arrays, the pitch of elements must be smaller than half of the wavelength for typical inspection techniques. This is to avoid grating lobes that have an adverse affect on the ultrasonic field. In conventional arrays, the pitch usually dictates the element size, as illustrated in Figure 2.13 in Chapter 2. The array is typically structured with rectangular or square elements, separated by a small gap.

Sparse arrays offer more freedom over the element size, shape and pitch. Referring to the Poisson disk layout, the pitch relates to the minimum distance separating any two elements. Since this configuration is aperiodic, it permits spacing between elements greater than $\lambda/2$ while still avoiding grating lobes. The pitch must be large enough to avoid cross coupling between adjacent elements, while remaining small enough to provide good coverage. For the probe being designed here, separations in the range of 0.2mm and 1mm were deemed appropriate. Separations in this range would ensure adjacent elements were adequately isolated from one another while avoiding undulations in the sensitivity due to elements being too far apart. Relatively large elements, in the order of 2-3mm dependent on frequency, were considered due to their increased sensitivity compared with smaller elements.

Similar to the effect of the full array aperture, element shape and size influence the behaviour of ultrasonic field. Since sparse arrays are not specified by a grid, they offer alternative control over the element shape. Circular elements are preferred here, since they produce a symmetrical ultrasonic beam as shown in Figure 5.4. This compliments equal imaging resolution in both the primary and secondary axes, as opposed to square or rectangular elements which produce slightly elongated or oval beams. Circular elements also fit most intuitively with the Poisson distribution.

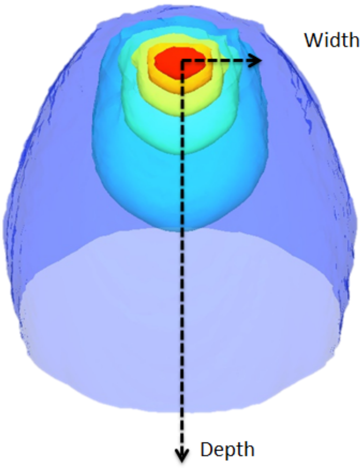

FIGURE 5.4: Example of a symmetrical ultrasonic beam profile from a circular element.

5.1.4 Summary of Design Constraints

The parameters discussed so far have identified a number of design constraints which can be summarised, and further investigation can be made within this criterion to settle on a sparse 2D array design.

The design constraints of a sparse 2D array suitable for inspection of complex components in the context of this study are therefore:

- an operating frequency of 1-2MHz
- an overall aperture of around 50mm in diameter or similar
- no more than 128 elements, and preferably less
- circular shaped elements in a Poisson disk distribution
- an element separation between 0.2mm and 1mm
- element diameter of 1-4mm

5.2 Prototype Array

A prototype sparse 2D array was designed within the parameters defined above, manufactured, and then evaluated for inspection of the bespoke test block. A centre frequency of 1.5MHz was chosen, to slightly improve the resolution of the inspection, while avoiding a significant reduction in SNR. The aim of the prototype array was to achieve imaging performance similar to that realised by the 1MHz matrix probe used so far, with a secondary aim of reducing the number of elements.

A circular aperture of 50mm was selected, to provide large volumetric coverage, similar to that of the 1MHz array. The frequency and aperture size were considered fixed for the remainder of the prototype probe design.

The *beam* and *inspection* modelling packages in CIVA (CEA de France) were used to simulate the performance of a variety of array configurations. First, the element size was considered and a compromise between a large surface area for sensitivity, without narrowing the beam spread was sought through evaluating element diameters between 1mm and 4mm. The *beam* tool was used to simulate the ultrasonic field generated by a single element operating at 1.5MHz in steel with a 35mm water gap. The result is shown in Figure 5.5 for diameters between 1 and 4mm at 1mm increments. As expected, the beam narrows with increasing diameter and otherwise the beam profiles remain unchanged. An element diameter of 3mm was chosen for the prototype array due to the relatively wide beamspread coupled with a large surface area for high sensitivity.

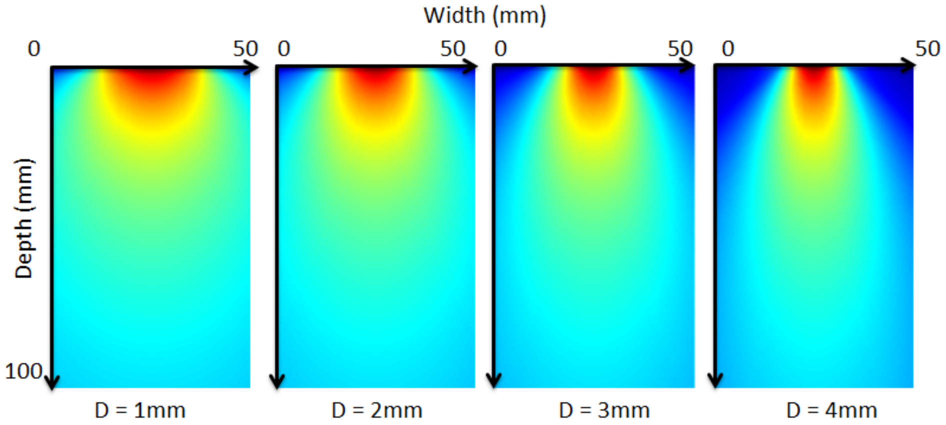

FIGURE 5.5: Ultrasonic beam profile for element diameters (D) between 1mm and 4mm.

The *inspection* tool was used to generate FMC data for the probe configurations noted in Table 5.1. A screen capture of this model in CIVA is shown in Figure 5.6. The model is based on the surface profile at position A and has three 3mm SDH placed at depths of 20mm, 58mm and 78mm.

As detailed in Table 5.1, the probe design was changed iteratively, increasing the minimum spacing from 0.2mm to 1mm in 0.1mm increments. The aperture was fixed at 50mm as specified above, and the element diameter was fixed at 3mm. The number of elements in the array decreased with increased spacing, as appropriate. Evaluation of each configuration was performed by using the auto correction TFM algorithm on each FMC data set, and the quality of the probe was determined by it's ability to reconstruct the surface and detect the SDHs.

Spacing (mm)	0.2	0.3	0.4	0.5	0.6	0.7	0.8	0.9	1.0
No. El	85	79	76	73	71	69	64	60	56

TABLE 5.1: Probe configurations modelled for 1.5MHz prototype array, defining the spacing and number of elements.

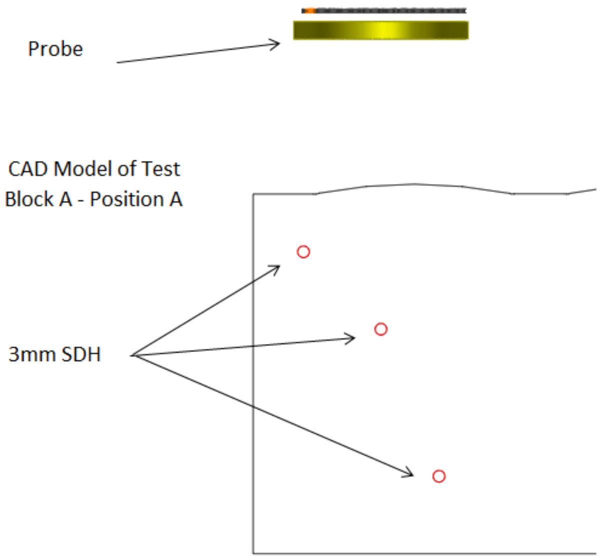

FIGURE 5.6: 2D representation of the 3D FMC simulation model in CIVA, using the surface profile of position A . Three 3mm SDH are placed at 20mm, 58mm and 78mm to evaluate each array designs ability to image efficiently.

This model presents ideal operating conditions that are not expected in practice, however it provides an indication of the performance that may be realised in the inspection. The TFM image obtained using an element separation of 0.8mm is shown in Figure 5.7. The TFM image obtained for the various separations did not deviate from this example image. The SNR for each of the 3 SDHs remained within $\pm 2dB$ despite the change in the minimum spacing. Table 5.2 details the SNR for each of the SDH for the range of element spacings.

This very slight variation in SNR suggests the image quality of the component is not significantly affected by the diverse minimum spacings considered here. Furthermore, the probe's ability to reconstruct the surface profile was considered, as the minimum spacing was increased. Table 5.3 details the RMS and maximum errors between the detected surface profile and true surface profile for all element spacings considered. Additionally, the extent of the surface detected is also noted, and is generally in the range of 45mm which is coincident with the complete aperture of the probe at 50mm. RMS errors in the order of 0.10mm were observed for arrangements with minimum separations between 0.2mm and 0.5mm, while separations in the range of 0.6mm to 1mm produced RMS errors of 0.20mm.

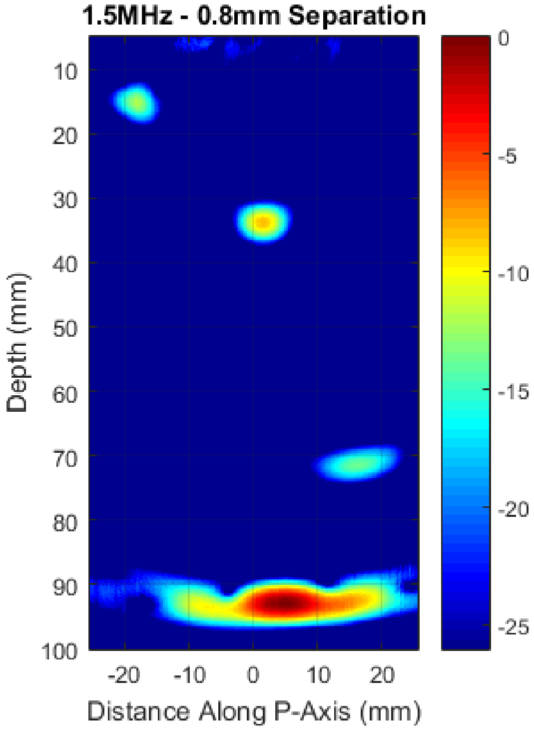

FIGURE 5.7: TFM image created using 1.5MHz sparse 2D array with an element separation of 0.8mm.

Spacing(mm)	SDH1 SNR(dB)	SDH2 SNR(dB)	SDH3 SNR(dB)
0.2	-	18	12
0.3	16	18	13
0.4	16	18	14
0.5	18	18	14
0.6	16	18	12
0.7	16	18	14
0.8	14	18	12
0.9	16	18	14
1.0	16	18	12

TABLE 5.2: SNR of SDH for varying spacings of the 1.5MHz prototype array.

Spacing (mm)	**RMS Error (mm)**	**Max Error (mm)**	**Extent(mm)**
0.2	0.11	0.29	35
0.3	0.09	0.21	40
0.4	0.09	0.18	38
0.5	0.10	0.23	40
0.6	0.21	0.53	45
0.7	0.12	0.26	45
0.8	0.19	0.29	45
0.9	0.20	0.44	50
1.0	0.20	0.60	45

Table 5.3: Analysis of surface profile detection using various element separations for the 1.5MHz sparse probe design.

Evaluation of each of the factors considered conclude that separations up to 0.8mm, using the Poisson disk distribution for elements of 3mm, do not significantly reduce the inspection quality. This coincides with a complete circular aperture of 50mm in diameter, accommodating 64 elements utilising this layout. The final design for the prototype array is therefore 64 elements in a Poisson disk distribution, with a minimum separation of 0.8mm and 3mm element diameter, over a complete circular aperture of 50mm.

5.2.1 Manufacture

The prototype array was manufactured in CUE, meaning specification of all of the constituent parts of the probe was required. Spot checks on the device's performance were completed at various stages in the manufacturing process, to ensure the integrity of the device at each step. Key parts of the process include design of the active layer, and subsequently dicing and filling to the required specification, establishing the electrode pattern, electrical wiring, applying the matching and backing layers and securing the device in suitable housing. A schematic of the various components that constitute an ultrasonic probe is shown in Figure 5.8. The main components include the active layer, backing and matching layers, internal and external wiring and the probe housing. The active layer contains the piezoelectric material and electrode pattern of the array on the back face, and ground electrode on the front face. Thin internal wires are connected to each electrode representing an element, which are then attached to a more robust external cable with a Hypertronics connector. The backing layer is applied to damp any signals generated at the rear face of the active layer, and avoid unwanted reverberations within the probe housing. The matching layer acts as a link between the active layer and load medium, enhancing energy transfer and acting as a protective layer.

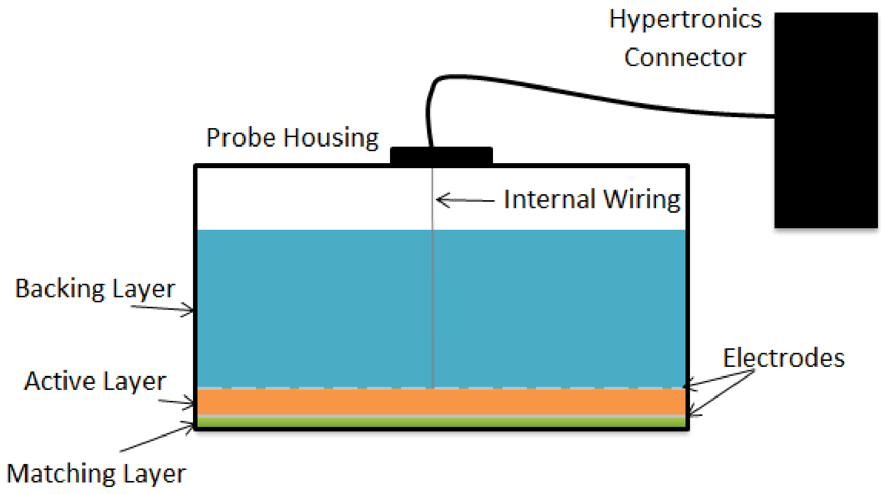

FIGURE 5.8: Constituent components that form an ultrasonic probe, showing the active, matching and backing layer, probe housing and electrical wiring.

First, specification of the active layer of the probe was conceived using a simulation package developed in CUE, known as *compD*. This is built upon physical properties, experience and expertise of ultrasonic array manufacture in CUE. The active layer is comprised of piezoelectic ceramic and polymer filler, which are collectively referred to as a piezocomposite [80]. Numerous studies have concentrated on developing advanced ultrasonic arrays through various piezocomposite structures or manufacturing techniques [20]. The probe design here relies on established device fabrication methods, piezocomposite structures, matching and backing layers. It is not in the scope of this work to develop or implement any new design or method in probe manufacture. The piezocomposite was chosen to be PZT5H ceramic, together with an epoxy resin, RX771C/NC mixed with Aradur HY1300 hardener, as the filler. A saw width of 0.1mm, saw pitch of 0.34mm and a volume fraction of 0.5 was specified through *CompD*, resulting in pillars of 0.24mm, with a thickness of 0.95μm, giving an aspect ratio of 0.25 for the piezocomposite.

The procedure is demonstrated in Figure 5.9, starting with a slab of PZT5H ceramic of the desired dimensions. The thickness of the ceramic should be slightly larger than the final desired thickness of the device, as specified by the frequency. The saw is passed through the ceramic at the specified pitch, creating channels in the ceramic and leaving vertical strips. The saw depth should be set to the final thickness, leaving a ledge to support the pillars, as in part 2 in Figure 5.9. The saw then passes in the direction perpendicular to the first pass, resulting in rectangular pillars. Finally the channels are filled with the passive material which is typically an epoxy material. In some cases, the passive material is applied between steps 3 and 4 to prevent the ceramic pillars from being damaged during the second manufacturing stage. The ledge is then sliced off, leaving only the ceramic held together by the epoxy, which results in a two-phase material of piezoceramic pillars embedded within a polymer matrix.

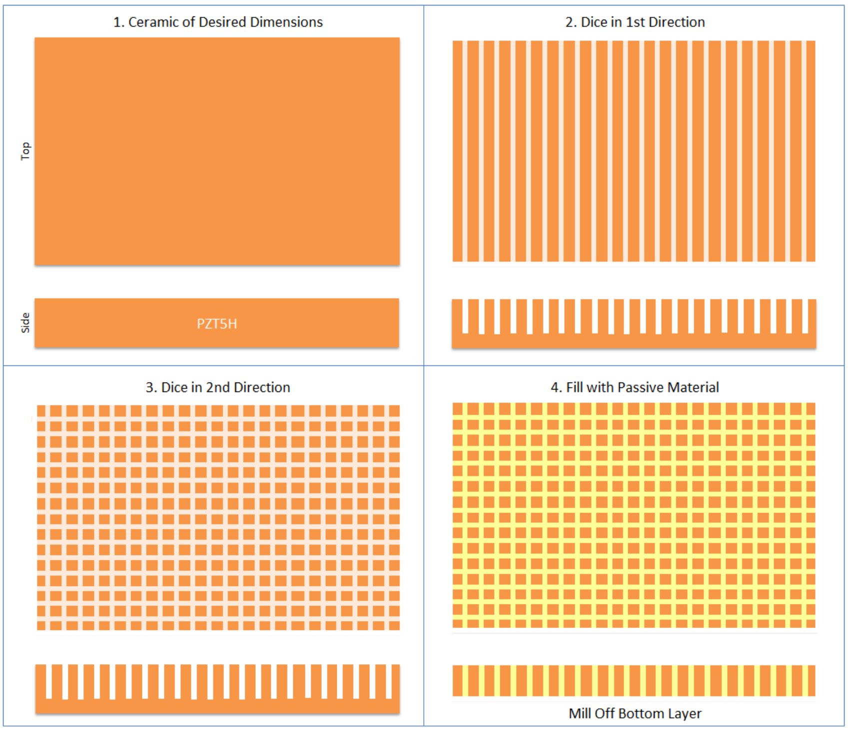

FIGURE 5.9: Steps involved in dicing and filling a piezocomposite device, starting with a block of ceramic, dicing in either direction and filling the channels with a passive epoxy.

The piezocomposite was evaluated using laser vibrometry at this stage, to ensure it operated uniformly over the full aperture. This involves applying a voltage through a signal generator to the piezocomposite, and using a laser to measure the magnitude and phase of displacement on the surface of the device. This confirmed the piezocomposite was operating in a uniform manner, with the phase and magnitude of the oscillation consistent over the complete aperture. The electrical impedance of the piezocomposite was evaluated as a single device, with the result shown in Figure 5.10. As expected, there is a single smooth peak representing the phase, indicating the device is oscillating uniformly. There is also a stable curve depicting the magnitude, with a clear minimum and maximum. The minimum represents the resonant frequency of the device, which appears at 1.5MHz as expected. Ideally electrical impedance checks should be performed at intervals in the array fabrication process, however this was not possible due to the fragile wires attached to the probe and dominance of the coaxial cable. Instead the presence of a phase was sought for each element throughout various stages of manufacture, to ensure a connection was made. A phase response was detected for 63 out of 64 elements in the array during manufacture, with a consistent output obtained for all elements.

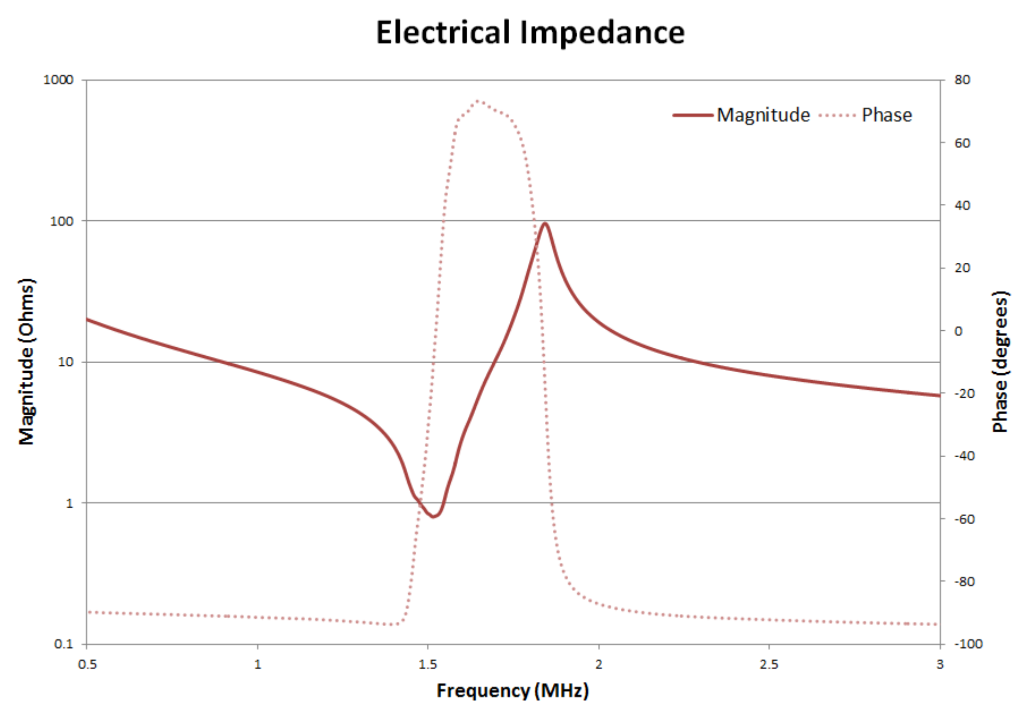

FIGURE 5.10: The magnitude and phase response of the electrical impedance of the 1.5MHz piezocomposite.

A stencil representing the element layout was then created, and is shown in Figure 5.11. The stencil was secured onto one side of the piezocomposite before a 10nm layer of Chromium was applied and then a 500nm thick layer of silver was evaporated onto the surface. This produced the electrode pattern on the array, where electrical connection could be made. The four corners of the composite were also coated, representing ground connections. The opposite face of the composite was also coated with a layer of silver, acting as ground. A photograph of the piezocomposite with the electrode pattern is shown in Figure 5.12. It is noted here that the pillars on the piezocomposite are square and the electrodes representing the elements are circular. This creates a circle with pixelated edges, however since the pillars are very small compared to the elements, there are no significant effects to the overall device performance.

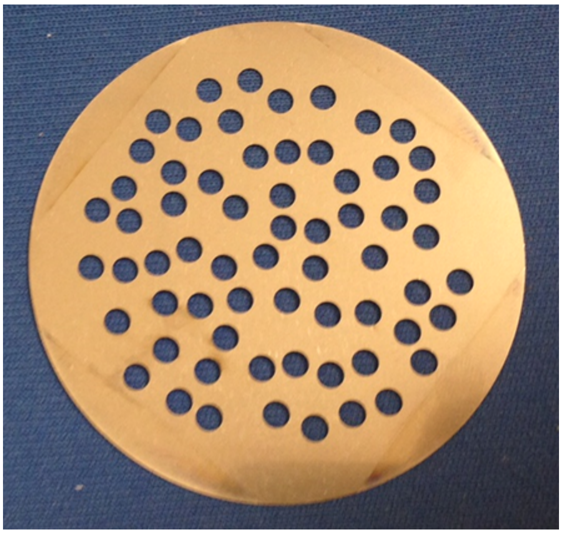

Figure 5.11: The stencil used to identify the element layout (50mm diameter), when evaporating the electrode pattern with silver paint.

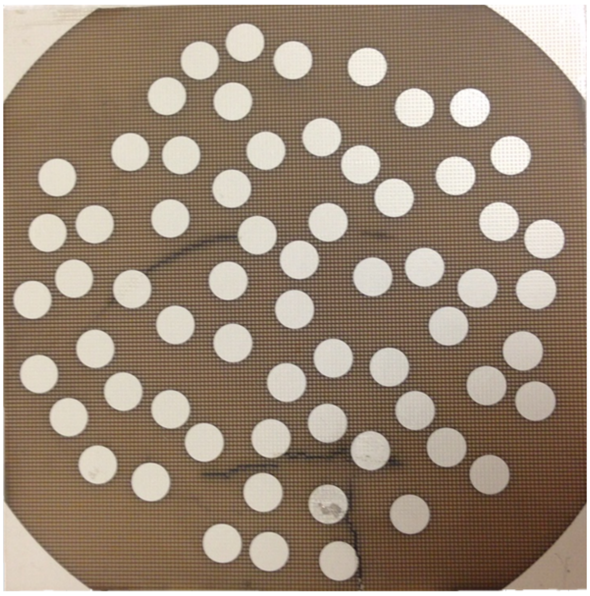

FIGURE 5.12: The piezocomposite with the electrode pattern in silver. The pillars of the piezocomposite are visible in the background.

The backing and matching layers used for this device were derived from successful devices, previously manufactured in CUE. The backing material used was a soft set epoxy using Araldite CY208 resin mixed with Aradur HY956 hardener and filled with 12% tungsten. This composition was designed to match the 16MRayl impedance of the piezocomposite. A final backing layer thickness of 35mm was used. A dual matching layer was used, with a 73% alumina filled hard set epoxy using RX771C/NC resin mixed with Aradur HY1300 hardener closest to the piezocomposite, then a layer of only the epoxy with no filler. A quarter wavelength thickness for each of the matching layers was used, resulting in $485\mu m$ and $414\mu m$ respectively. This arrangement is an established system used in CUE for a device operating into water, as is the case here.

Thin electrical wire was then hand soldered onto each pad on the piezocomposite, as shown in Figure 5.13. It was then secured into the probe housing, and a thin backing layer was applied to avoid pulling any of the wires off. A coaxial cable with a Hypertronics connector is required to connect to a phased array controller, so connection between the thin wires and the individual coaxial wires is required. Four small Printed Circuit Boards (PCBs) each consisting of 32 pads, split into 16 pairs of two, were used to provided a bridge from the fragile wires connected to the piezocomposite and the coaxial wires. Ground electrodes were connected to the inside of the probe housing.

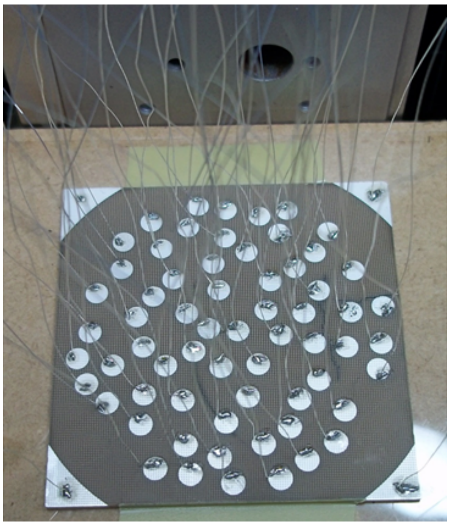

Figure 5.13: Small thin electrical wires, hand soldered to the electrode pattern on the piezocomposite.

The remainder of the backing layer was poured into the probe housing. It is best to apply the backing layer in stages to avoid the tungsten settling near the piezocomposite, which can result in a short circuit within the device. Finally, the two matching layers were applied in turn, using a flat blade to achieve a uniform thickness of each layer over the area of the piezocomposite. The final device, in the housing with the Hypertronics cable attached, is shown in Figure 5.14.

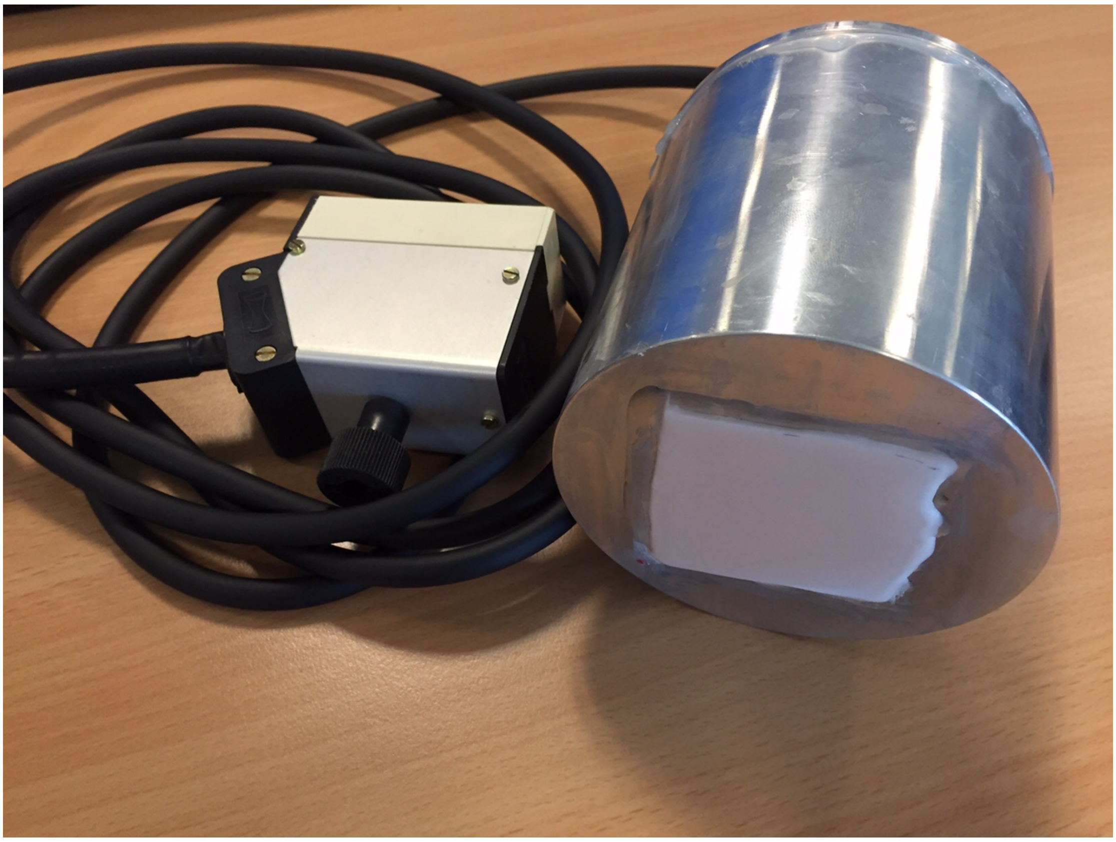

Figure 5.14: Photograph of the prototype array in the probe housing with a Hypertronics cable attached.

5.2.2 Characterisation

Upon completion of an ultrasonic array, the manufacturer must ensure the device's characteristics are within quality guidelines. Generally the characterisation of an array includes it's sensitivity, bandwidth, centre frequency and pulse length. Each of these have an impact on how well the probe will perform in an inspection scenario, so it is imperative to identify and characterise the arrays performance.

Initally, laser vibrometry was performed by connecting an electrical signal to a single pin relating to an element on the array in turn. The full aperture of the array was then scanned by the laser to ensure only the selected element was vibrating. This process confirmed that 63 out of the 64 elements in the array were operating as expected. It is believed that the remaining element was touching the probe casing and is therefore effectively connected to ground.

The array was suspended 20mm in water above a glass block to perform the characterisation. The following graphs present the results, initially the typical A-Scan from 6 elements, selected at random, is shown in Figure 5.15. The frequency response from the six elements is then given in Figure 5.16. These time and frequency response samples are indicative of the complete set of 63 elements in the array. It is clear from these results that the response from the array is consistent over the range of elements, with the time response signals in phase and the frequency responses uniform.

The variation across all elements in the array is shown for the sensitivity and central frequency, in Figures 5.17 and 5.18 respectively. The deviation of the sensitivity was 2.5dB from the mean, with a maximum deviation of 5dB observed. A mean centre frequency of 1.4MHz was determined for the array, with a mean fractional bandwidth of 60%.

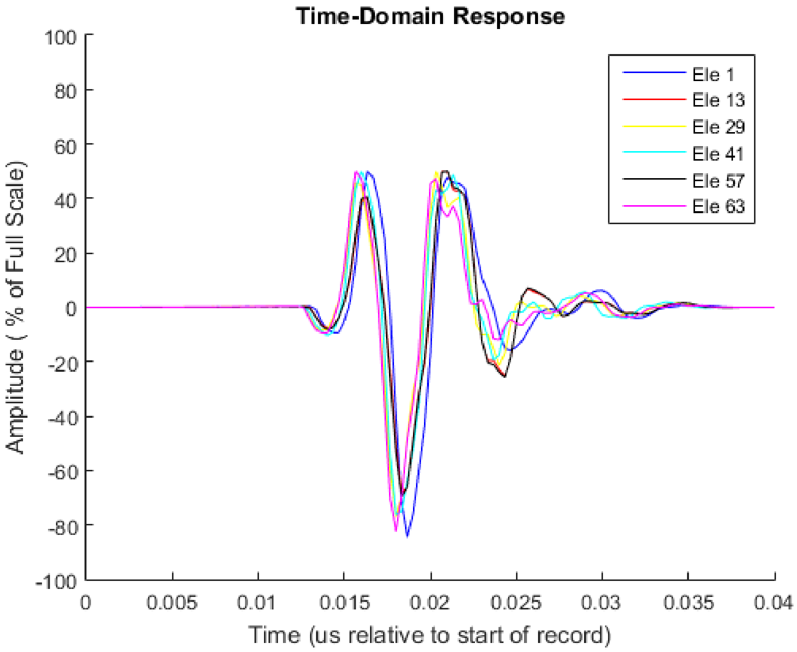

FIGURE 5.15: Typical time domain response from a glass block, sampled from 6 elements in the array. The signals are consistent and are of good form.

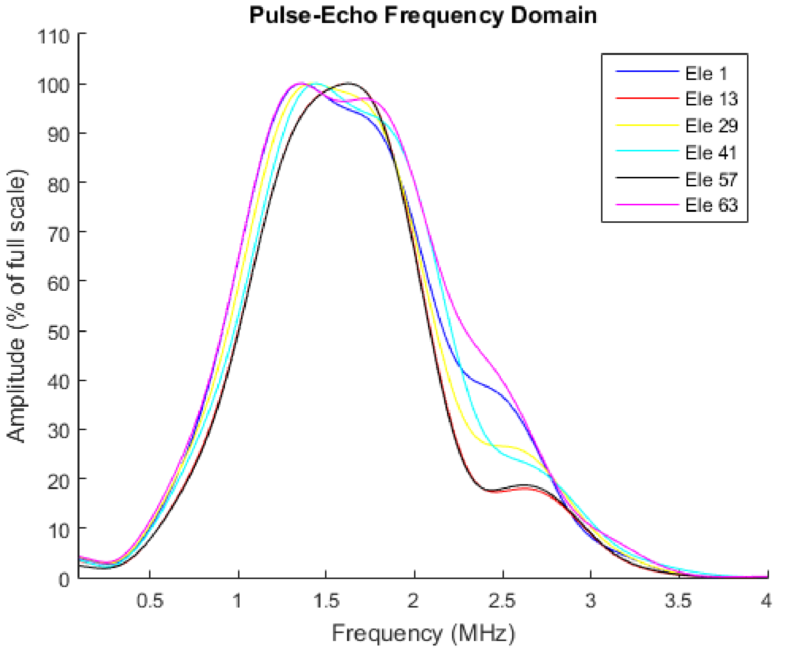

FIGURE 5.16: The frequency response from 6 elements in the array, one main peak is observed at around the expected centre frequency, of 1.5MHz.

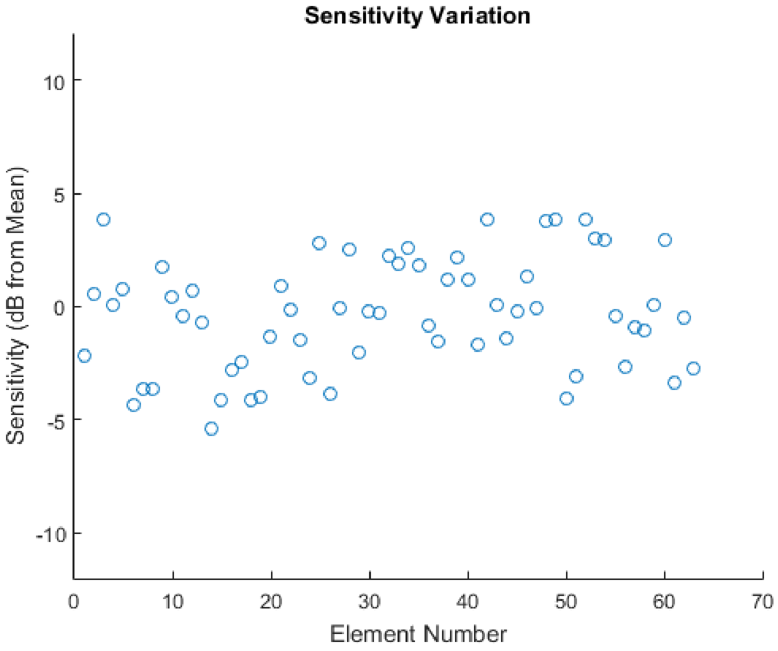

FIGURE 5.17: The variation of sensitivity across all elements in the array, measured with respect to the mean sensitivity. A standard deviation of 2.5dB was observed, with a maximum of 5dB.

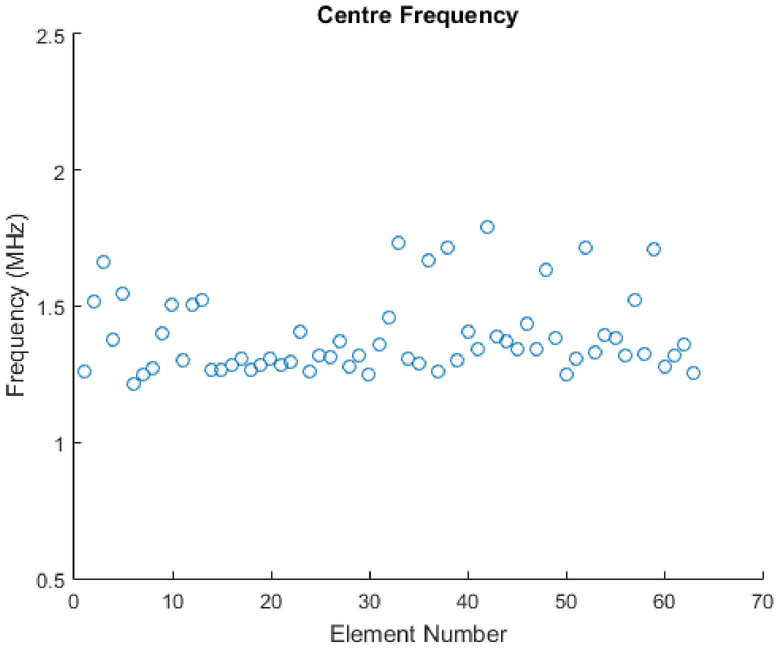

FIGURE 5.18: The centre frequency measured for each element in the array, with a mean centre frequency of 1.4MHz, minimum of 1.25MHz and maximum of 1.8MHz.

5.2.3 Inspection Performance

The prototype array was evaluated for it's fitness for purpose using positions A, B and C on the bespoke test block. Both the ability to accurately reconstruct the surface profile, and adequately image the SDH were considered. The probe was suspended in water, 35mm above the test block at each of the positions, and data was recorded at a sampling rate of 25MHz. The settings specified in Chapter 4, for the surface TFM and extraction method are maintained here. Figure 5.19 shows the surface corresponding to positions A, B and C respectively with the raw profile points extracted and subsequent surface fit compared with the true profile. Unfortunately, the surface is not represented well at position A, as the profile extends incorrectly to the right, instead of following the true surface. Positions B and C are relatively well represented, although the trough in position B is slightly underestimated.

The surface TFM settings, including the window and extraction threshold, were adjusted to investigate whether a better surface representation could be achieved. Although slight differences in the profile were observed, no significant improvement was accomplished using this data. A summary of the RMS and maximum error in the surface profile measurement, at each position, is given in Table 5.4. The errors are notably larger than achieved with the 1MHz matrix array. Table 5.5 also details the error between the raw extracted profile points and the surface fit using the approximation method. The importance of accurate extraction is demonstrated here, since a good surface representation cannot be achieved if it is not extracted first.

Error	**Position A (mm)**	**Position B (mm)**	**Position C (mm)**
RMS	0.70	0.22	0.17
Max	1.79	0.50	0.34

Table 5.4: RMS error between the true surface and measured profile at positions A, B and C, using the prototype 1.5MHz sparse array.

Error	**Position A (mm)**	**Position B (mm)**	**Position C (mm)**
RMS	0.23	0.19	0.23
Max	0.43	0.54	0.35

Table 5.5: RMS error between the raw extracted surface and the surface fit using the approximation method at positions A, B and C, using the prototype 1.5MHz sparse array.

Despite a reduction in surface profile accuracy, the TFM images still represent the component reasonably well, as shown in Figure 5.20. The BW at position A, B and C is located at the correct depth, with good SNR (26dB). The SDH are also detected in the correct locations, however their SNR is slightly reduced when compared with the 1MHz results.

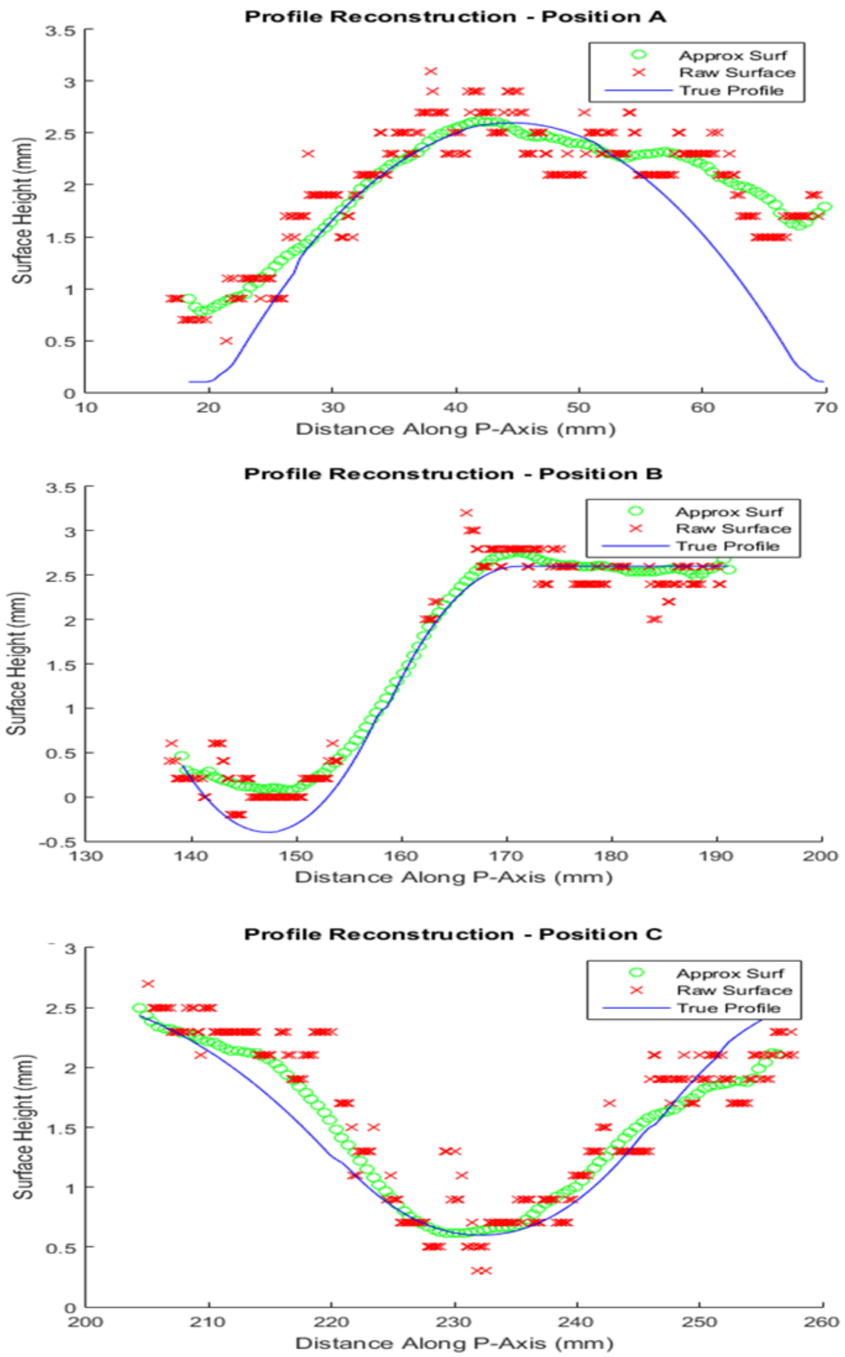

FIGURE 5.19: The surface representation obtained from the 1.5MHz prototype array(green), at positions A, B and C. The true surface profile is shown in blue and raw extracted points are in red.

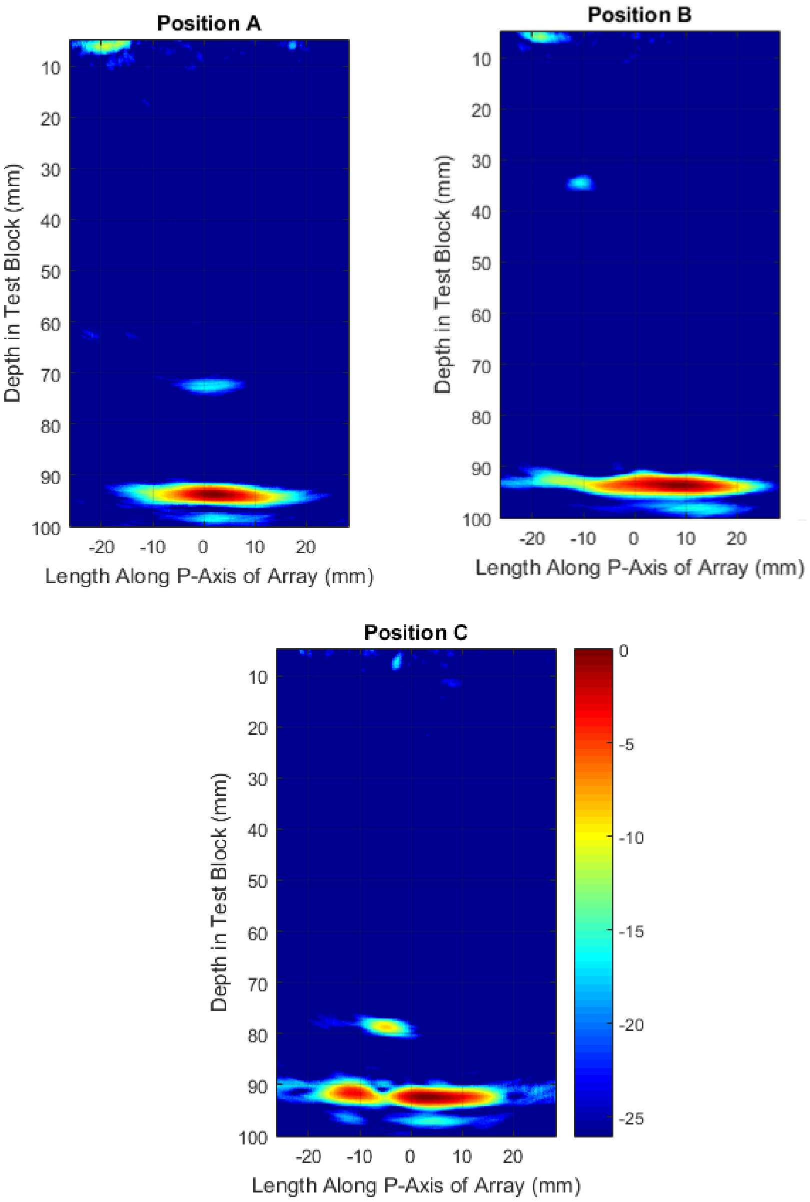

FIGURE 5.20: The corrected TFM images at position A, B and C obtained using the 1.5MHz sparse prototype array. Using the respective surface profiles shown in Figure 5.19.

5.3 Revised Array

Review of the performance of the 1.5MHz prototype array, provided some lessons and changes for a final probe design. Since a high SNR achieved with the 1.5MHz array, the decision was made to slightly increase in operating frequency again, to 2MHz. This is in line with the frequency currently used to inspect such components in industry. The increase in frequency means a slightly smaller element size than in the prototype array, with 2mm chosen as a suitable compromise between sensitivity and divergence. In order to achieve a similar volumetric coverage as the prototype array, the number of elements was increased to 128, which is still reasonable in terms of the amount of data.

One key issue observed in the prototype array was that the distribution of energy was not uniform due to the sparse layout. In a matrix array the elements are positioned at regular intervals, however with the Poisson disk distribution elements have no fixed distance between them. This means that some elements may have 2 or 3 in the vicinity of the minimum separation, and other elements may have no neighbours close to that distance. Care was therefore taken in the element distribution by ensuring the elements were packed as tightly as possible, while still obeying the minimum spacing.

Similar to the prototype array, an iterative process was followed using the CIVA model to determine the number of elements, array size and minimum separation. The final design included a rectangular aperture of 45mm by 30mm, an element diameter of 2mm and a minimum spacing of 0.8mm, with a total of 128 elements. This layout is shown in Figure 5.21.

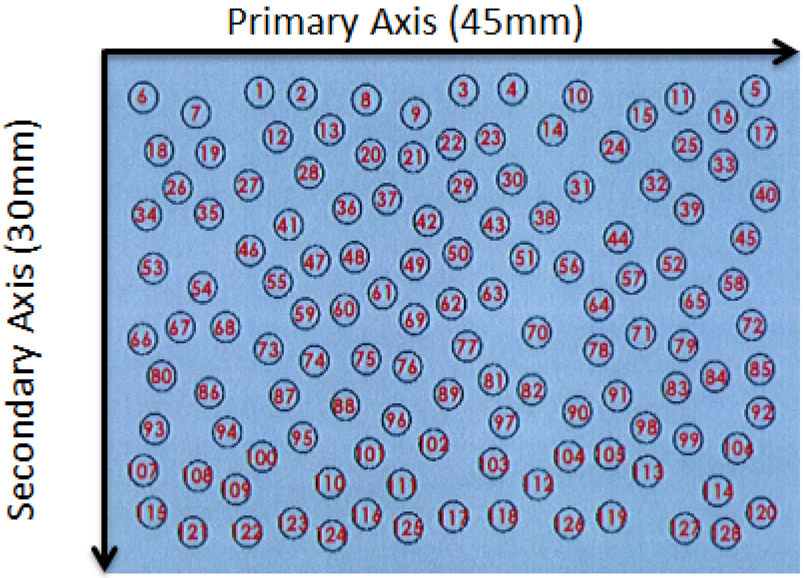

FIGURE 5.21: Element layout of the 2MHz revised sparse array design.

The revised design was then specified to array manufacturer Sonaxis for fabrication. Due to competition in the array manufacture market, the internal structure of the probe, including the pizeocomposite, backing and matching layers are unknown.

5.3.1 Characterisation

As noted previously, array manufacturers are typically required to document the performance of the device upon delivery. Sonaxis provided documentation for the 2MHz sparse array, advising it had passed all quality checks and was operating as expected. The characterisation process was repeated, and is detailed here for clarity. As with the prototype array, the probe was suspended in water, 20mm above a glass block. The time and frequency domain response are shown in Figure 5.22 and 5.23, for 8 elements chosen at random. Both figures show the 8 elements are operating consistently, with a centre frequency of 2MHz. A bandwidth of 60 % was reported by the manufacturer, and confirmed by the characterisation performed here.

The sensitivity and frequency deviation over the complete set of elements are then shown in Figures 5.24 and 5.25 respectively. All 128 elements in the array were confirmed to be operational. The standard deviation in the sensitivity was measured to be 0.8dB here, while the mean operating frequency was found to be 1.9MHz. A minimum frequency of 1.6MHz, and maximum of 2.1MHz were observed. The fractional bandwidth over all elements in the array was averaged to 60%, which is in agreement with the manufacturers result. The sensitivity and frequency characterisation reported by the manufacturer were slightly improved compared with the result here. They reported a deviation in the sensitivity of 0.3dB and a mean centre frequency as 2.03MHz, with a minimum of 1.98MHz and a maximum of 2.01MHz, giving a standard deviation of 0.01MHz. Although the results obtained here vary slightly with the manufacturers results, it is a relatively small difference and signify the probe is of high quality.

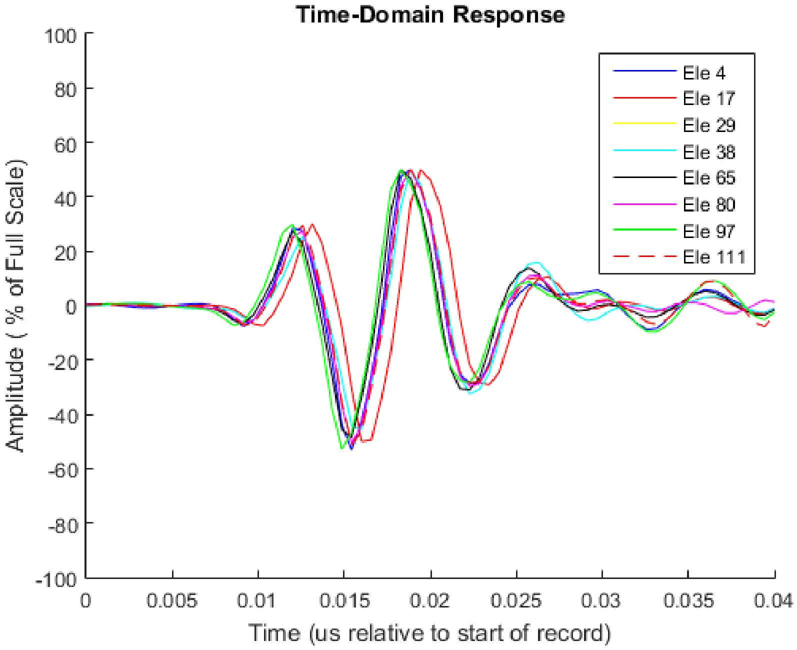

FIGURE 5.22: Typical time domain response from the 2MHz sparse array on a glass block, sampled from 8 elements in the array. The signals are consistent and are of good form.

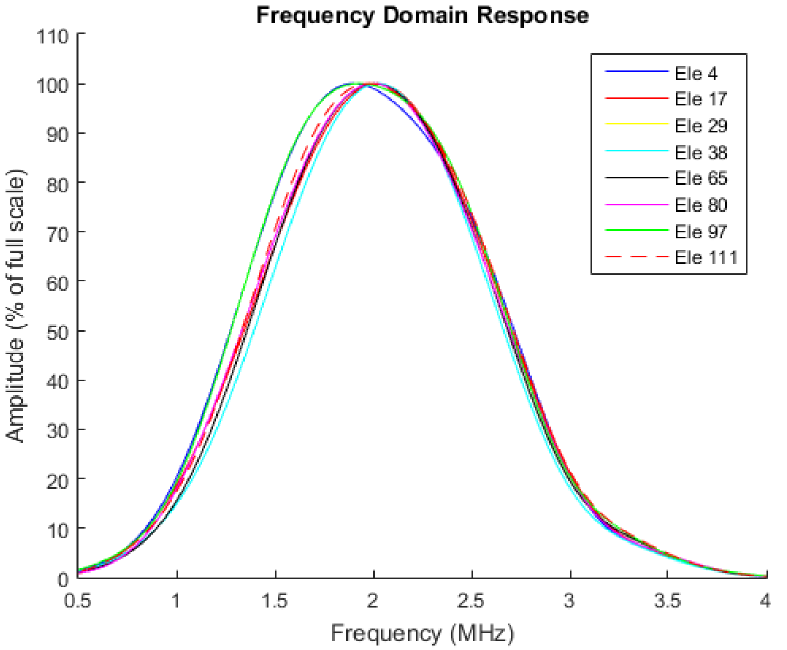

FIGURE 5.23: The frequency response from 8 elements in the 2MHz sparse array, one smooth peak is observed at the expected centre frequency, of 2MHz.

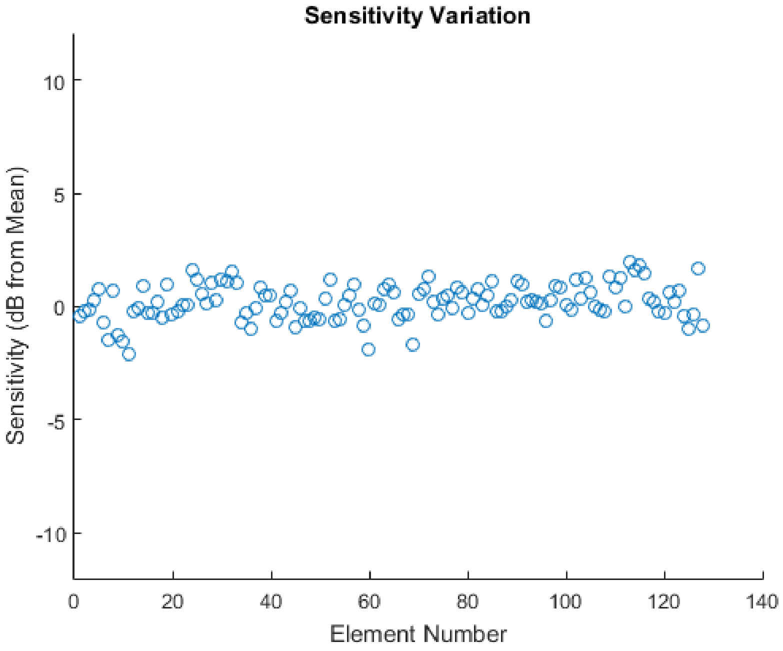

FIGURE 5.24: The variation of sensitivity across all elements in the 2MHz sparse array, measured with respect to the mean sensitivity. A standard deviation of 0.8dB was observed, with a maximum of 1.8dB.

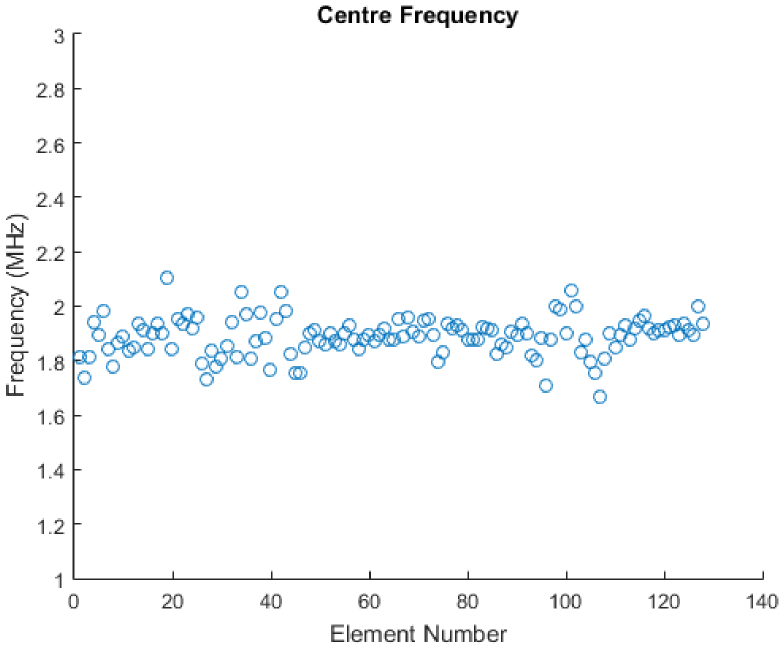

FIGURE 5.25: The centre frequency measured for each element in the 2MHz sparse array, with a mean centre frequency of 1.9MHz, minimum of 1.6MHz and maximum of 2.1MHz.

5.3.2 Inspection Performance

The 2MHz sparse 2D array was then used to interrogate positions A, B and C, to evaluate its performance for this inspection. As with the prototype array, the probes ability to accurately reconstruct the surface profile, as well as detect the SDH and BW with reasonable signal quality was considered. FMC data was collected using the MP5 and a sampling frequency of 25MHz. The probe was suspended 35mm above the test block, in water, and data was recorded at position A, B and C respectively. The previously defined surface extraction parameters were maintained for continuity here. Figure 5.26 shows the reconstructed surface profile in green, compared with the true surface profile in blue, at positions A, B and C. The surface is accurately represented in all 3 cases, and a summary of the RMS and maximum errors observed between the extracted and true profiles are given in Table 5.6.

Error	**Position A (mm)**	**Position B (mm)**	**Position C (mm)**
RMS	0.07	0.12	0.05
Max	0.15	0.19	0.16

Table 5.6: RMS error between the true surface profile and measured profile at positions A, B and C, using the revised 2MHz sparse array.

The TFM images accounting for the arbitrary surface profiles shown in Figure 5.26, are shown in Figure 5.27 for position A, B and C. The BW is positioned correctly for all 3 positions, with a strong SNR of 26dB. The SDH appearing in each of the positions are also located correctly with reasonably high SNR, in the range of 16 to 26dB. In line with the improvement in surface detection, the TFM images are considerably better than those achieved with the 1.5MHz prototype array. The increase in operating frequency and revised element distribution also play a role in this improvement.

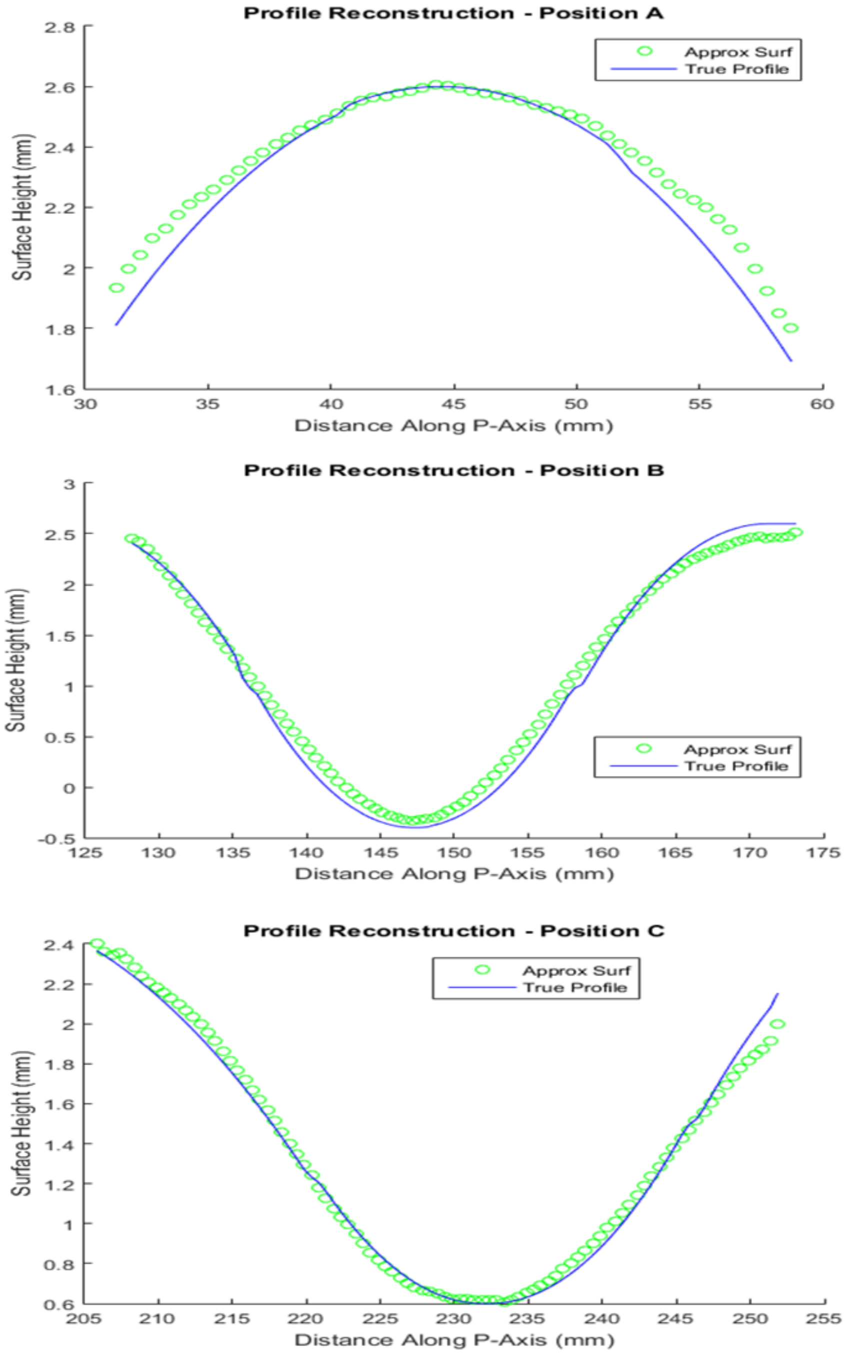

Figure 5.26: The surface representation obtained from the 1.5MHz prototype array(green), at positions A, B and C. The true surface profile is shown in blue.

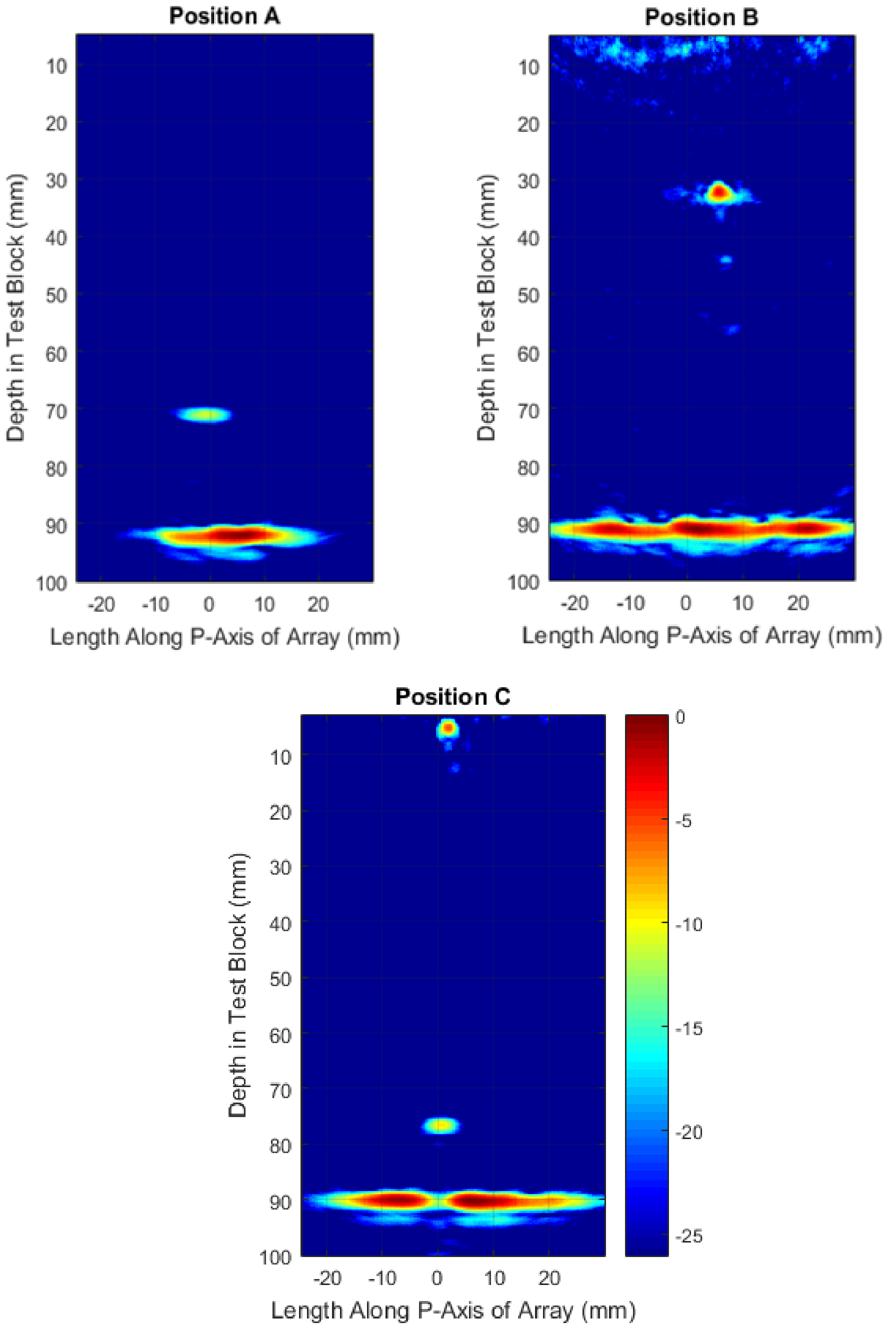

FIGURE 5.27: The corrected TFM images at position A, B and C obtained using the 1.5MHz sparse prototype array. Using the respective surface profiles shown in Figure 5.19.

These results conclude that the revised 2MHz sparse array is suitable for the inspections considered in this work. This probe is therefore employed for the final inspection system developed in the remainder of this Thesis.

5.4 Discussion

Sparse 2D arrays offer a solution to volumetric ultrasonic imaging, by reducing the number of elements required compared to a fully populated matrix array. They have been investigated in this Chapter in order to achieve an efficient inspection system, while maintaining or improving on the quality compared with the 1MHz array. A higher frequency was sought to improve resolution, in line with industrial inspections performed with conventional 2MHz probes. A prototype array was designed, manufactured and evaluated, allowing for a revised probe to be designed and manufactured externally.

The prototype array was designed based on a centre frequency of 1.5MHz, with 64 elements over an aperture of 50mm. The Poisson disk distribution was employed with a minimum separation of 0.8mm and elements of 3mm in diameter. Ultrasonic characterisation of the prototype array concluded that 63 out of the 64 elements were operational, with a standard deviation in sensitivity of 2.8dB a bandwidth of 60% and mean centre frequency of 1.4MHz. This device did not perform as well as the 1MHz matrix probe when imaging the calibration test block, meaning a revised design was required. Poor representation of the surface profile was obtained using this probe resulting in poor TFM imaging of the SDH in the component. The element distribution is the most likely contributor to this poor performance, due to lack of control over elements with nearest neighbours in the range of the minimum spacing. This resulted in an element distribution more densely packed in some regions compared to others. A revised element layout and higher frequency was sought to improve the performance.

The frequency was increased to 2MHz for the final probe design, over a rectangular aperture of 45mm by 30mm. The Poisson disk configuration was employed again, however care was taken to obtain a tightly packed layout. This avoids elements with no neighbours close to the minimum spacing and provides more uniform coverage in the inspection. A minimum separation of 0.8mm was maintained, with elements of 2mm diameter elements. The revised probe performed well when inspecting three reference positions on the calibration test block. The probe accurately reconstructed the surface profile and imaged the component at these positions, confirming its aptness for inspections in this work. The enhanced performance is mainly due to an improved element distribution and increase in frequency.

Chapter 6

Evaluation of a TFM Inspection for Complex Components

Each of the aspects studied so far must be combined to form a complete inspection system. This includes using TFM and dynamic surface detection for imaging using the 2MHz sparse 2D array. Automation of the technique is also considered in a move towards industrialisation of an inspection technique suited to complex components. Furthermore, a methodology for analysing the sensitivity in such inspections is formulated, which is vital for industrial application of TFM in UT. A practical method for coupling the probe to an arbitrary surface component is also discussed. Finally, the technique is evaluated for its ability to detect angled slots machined into the bespoke test block.

6.1 Inspection Automation

The data acquisition process, probe and imaging algorithms are required in order to form a complete inspection system for complex components. Each of these factors have been specified in earlier Chapters and they must now be combined with other features in a move towards forming an inspection procedure. One main interest is automation of the inspection, and subsequent image stitching between probe positions. Other considerations are centred around the industrial robustness of the inspection, including coupling of the probe, the approximate time of the inspection and size of data recorded. Additionally, the repeatability and reliability of the inspection process are important.

Automation of ultrasonic inspections is key to minimising exposure of personnel to hazardous environments. This is in line with the As Low As Reasonably Practicable (ALARP) principle [81], which stipulates that personnel should be out of range of any hazard unless it is unavoidable. This principle is especially important in the nuclear industry in order to avoid unnecessary exposure to harmful radiation. For this reason automated inspections are favoured on nuclear plant, and in this context ALARP means spending as little time as possible close to the radiation source. An automated inspection is typically achieved by attaching the ultrasonic probe to a manipulator that manoeuvres the probe over the inspection region on a component. This means that personnel can set up the inspection equipment at the point of inspection before moving to a safe place to monitor the inspection and perform data analysis. Cameras are often used so that the operator can check the inspection is progressing as expected, especially ensuring the probe is moving correctly and no cables are catching. Automation also aids the repeatability of an inspection, since known reference points and scan patterns are used instead of manually placing the probe on the component. This makes it easier to compare inspection performance from one outage to the next.

Conventional UT inspections have been performed using 2 or 3 axis manipulators to manoeuvre various probes round the component. Similar manipulators are suitable for use for this inspection, however there is an additional requirement for the manipulator to wait until all the required FMC data has been acquired before moving the probe to the next data acquisition position. With conventional UT the speed of the manipulator could be set to suit the rate of data being acquired, but in the case of FMC acquisition a stop-start approach is required. This is achieved by communication between the PAC and motor controller. The PAC informs the motor controller to wait until all of the required data has been captured before moving on to the next position. This action has been achieved using the Micropulse 5 (Peak NDT) and an Integrated Motor Control System (IMCS). This control is supported through the application Arraygen (Peak NDT), and negates the requirement for an encoder card on the computer since the IMCS is controlled directly through the Micropulse. An example of this process is illustrated in Figure 6.1, where the probe is attached to a 2 axis manipulator over the component. The inspection settings are specified using a laptop which is connected to the Micropulse, typically by an Ethernet cable. The Micropulse informs the IMCS where to move the scanner to, and waits for feedback from the probe before informing of the next position. The data is then relayed to the laptop through the Micropulse. This forms a continuous loop which enables automatic inspection.

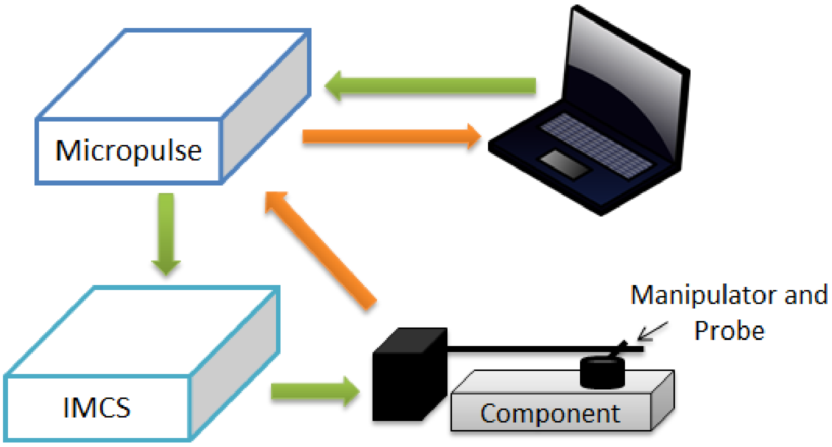

FIGURE 6.1: Micropulse-IMCS feedback loop used to enable automatic inspection using a manipulator.

A 2 axis scanner was deemed appropriate for use in this inspection. At this stage the inspection is performed in an immersion tank, and consideration for local coupling is made later in this Chapter.

As a general rule for conventional UT the probe is moved in increments equal to half of its length in that direction. This approach was followed to inspect the bespoke test block, HMC data was collected instead of FMC due to the reduced data size without sacrificing the data quality as discussed in Chapter 2. This process results in TFM images that overlap by half, meaning a way for stitching or fusing the images together is required. Various image stitching techniques exist such as taking the minimum, maximum or average as well as the requirement for the pixel to be approximately equal in both images [82, 83]. Each of the methods consider the pixel amplitude in two or more images and the resulting pixel is either the minimum, maximum or average of the two amplitudes. More complex algorithms may make further decisions on the final amplitude based on the difference between the pixel amplitudes and their surrounding pixels. Alignment of adjacent TFM images is not considered here due to the way the TFM images are created, resulting in a consistent inspection zone.

As a reminder, the TFM images in this study are based on a negative dB scale where 0dB is the maximum and -26dB is the minimum. In UT it is important to never dismiss a high amplitude signal, instead care must be taken to assess why the signal arises. A simple maximum value image stitching method is used here. Figure 6.2 shows two TFM images obtained by collecting HMC data separated by 18mm in the direction of the primary axis. Both TFM images present a strong horizontal signal at around 90mm, representing the BW and a smaller indication at a depth of 70mm, representing a SDH. Using the known separation as the offset bewtween the images along the primary axis, the two TFM images are stitched using the simple maximum method. The result is shown in Figure 6.3, where an uninterrupted BW is observed at 90mm and one SDH is visible at 70mm.

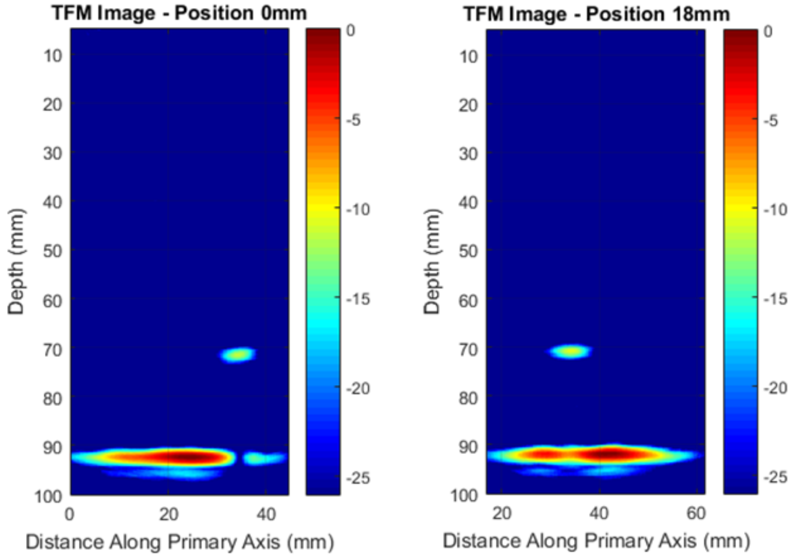

FIGURE 6.2: TFM images obtained with a separation of 18mm, with the BW and a SDH visible in both images.

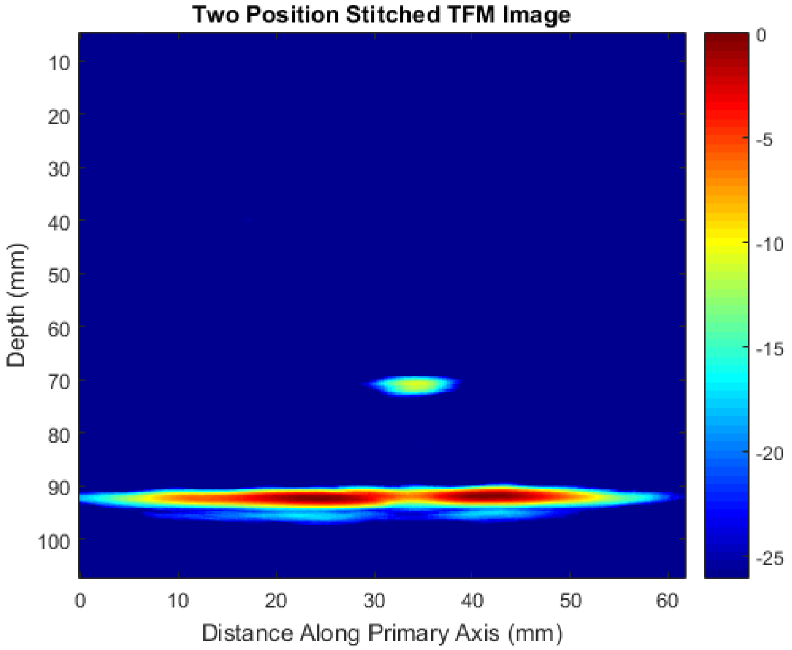

FIGURE 6.3: Combined image of the two TFM images separated by 18mm in Figure 6.2

Data was collected at 20mm intervals along the full length of the test block using the 2MHz sparse array in immersion. The complete surface profile detected is shown in Figure 6.4 and the component is reconstructed in Figure 6.5. These images demonstrate the technique is suitable for automation using this combination of controlled manipulation of the probe and simple image stitching. The response from the BW is reasonably consistent along the full length of the test block, with a slight break in the middle due to surface conditions. The SNR for each of the six SDH are detailed in Table 6.1. The maximum SNR here is 26dB with reference to the BW which returns the highest amplitude. Each of the SDH produce a SNR in the region of 14 - 21 dB, which is between 5 and 11dB less than the BW.

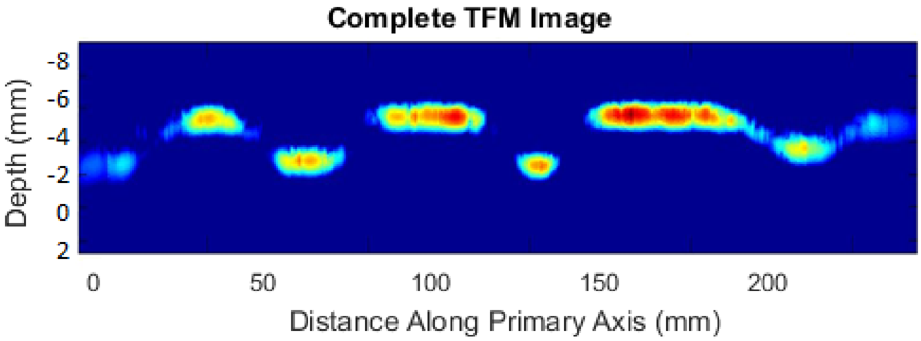

FIGURE 6.4: TFM image of the complete surface of the irregular form test block.

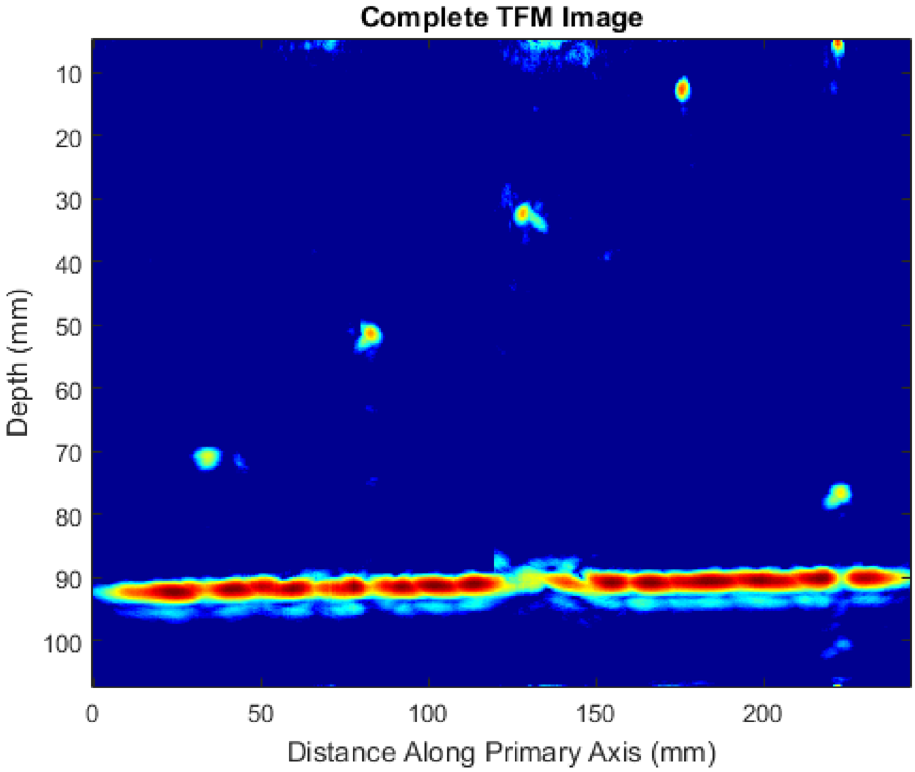

FIGURE 6.5: TFM image of the complete test block, showing 6 SDH and the BW.

SDH ID	**Depth (mm)**	**SNR (dB)**
1	71	14
2	51	19
3	32	19
4	12	21
5	5	21
6	77	18

TABLE 6.1: SDH depth and amplitude recorded on Test Block 1 using the 2MHz sparse array.

The data was collected using the Micropulse 5PA in combination with the IMCS and a 2 axis scanner. Making use of the stop-start routine HMC was returned once every 0.8s using the 2MHz sparse array with 128 elements. A single y-z slice TFM image using this HMC data is produced in approximately 2 seconds. Although this is not quite considered to be real-time imaging, it is close to it and nonetheless a quick turnaround given the complexity of the inspection scenario. Individual HMC files for this setup can be expected to be in the range of 15-20MB. This means the data storage requirements for a single inspection would be significant and must be considered in moving this inspection into industry.

As mentioned in Chapter 3, SDH are typically used as calibration reflectors to establish the sensitivity of an inspection. Real defects such as cracks are unlikely to have the geometry of SDH and are likely to return a smaller amplitude. It is expected that defects could still be easily detected with this technique due to the high amplitude response from the SDH. The SNR of the SDH vary slightly as a consequence of both the surface profile and depth of defect. Ideally, each of the SDH should return a similar amplitude meaning the effect of the surface profile and defect position on the SNR must be considered. The test block used in this work is representative of the worst case of surface expected to be inspected using UT, it is unlikely that component surfaces in-service will be as extreme as this meaning the inspection performance should not suffer as much as due to the surface form. However real defects may be more difficult to detect due to their orientation and further work is required to understand the variables that impact inspection performance and defect detection for in-service components.

6.2 Sensitivity Map

Defect detection and characterisation are highly dependent on the sensitivity of an inspection. It is therefore important to understand the sensitivity in an inspection volume, in order to correctly contextualise the response. As discussed in Chapter 2, conventional UT and phased array imaging utilises a DAC to achieve even and predictable sensitivity in an inspection. A DAC would be complex to employ in FMC due to the number of individual A-Scans being acquired. A methodology to evaluate the relative sensitivity for inspection of complex components using FMC and TFM is sought.

One issue that must be addressed here is accurately representing the interface and BW of the component on the A-Scan. Typically no signal should exceed 100% FSH to avoid saturation, and 80% is the ideal limit. When the interface is within these limits the BW of the steel is significantly less, up to around 10 % FSH. This is due to the acoustic impedance difference, causing a decrease in the energy reaching the BW compared with the interface.

Ideally the PAC should accommodate a dual gain setting, whereby the signal was amplified by some factor after the interface. This has not yet been implemented however is being considered for future work. It could be executed by automatically triggering a secondary gain which would be applied to each A-scan in the HMC data immediately after the interface. Currently this issue is overcome by setting a single gain that allows both the interface and BW of the component to be accurately defined without saturation. This often means using a high dynamic range, either 12 or 16 bit, to ensure all features in the component can be adequately distinguished.

Since TFM is a delay and sum algorithm the sensitivity can be predicted using a similar structure of calculations. The relative sensitivity in an inspection volume can be determined by calculating the approximate maximum amplitude of each transmit-receive pair at each pixel in the volume. The simplest scenario is used initially to demonstrate this approach, where the probe is in contact with the component.

First, the image space is segmented into a coarse grid to minimize the number of calculations required. For a single pixel and transmit-receive pair in the HMC, the angle between the transmitter position and pixel is calculated. Similarly, the angle between the pixel and receiver position is calculated. A simple beam spread model of the array elements is then used to assess the maximum possible amplitude that could reach the pixel for that transmit-receive pair. This process is repeated for all transmit-receive pairs for a single pixel, and then for all pixels in the coarse grid. Interpolation is then used to relate this sensitivity map to the resolution used to create the TFM image. Figure 6.6 illustrates this concept. Two pixels in the image space are highlighted in yellow. Considering the transmit-receive pair incident on the pixel to the left, the element is both transmitter and receiver and is almost directly above the pixel. This means the angle between the transmitter and the pixel will be close to zero, and the amplitude at that pixel will be at the maximum. The same is true for the receiving element here. Conversely, for the pixel on the right hand side there is an angle θ_{Tx} separating the transmitting element and the pixel. The receiving element is at a separate location and the angle between the pixel and receiving element is therefore θ_{Rx}. The angle between the transmitter or receiver and the pixel can then be used to assess the relative amplitude that could reach the pixel for that transmit-receive pair.

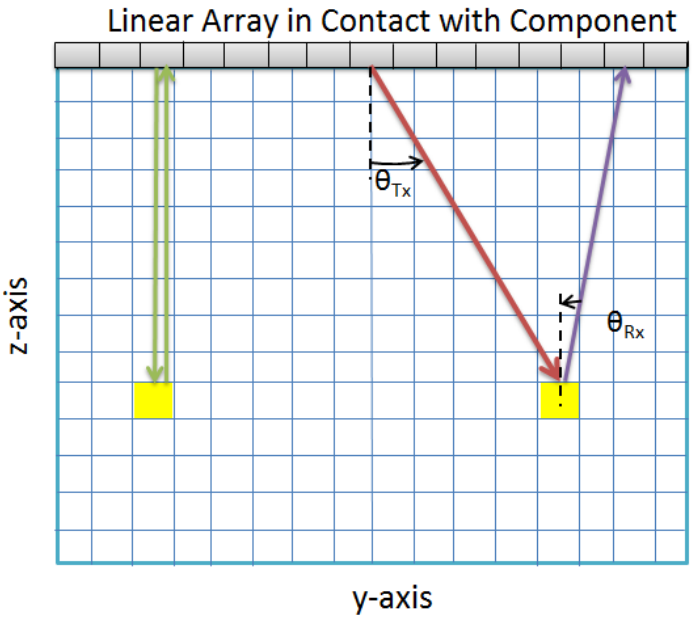

FIGURE 6.6: Schematic for calculating the angles of the transmit-receive path to a given pixel in a TFM image, required to calculate the relative sensitivity.

The relative amplitude of the ultrasonic beam can be predicted by replacing the variable k in Equation 2.17 as follows in Table 6.2 for circular elements. The relative amplitude is normalised, where 1 is the maximum amplitude and 0 is negligible amplitude. Assessing where θ_{Tx} and θ_{Rx} lie within the beam spread allows the maximum amplitude possible at any pixel, for any transmit-receive pair to be calculated.

Amplitude	1	0.94	0.90	0.84	0.80	0.75	0.71	0.67	0.63
k	0	0.21	0.30	0.37	0.42	0.47	0.51	0.55	0.59
Amplitude	0.60	0.56	0.50	0.45	0.40	0.35	0.32	0.25	0.1
k	0.62	0.65	0.70	0.75	0.80	0.83	0.87	0.93	1.09

TABLE 6.2: Relative amplitude and k values for circular elements.

Using the examples in Figure 6.6 as a case study, for the pixel on the left θ_{Tx} and θ_{Rx} are 0 since the pixel lies directly below the transmitting and receiving elements. This means the energy from that transmit element, and also the energy returning to the receive element is along the maximum path. However, for the pixel on the right hand side if angle θ_{Tx} is taken to be around 60° and θ_{Rx} is assumed to be around 30° then the pixel does not lie in the maximum path for either the transmit or receive ray. Rearranging Equation 2.17 for k gives:

$$k = \frac{D \sin \theta}{\lambda} \tag{6.1}$$

To calculate the value of k, and hence the relative amplitude, a 2mm element diameter is assumed to be operating at 2MHz in stainless steel of longitudinal velocity $5750ms^{-1}$, resulting in a wavelength of 2.9mm. Substituting these variables into Equation 6.1 gives k as 0.597 and 0.345 for θ_{Tx} and θ_{Rx} respectively. This corresponds to amplitudes of 0.63 and around 0.86 for θ_{Tx} and θ_{Rx}. These factors are then multiplied to obtain the maximum relative energy for the path between this transmitter, pixel and receiver. In this case the maximum energy would be 0.54.

After repeating this process for all Tx-Rx pairs in the FMC and all pixels in the TFM image, a sensitivity map can be formed to show the relative amplitude possible at each pixel due to FMC and TFM methodology. The map for this simple case, where a linear array is in contact with a component is shown in Figure 6.7. The sensitivity is normalised to the maximum in the image which occurs at the bottom centre of the image, corresponding to the centre of the array. A 32 element linear array with a pitch of 2mm and operating frequency of 2MHz in steel was specified for this coverage map, and the elements are indicated along the top of the image by red circles. This sensitivity map is as expected since the maximum energy will be centred around the middle of the array, where the angle between the maximum number of elements and pixels remains small. The relative sensitivity gradually decreases closer to the array, and is least at the edges. This is because the angle between most of the elements and the pixels will be large, meaning little energy from the element will reach those areas. This means that a defect appearing at either top edge of the inspection may return a lower amplitude compared to a similar defect at the bottom centre. This must be taken into account when calibrating an inspection since ultrasonic data analysis techniques can be highly reliant upon the signal amplitude.

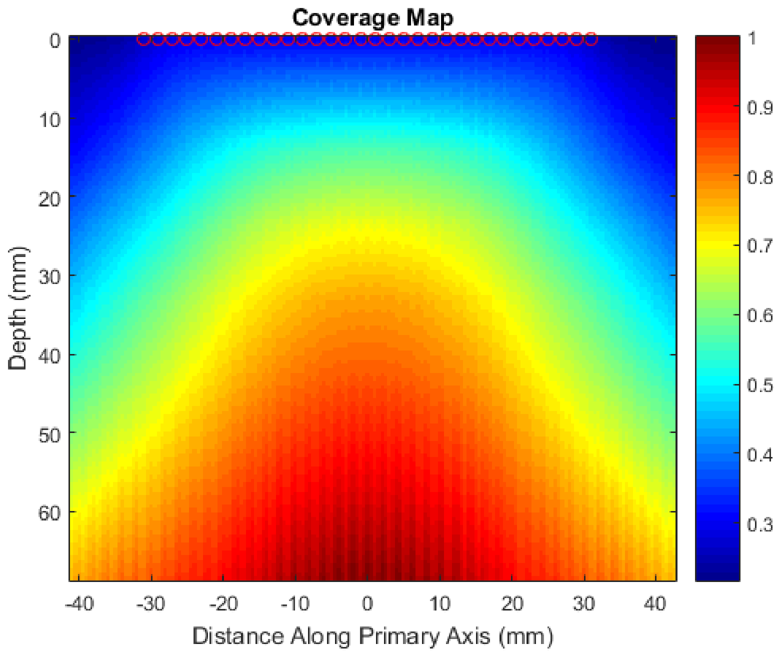

FIGURE 6.7: Sensitivity map of a TFM inspection using a linear array in contact with a steel component.

A similar procedure was followed to predict the sensitivity in a 3D TFM image, using a 2D array, still where the probe is in contact with the component. In this case the angle between the transmitter or receiver and the pixel must be calculated considering the 3D volume, however all other aspects are consistent with the linear array case. An example of coverage map for a 2D array, of 8 by 8 elements with a pitch of 2mm, inspecting a 3D volume is shown in Figure 6.8. Again the elements are indicated by red circles on the image. The coverage map is similar to the linear array contact case, with the relative sensitivity peaking at the bottom centre of the image.

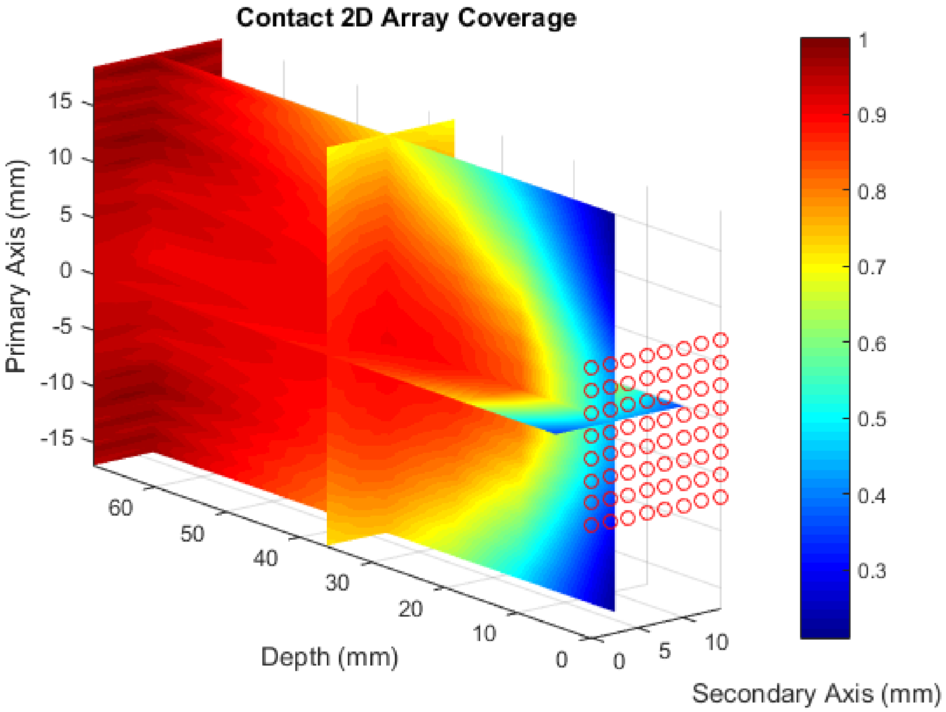

FIGURE 6.8: Sensitivity coverage of a TFM inspection using a 2D array in contact with a steel component.

The relative sensitivity in a TFM image for both the linear and 2D array in contact with a component involve relatively simple calculations. However these become increasingly complex when considering dual media and irregular surface components.

First, extending the sensitivity map to dual media means it must handle the effects of refraction. This is achieved by employing the transmission coefficients relating to non-normal incidence, as defined in Chapter 2, more specifically Equation 2.9.

A similar process to the contact case is followed, where the angle of the path between each transmitter or receiver determines the relative amplitude. The path from transmitter to receiver in the HMC is considered as a ray travelling to each pixel in the image. The PoR on the surface where refraction occurs must be determined following the same process to the TFM calculation itself, for every pixel in the image and every Tx-Rx pair. As in the contact case, the angle is used to determine the maximum amplitude possible for that path. Additionally, the angle between each transmitter or receiver and PoR is then used to along with the material properties to calculate the transmission coefficient using Equation 2.10. The transmission coefficient and maximum amplitude for the transmitter to pixel path are multiplied, before being multiplied with the same for the pixel to receiver path.

Since TFM imaging in this Thesis is only performed using the longitudinal wave velocity, only longitudinal wave sensitivity is considered here. A similar methodology could be applied to calculate the shear wave sensitivity by employing the Equation 2.10, however it is out of the scope of this work.

Figure 6.9 shows the sensitivity map for a 2MHz, 16 element linear array with a 2mm pitch inspecting steel through a 20mm water gap. The sensitivity distribution is similar to that of the contact linear array as expected. The element locations are indicated for their y-axis positions only, as they are 20mm above the surface instead of in contact with it.

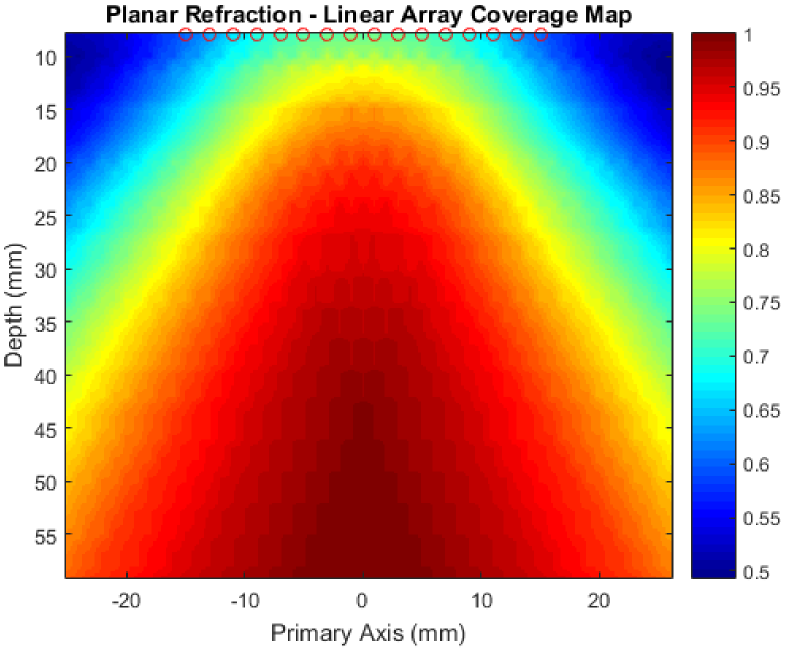

FIGURE 6.9: Sensitivity coverage map handling refraction through a planar interface with a linear array.

As with the contact case, the sensitivity map for a 2D array inspecting steel through a coupling medium can be established by calculating the 3D angle between the transmitter or receiver and PoR. An example of the sensitivity map for a 8 by 4 element 2D matrix array, operating at 2MHz with a pitch of 2mm in the primary and secondary axis is shown in Figure . As before, the inspection medium is steel and the probe coupled to the component through 20mm of water.

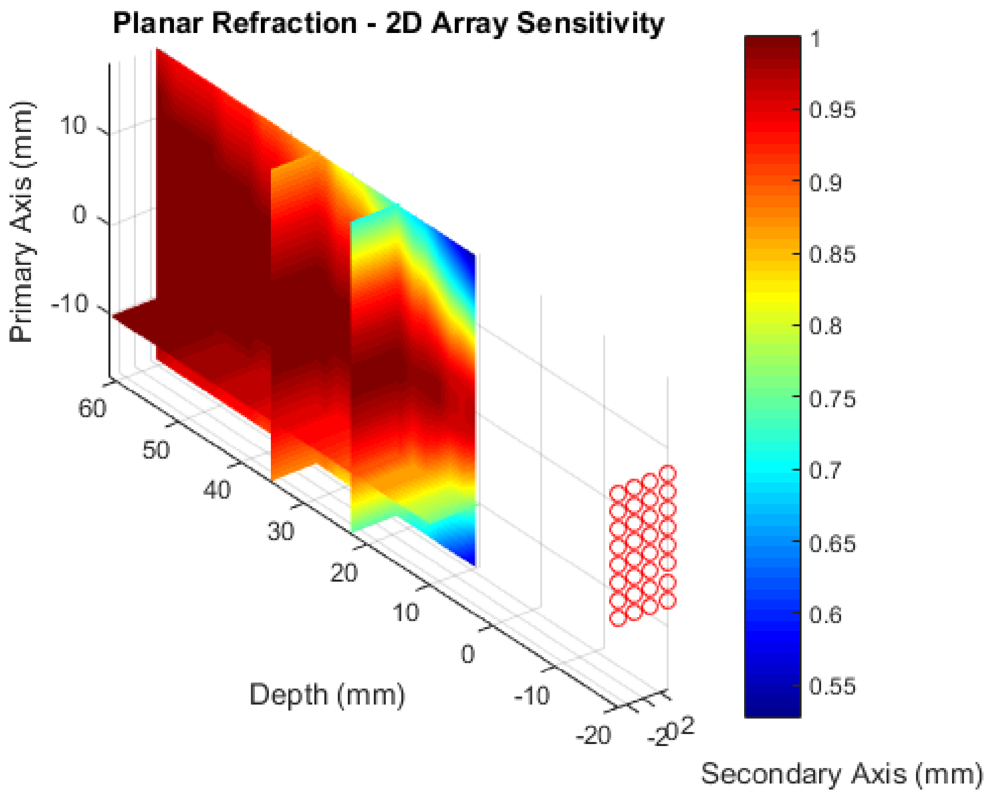

FIGURE 6.10: Sensitivity map for a 2D array inspecting steel through water coupling.

The sensitivity distribution does not deviate much for each of the configurations demonstrated so far. They all consent that the maximum sensitivity is at the centre of the array, some distance from the array. The sensitivity is relatively evenly distributed throughout the imaging regions considered, with predictable reductions in sensitivity close to the edges of the array. More complex scenarios involving irregular surface profiles or sparse 2D arrays are the focus of this work, and the sensitivity in such inspections begins to deviate from the norm in such circumstances.

The procedure for calculating the PoR on an irregular surface remains as described in Chapter 3, however the angle must be calculated from the normal to the surface, as shown in Figure 6.11. Otherwise the sensitivity can be calculated as for the case handling planar refraction.

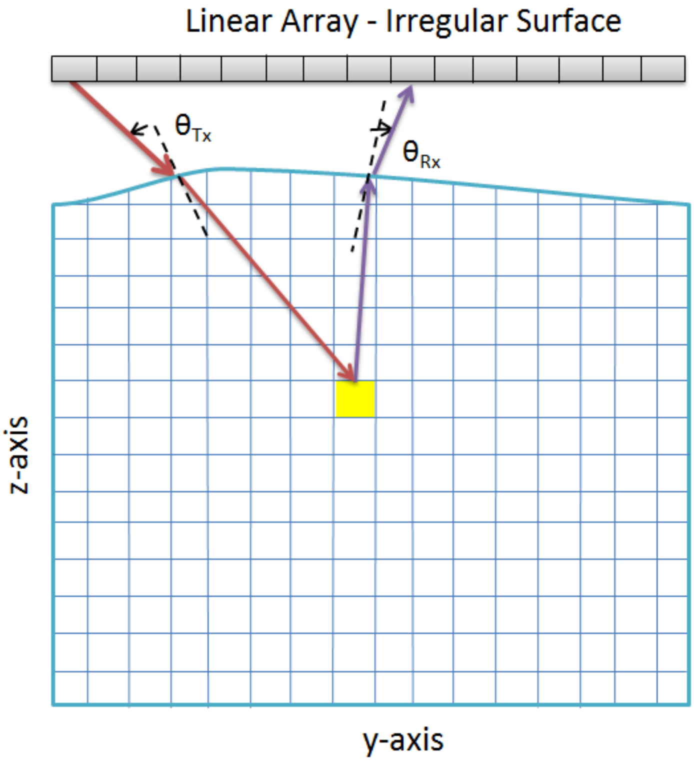

FIGURE 6.11: Calculating the angle between elements and PoR on an irregular surface for sensitivity mapping.

Figures 6.12 and 6.13 show the sensitivity map for two different irregular surface arrangements. The coverage maps were obtained assuming a 16 element linear array with a pitch of 2mm and operating frequency of 2MHz. The probe was set at 35mm in water above the steel component with an irregular surface based on positions A and C on the bespoke test block, as highlighted in Chapter 4.

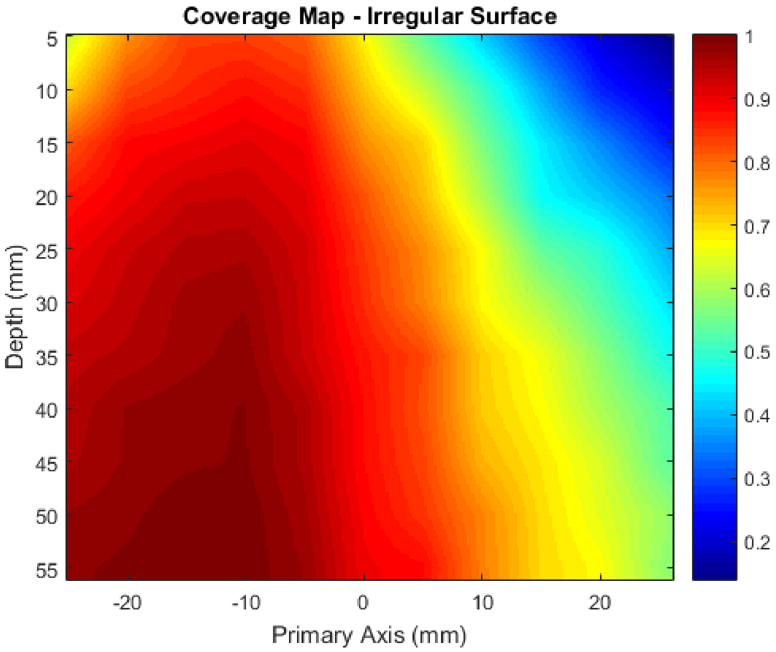

FIGURE 6.12: Sensitivity map based on position A on the irregular surface test block.

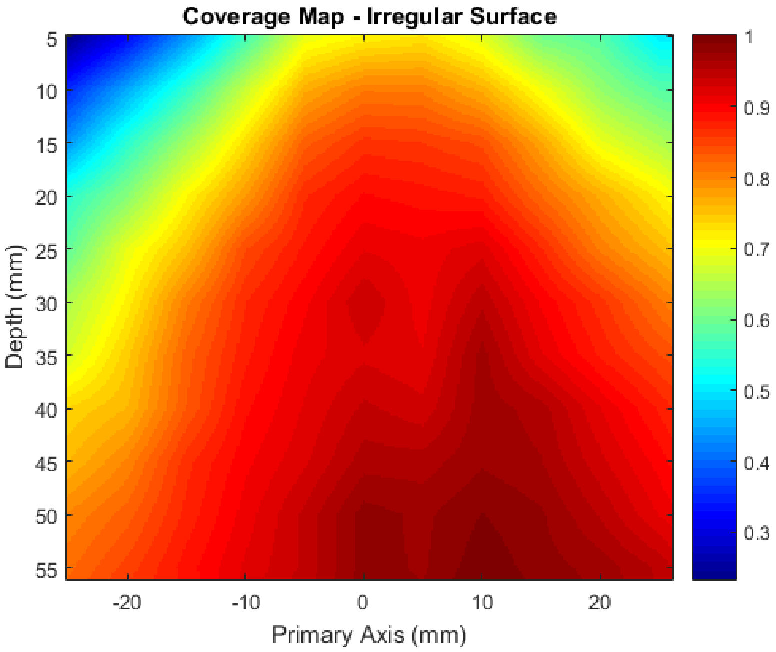

FIGURE 6.13: Sensitivity map based on position C on the irregular surface test block.

There is a clear difference between the contact case and planar surface sensitivity with the irregular surface sensitivity map. The maximum sensitivity is no longer centred at the bottom of the TFM image around the middle of the array elements. Instead the sensitivity distribution is highly dependent on the surface form. This highlights the importance and requirement of formulating a method to predict the relative sensitivity in inspection of complex components using TFM.

Calculation of the sensitivity map is not currently performed on GPUs meaning they are very computationally expensive. This initial development of a coverage map of the relative sensitivity in a TFM inspection is a new development and further work is ongoing to determine how best to employ these coverage maps to achieve equal sensitivity throughout an inspection volume. At present the coverage maps can act as a visual guide to clarify signals of spurious amplitudes. It would be beneficial to streamline calculation of the sensitivity map with the TFM image computation. This would avoid repetition of PoR calculations and significantly speed up the process.

6.3 Conformable Coupling

Data collection on the irregular surface test block has been performed using an immersion tank throughout this Thesis. It is not practically possible to perform inspection of operational plant in immersion, therefore another method capable of maintaining coupling between the probe and component must be considered. Two main options were explored, first a conformable silicone wedge and second a local immersion technique.

A silicone wedge was manufactured for use with the 2MHz sparse 2D array. A probe holder permitting movement only in the probe height was used to press the probe and wedge flat onto the surface. Physical trials proved it was difficult to ensure the probe was held in an exact, defined position using this wedge and holder combination. This was problematic since one main factor that influences TFM imaging is the accuracy of the probe element positions, with reference to the image space. Slight variations in probe angle can significantly reduce the TFM image quality due to discrepancies in the ToF calculations. The silicone also tended to be more attenuative compared with water, meaning the amplitude of signals on individual A-scans in the HMC were reduced. Together these factors meant that although the silicone wedge could provide convenient conformable coupling, it did not seem suitable for industrial UT and diverse surface form presented in this study.

Instead, a method for performing local immersion was adopted to couple the probe to an irregular surface. Various other conventional UT and development projects within Doosan Babcock employ this method, and it is approved for use on nuclear plant. It involves using a hollow probe shoe with a conformable outer edge and a water recirculation system. Water is pumped into the centre of the show, between the probe and component surface, and a vacuum removes excess water. The conformable edge ensures contact is made between the probe shoe and component, allowing the small volume under the probe to be filled locally. The flexible skirt along the bottom of the shoe can be formed by an inflatable tyre, flexible brushes or silicone rubber strips. Figure 6.14 shows a computer model of this arrangement, with the probe held in the shoe and attached to mechanical sliders that only permit movement in one direction. This combination provided a much more rigid support to move the probe on, and allowed constant coupling to be maintained between the probe and component.

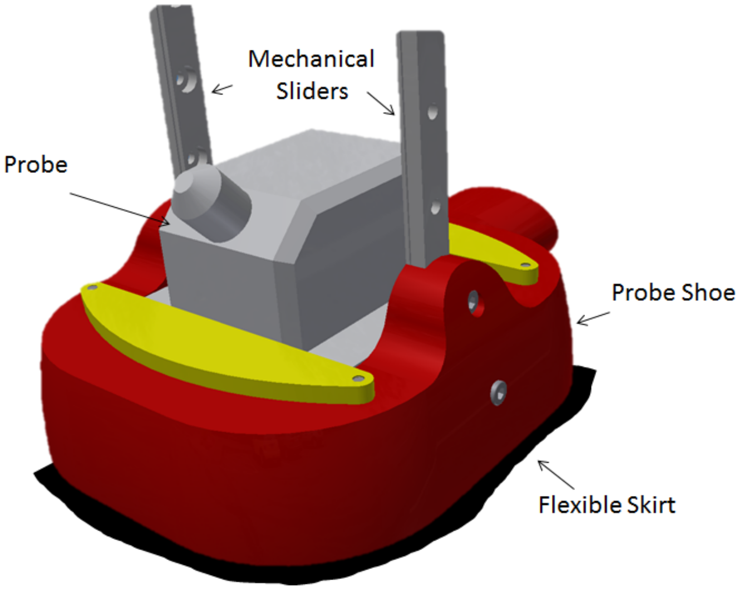

FIGURE 6.14: Illustration of a hollow probe shoe and flexible skirt and mechanical sliders to position the probe on an irregular surface and achieve conformable coupling.

6.4 Detection of Planar Defects

Defects that are likely to occur in operational components are unlikely to have the geometry of a SDH. One typical defect that is likely to transpire is an almost vertical, planar crack. Slots at various angles with a 1mm opening were therefore manufactured into the calibration block to assess the inspection system's ability to detect such flaws. Figure 6.15 details the angled slots, where the angle is clockwise from the normal to the horizontal line at 50mm from the planar BW of the block. Each of the slots are 6mm from edge to edge and penetrate half of the test block width. Further detail is given in Appendix A. Angled slots are often the machined into samples as artificial defects used to represent planar flaws that may occur in welded components. SDH are useful since they provide a specular response independent of incident angle, however angled slots rely on tip diffraction which is often required when the incident angle is not normal to the defect. As such, angled slots are an effective artificial flaw that can be used to predict the detection capability of angled, planar flaws.

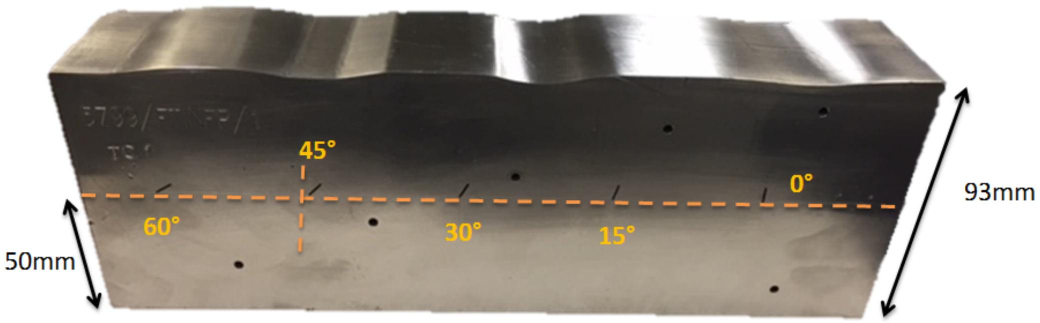

Figure 6.15: The bespoke test block with detail of the angled slots.

The following TFM images in Figure 6.16 shows the response from each of the slots on the test block as shown in Figure 6.15. The indications are of significantly lower amplitude compared with the 3mm SDH in the block, however the upper and lower tips of all of the slots are detected. The SNR of the tips for each slot is detailed in Table 6.3 and the depth of the tips is detailed in Table 6.4. The top and bottom tips for all slots except for the 0° one were detected with SNR exceeding 6dB. This is a satisfactory result and means that planar, almost vertical defects in complex components should be detected with reasonable SNR using the adapted TFM accounting for an undefined surface.

SlotID	**Top Tip SNR (dB)**	**Bottom Tip SNR (dB)**
60°	12	10
45°	14	10
30°	10	6
15°	10	5
0°	13	-

Table 6.3: SNR of the tips detected for each of the angled slots in the test block.

SlotID	**Bottom Tip Position (mm)**	**Top Tip Position (mm)**
60°	-12, 43	-8, 39
45°	8, 42	10, 38
30°	8, 43	11, 41
15°	5, 41	9, 36
0°	-	-4, 35

Table 6.4: Position in (P-Axis, Depth) for tips detected for each of the slots in the test block.

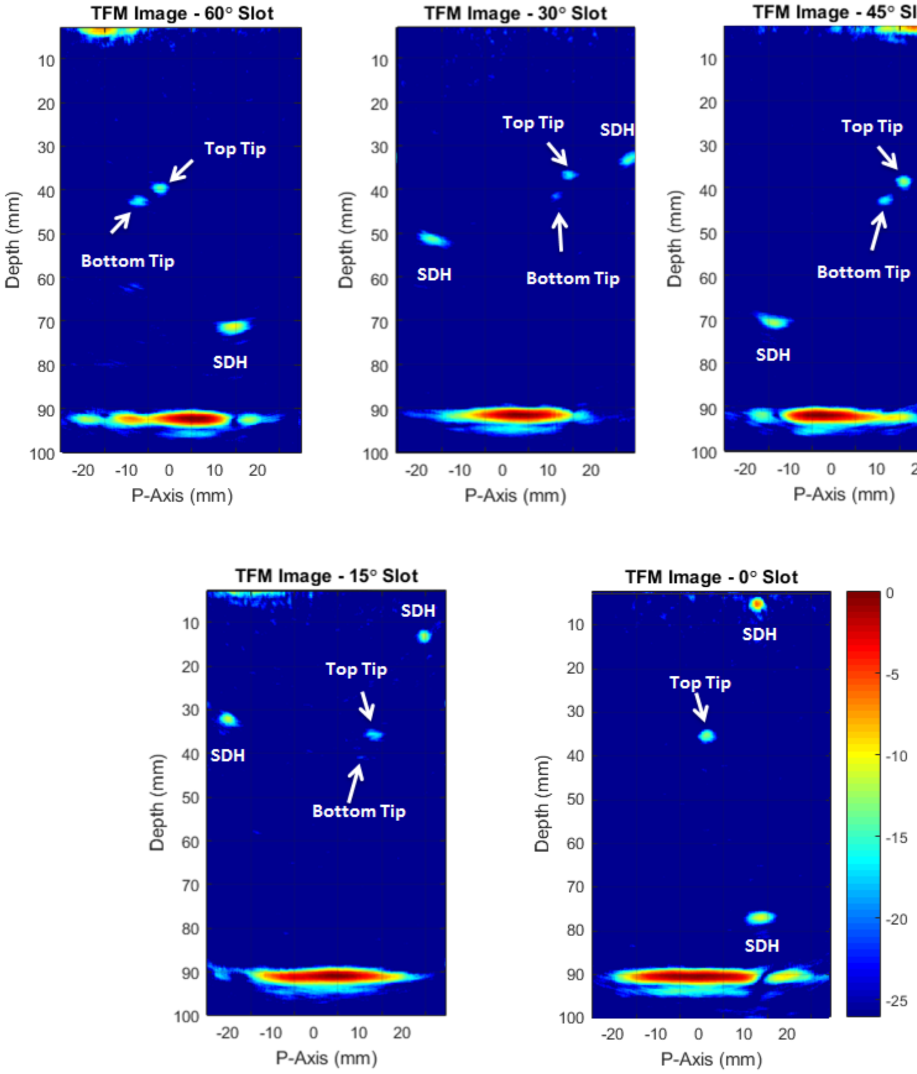

FIGURE 6.16: TFM images showing the angled slots on the test block as shown in Figure 6.15.

6.5 Discussion

An initial technique for efficiently inspecting complex components has been formed by combining advanced signal processing algorithms and a sparse 2D array. The constituent components that collectively form this system have been combined in this Chapter, with consideration for factors involved with industrial inspection. Automation of the inspection has been demonstrated by utilising a stop-start manipulator that works under instruction of the PAC. Simple image stitching has been performed to achieve a complete TFM image of the bespoke test block, showing all SDH and the BW can be detected with reasonable SNR and positioned correctly.

Furthermore, a method for predicting the sensitivity distribution in an inspection using TFM on complex components has been formulated. Further work is ongoing to decipher how best to utilise the sensitivity map and achieve TFM inspections with uniform sensitivity throughout an inspection volume.

The inspection technique is further demonstrated for it's ability to detect planar, almost vertical defects in the bespoke test block. Such flaws are representative of cracks that are likely to transpire in in-situ components. Planar flaws of various orientation were detected with reasonable SNR when employing TFM and the sparse 2D array developed in this Thesis.

Each of these factors contribute towards a significant step forward in realising TFM inspections using sparse arrays in industrial UT. This puts the industrial sponsor of this work in an excellent position for further developing an industrially robust inspection technique using TFM. This means efficient and reliable inspection of complex components is within reach, and may be achieved by following the future work recommended to compliment this Thesis.

Chapter 7

Concluding Remarks

The work presented in this Thesis details the evolution of an initial inspection technique for complex components typical of nuclear plant. The key aspects that form an inspection system have been investigated throughout this Thesis, before being combined to form an initial version of an efficient inspection technique for complex components. The objectives that were established in order to develop this inspection were outlined in Chapter 1, and are given here as a reminder:

- Development of TFM accounting for refraction through an arbitrary interface.
- Develop a method for accurately extracting and reconstructing arbitrary surface profiles.
- Design and manufacture a sparse 2D array suitable for inspecting thick section stainless steel.
- Consider automation of the inspection of complex components using TFM and sparse 2D arrays.
- Formulate a method to evaluate the sensitivity in inspection of complex components using TFM and sparse 2D arrays.
- Consider application of this technique to an example component.

This Thesis documents the work performed in accomplishing these objectives, and ultimately evaluates the initial inspection technique for purpose in industrial UT of complex components. The key findings of the work presented in this Thesis are summarised in this Chapter. Furthermore, the purpose of the EngD scheme this work was performed under is to implement technology transfer. Therefore, the benefit of this work to Doosan Babcock is discussed. Until now inspections utilising FMC, TFM and sparse 2D arrays have largely remained a research topic, the aim of this work is to transfer this technology to the industrial partner and pave the way for such inspections in an industrial environment. The industrial sponsor is now funding further development of this work to transform it into an automated inspection and the work in this Thesis provides a strong foundation for future work to be built upon. Finally, avenues for future work that would compliment the findings of this Thesis are suggested.

7.1 Key Findings

In line with the objectives set for this work, the key findings can be summarised as follows and further detail on the development of each topic is given:

- An efficient implementation of TFM capable of handling refraction through a surface varying in all directions.
- A dynamic and efficient method for accurate detection and reconstruction of arbitrary surface profiles.
- A custom designed 2MHz sparse 2D array.
- Development of an industrially robust and efficient inspection of complex components using TFM and sparse 2D arrays; including automation, image stitching and initial data analysis.
- A methodology for evaluating the relative sensitivity in inspection of complex components using TFM and sparse 2D arrays.
- Detection of planar flaws, representative of real defects, in an example test block.

7.1.1 Adaptation of TFM

The initial step in adapting TFM for inspection of complex components relied on an efficient implementation of TFM capable of handling refraction through an arbitrary interface. The background and calculations involved in this process is detailed in Chapter 3. Initially, a simple single medium inspection using a linear array is demonstrated, and the calculations are iteratively extended to manage more complex imaging scenarios. The mathematics involved in executing TFM for a dual medium inspection, with an arbitrary interface was implemented by representing the surface profile for TFM through a discrete map of the surface height. Furthermore, TFM was developed to handle arbitrary surfaces evolving in all directions. This is essential in order to apply TFM on industrial components that have undergone machining. The highlights of the author's contribution to TFM are therefore:

- Specifying the surface as a discrete map of heights.
- Validation of TFM with refraction through a 2D arbitrary interface using experimental data.
- Development and validation of TFM with refraction through a 3D arbitrary interface using simulated data.

7.1.2 Dynamic Surface Detection

An accurate representation of the surface profile is required to correctly compute the TFM image of a complex component. Small undulations (less than 2mm) occur on the surface of industrial components due to welding and machining procedures in the application relevant to this EngD. Such variations are difficult to capture on component drawings and result in a significant reduction in imaging performance for UT. A method for detecting and accurately reconstructing the irregular surface profiles is presented in this Thesis. The technique is demonstrated on a bespoke test block exhibiting an irregular surface that is representative of components requiring UT in nuclear plant. The surface extraction and reconstruction technique involves creating a TFM image of the component surface as a reflector in water and extracting and reconstructing a map of the surface height. A number of variables concerned with extracting the surface profile, including limiting pixel window and the threshold at which to extract points at is investigated. Additionally, various mathematical curve fitting algorithms are evaluated for their ability to produce a smooth and complete representation of the surface profile.

An approximation method that employs interpolation and simple smoothing was developed as it provided the most accurate representation of the surface profiles considered in this work. This dynamic surface detection and reconstruction method requires no prior information on the surface form, and only requires the user to specify an estimated probe height above the surface, threshold and pixel window. This development means a single FMC or HMC data set can be used to detect the surface profile and subsequently relayed to the TFM algorithm to correct the ToF due to the surface form. This technique has been successfully demonstrated over a range of 14 positions on the bespoke irregular surface test block, with RMS and maximum errors between the reconstructed surface and true surface profile of 0.09mm and 0.21mm respectively. The impact of accurate representation of the surface profile is demonstrated by comparison of TFM images created using the detected surface profile with those assuming a planar interface. The results demonstrate detection and positioning is significantly impaired when an accurate surface profile is not portrayed to the TFM algorithm. The technique has been demonstrated on both 2D and 3D irregular surfaces representative of those encountered on components in nuclear plant. Highlights of the author's development of this dynamic surface detection include:

- A robust and reliable method for detecting irregular surface profiles typical of components in nuclear plant, requiring minimal user intervention.
- High accuracy of surface reconstruction for both 2D and 3D cases, with errors in the range of 0.2mm.
- Significantly improved TFM images of the bespoke test block employing automatic portrayal of the surface profile.

7.1.3 Sparse 2D Array

It is essential to understand the requirements of an inspection in order to design a probe suitable for the application. The component in this context of this study is thick section stainless steel, presenting an irregular surface form. Also, the objective of this study is to perform efficient inspection of such components, with the ability to volumetrically interrogate them. Therefore sparse 2D arrays were investigated due to their economical configurations and potential equivalent performance compared with linear or 2D matrix arrays. A Poisson disk element layout was adopted as the design of a 1.5MHz sparse 2D array suitable for complex components. The array was manufactured in CUE providing the author with a beneficial insight into the limitations of array manufacture and design. Ultrasonic characterisation and evaluation of this prototype device for inspection of the bespoke test block imparted valuable lessons on the array design. Most specifically the author resolved that although a minimum spacing is set for Poisson disk distributions, it is important to ensure all elements are uniformly allocated to a degree in order to avoid significant undulations in the ultrasonic energy distributed in an inspection volume. A revised 2MHz sparse 2D array was designed again employing the Poisson disk layout, however care was taken to avoid elements with no neighbours in the range of the minimum separation. The final design encompassed 128 elements of 2mm in diameter and a minimum separation of 0.8mm over a complete aperture of 45mm by 30mm. The benchmark for the performance of the array required for this work was set by a 1MHz 2D matrix and the 2D array was able to achieve equivalent imaging performance to this. The increase in frequency from 1MHz to 2MHz means that the inspection resolution was improved while the sensitivity to defects and inspection volume was maintained. The 2MHz sparse array was demonstrated for inspection of complex components using the calibration SDH in the bespoke test block. The array was able to accurately detect the surface profile along the complete test block and correctly position the 6 SDH and BW of the component with a reasonable SNR. The highlights of the investigations on sparse 2D arrays in the context of this Thesis include:

- Design and manufacture of a prototype 1.5MHz sparse 2D array.
- Impact of nearest neighbours in Poisson disk distribution on performance.
- Revised design of a 2MHz sparse 2D array.
- Achieving equal imaging performance to the 1MHz matrix array with the 2MHz sparse 2D array for inspection of the bespoke test block.

7.1.4 Industrial Inspection Factors

The main aspects in this Thesis are combined to form an efficient inspection system for complex components. The GPU execution of TFM incorporating refraction, dynamic surface detection method and sparse 2D array are brought together in Chapter 6 and factors relating to implementing this inspection in an industrial environment are considered. The main factors include automation of the inspection, data size and collection time, sensitivity mapping and detection of representative flaws. Addressing each of these aspects moves the likelihood of an industrial inspection using TFM and sparse arrays closer to being realised.

The author has worked with Peak NDT (UK) to establish a stop-start manipulation of the probe using a 2 axis scanner. A feedback loop is utilised between the MP5 and the IMCS to ensure all of the relevant data is captured before the probe is moved to the next position. This step means the inspection can be automated and requires little intervention from personnel. Automated inspections are desirable, and often essential, in industrial NDE since the component may be placed in a hazardous environment. Such inspections are also likely to be highly repeatable since known reference positions and inspection paths are set, meaning manual intervention is minimal.

Image stitching must be performed to combine data from various probe positions into one image. A simple image stitching method using the maximum amplitude is demonstrated on the bespoke test block to achieve a single view of the complete block using data collected at incremental probe positions. Conventional UT utilises various views of the inspection data to provide a comprehensive analysis of the component. This is vital as flaws may be more obvious when using certain views of the component compared with others. The ability to perform image stitching means an overall volumetric image of the component can be achieved, any view within this can then be interrogated as required.

Since the components targets by this inspection present an irregular surface a method for conforming to the surface maintaining coupling between the probe and component is required. A hollow probe shoe with a flexible skirt is used to provide a localised water column by employing a recirculation pump. This technique has been employed in various other inspection systems by Doosan Babcock and provides and efficient and effective solution to conformable coupling here.

Data analysis techniques applied in UT typically rely on evaluation of the signal amplitude and pattern. It is therefore vital to understand the sensitivity of an inspection throughout the inspection volume. Therefore, a method for determining the relative sensitivity using TFM to inspect complex components is formed in Chapter 6. This is an essential step in moving TFM inspection towards being industrially viable.

Finally, it is important to ensure the inspection technique is suitable for detecting any expected defects in a component. The 2MHz sparse 2D array and auto correction TFM inspection method were evaluated for their ability to detect planar flaws in the bespoke test block, representative of those expected in an in service component. The 5 angled slots were all detected with reasonable SNR under a variety of irregular surface forms.

The main achievements realised through considering industrial inspection factors can be summarised as:

- Establishing an automated inspection using HMC with auto-correction TFM.
- A method for evaluating the relative inspection sensitivity using TFM on irregular surface components
- Detection of planar flaws in the bespoke test block

7.2 Technology Transfer

The work presented in this Thesis was completed through an industrially motivated EngD, where the industrial partner is a key provider of NDE services. This scheme provided a highly effective route for Doosan Babcock to perform product development. The author was given clear motivation by the industrial sponsor which was well suited to the academic partner. The author worked with a group of focused researchers in CUE to develop a collection of signal processing algorithms suited to industrial NDE. The author then adapted various aspects of this software to realise an efficient inspection for complex components. The author worked closely with both the academic and industrial partner's for the duration of the EngD project allowing the requirements of both to be addressed.

The work in this Thesis forms a preliminary package of work, allowing a business case to be formed and accepted for further development of an inspection for complex components utilising TFM. The author has played a key role in this business case and is the main technical lead in the ongoing project. The aim of this work is to achieve an industrially viable inspection system within 1 year.

The author has successfully transferred both the physical technology and valuable experience established in this work to the industrial partner. The author has a clear vision of the developments required to achieve an industrially viable inspection, and is imparting their knowledge to colleagues. Furthermore, the author has drawn upon the vast inspection experience within Doosan Babacock to ensure factors relating to performing an efficient industrial inspection are addressed.

7.3 Suggested Future Work

A number of developments that would compliment the work presented in this Thesis are identified as suggested future work. Essentially each of the aspects should contribute towards realising an industrially viable and robust inspection for complex components. The main concerns still to be addressed include data size and storage, real defect detection and analysis and streamlining of the sensitivity map.

7.3.1 Data Size and Storage

Inspections performed using FMC or HMC typically result in data sizes in the range of 10-20MB for a single probe position. Depending on the component size coverage required an inspection can therefore result in a vast amount of data being collected. Generally this data should be safely stored and accessible for the duration of the plant life. This presents a significant issue as current data storage methods are not capable of efficiently storing data of such sizes. Before inspections using TFM can be applied it is important to address how the HMC data will be stored. Two suggestions for overcoming huge data storage requirements include storing only essential data within the HMC, or only saving the processed TFM data.

Saving only useful data within the HMC the data size could be significantly reduced. This could be achieved by disregarding noise in the HMC and only storing indications above a specific threshold. A routine reconstruct the full HMC data could be used to approximate the discounted data. This may be difficult and time-consuming to apply in practice, and could result in the integrity of the data being compromised.

Similarly, saving the processed TFM data would also result in significantly less data to store compared with the HMC. However, one of the main benefits of using HMC is that the raw data remains untouched even after applying post-processing algorithms such as TFM. It is often a requirement of nuclear inspection that the raw data is stored, meaning this may not be a viable solution.

7.3.2 Inspection Qualification

An essential requirement of nuclear inspections is qualification, which involves identifying and evaluating the variables in an inspection. In the context of this inspection one of the main variables would be the impact of the surface form on any potential defects. Additionally, the technique must be evaluated for its ability to detect a variety of realistic defects.

The technique has been evaluated for detection of calibration reflectors and angled planar slots. Further evidence must be gathered on representative components containing realistic defects. A selection of experimental and simulated evidence may be used to assess the impact of variables in the inspection system.

Supplementary signal processing techniques may also assist the data analysis of inspections employing TFM. One idea is adopting the pixel windowing technique to limit the elements contributing towards a region in an inspection, similar to performing single angled inspections with phased arrays.

7.3.3 Streamlining of Sensitivity Calculation

A methodology for evaluating the relative sensitivity in a TFM inspection of complex components is presented in Chapter 6. The calculations performed to establish the sensitivity are similar to those for the TFM image itself. It would therefore be beneficial to streamline the TFM and sensitivity map calculations to avoid unnecessary repetition.

Furthermore, how to effectively use the sensitivity map must also be considered. Essentially it should be used to provide TFM inspection data that is uniform in its sensitivity to defects throughout the inspection volume. This may be achieved by applying a correction factor to the TFM data, or may require rectification of the HMC data.

7.4 Concluding Remarks & Personal Reflection

This Thesis presents the work performed in adapting TFM for inspection of complex components. The author's has contributed to the field by extending and validating TFM handling refraction through an irregular surface in both 2D an 3D. Auto correction of TFM imaging of complex components is performed by employing a dynamic surface detection technique. Furthermore, the author has transferred this technology to the industrial partner placing them in an ideal position for developing an industrially robust inspection for complex components.

Reflecting personally on my EngD experience, I have thoroughly enjoyed the mixture of academia and industry. Having a clear motivation and end goal helped immensely and the guidance and enthusiasm from both the academic and industrial partners has led to the success of the work. I feel that I have developed a good foundation of project engineering skills through management of this EngD, and I have also acquired methods for performing and presenting research to the scientific community.

Appendix A

Bespoke Test Block

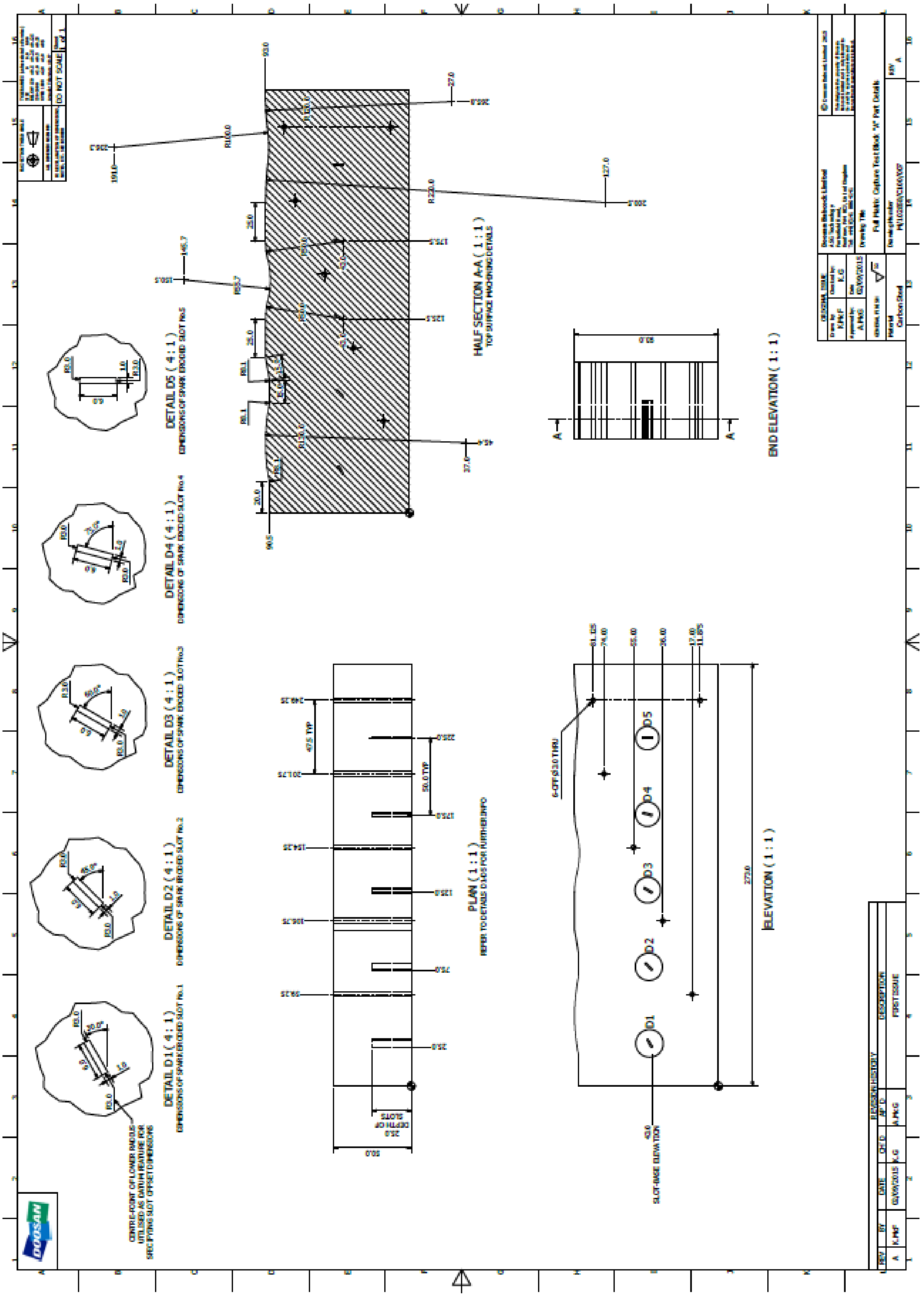
DETAIL D1 (4 : 1)
DIMENSIONS OF SPARK ERODED SLOT No.1
DETAIL D2 (4 : 1)
DIMENSIONS OF SPARK ERODED SLOT No.2
DETAIL D3 (4 : 1)
DIMENSIONS OF SPARK ERODED SLOT No.3
DETAIL D4 (4 : 1)
DIMENSIONS OF SPARK ERODED SLOT No.4
DETAIL D5 (4 : 1)
DIMENSIONS OF SPARK ERODED SLOT No.5
CENTRE-POINT OF LOWER RADIUS UTILISED AS DATUM FEATURE FOR SPECIFYING SLOT OFFSET DIMENSIONS
HALF SECTION A-A (1 : 1)
TOP SURFACE MACHINING DETAILS
PLAN (1 : 1)
REFER TO DETAILS D1-D5 FOR FURTHER INFO
25.0 DEPTH OF SLOTS
47.5 TYP
50.0 TYP
ELEVATION (1 : 1)
6-OFF Ø3.0 THRU
D1
D2
D3
D4
D5
SLOT-BASE ELEVATION
END ELEVATION (1 : 1)
A
REVISION HISTORY
FIRST ISSUE
DO NOT SCALE
DOOSAN
Doosan Babcock Limited
Full Matrix Capture Test Block "A" Part Details
Carbon Steel

Appendix B

1MHz Matrix Array

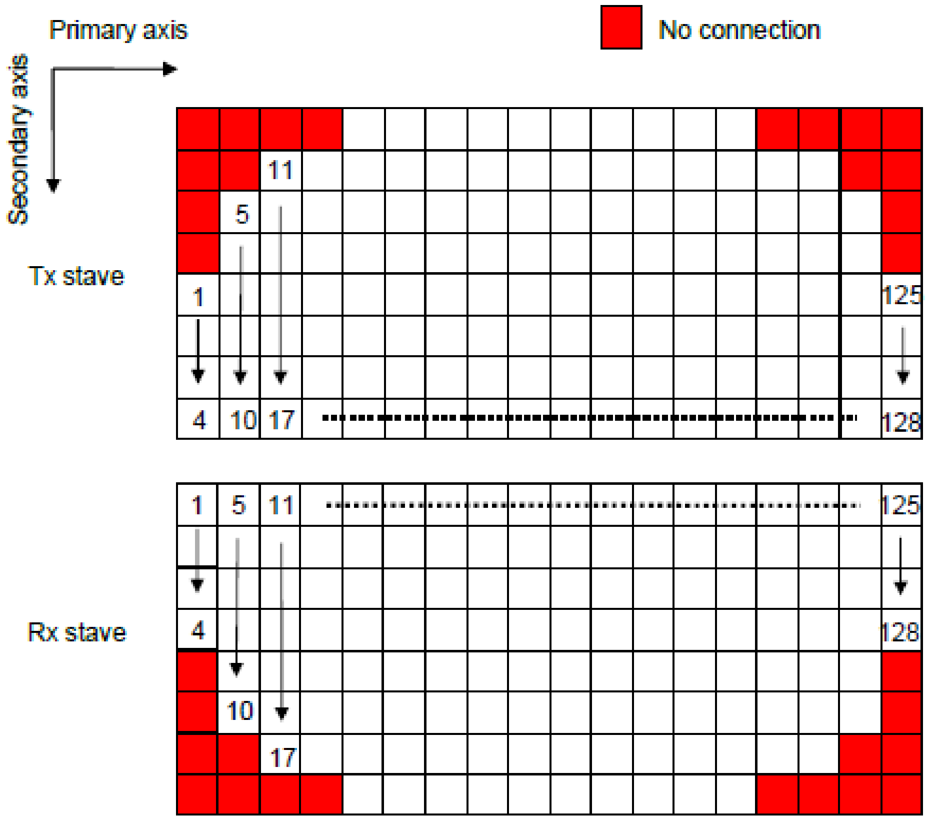

Parameter	Value
Generated wave type	Longitudinal
Array layout	2D matrix
Total number of elements	256 (128 Tx, 128 Rx)
Number of elements on primary Axis (N_P)	18
Element pitch of primary axis (p_P)	3.5 mm
Number of elements on secondary axis (N_s)	8
Element pitch of primary axis (p_s)	4.0 mm
Inter element gap (g)	0.15 mm
Frequency	1 MHz
Fractional bandwidth (-6dB)	≥ 65%
Pulse length (-20dB)	≤ 3μs

Bibliography

[1] Albert S Birks, Robert E Green, and Paul McIntire. *Ultrasonic Testing*. American Society for Nondestructive Testing, 1991.

[2] C Holmes, B W Drinkwater, and P D Wilcox. Post-processing of the full matrix of ultrasonic transmit–receive array data for non-destructive evaluation. *NDT and E International*, 38(8):701 – 711, 2005.

[3] Jerzy Dziewierz. 2d ultrasonic phased arrays for quantitative characterisation of complex defects. 2015.

[4] Timothy Lardner. New array systems for ultrasonic non-destructive evaluation of difficult materials. 2016.

[5] Miles Weston. Advanced ultrasonic digital imaging and signal processing for applications in the field of non-destructive testing, 2011.

[6] Alan J Hunter, Bruce W Drinkwater, and Paul D Wilcox. Autofocusing ultrasonic imagery for non-destructive testing and evaluation of specimens with complicated geometries. *NDT & E International*, 43(2):78–85, 2010.

[7] Sylvain Chatillon, Gérard Cattiaux, Marc Serre, and Olivier Roy. Ultrasonic non-destructive testing of pieces of complex geometry with a flexible phased array transducer. *Ultrasonics*, 38(1):131–134, 2000.

[8] Andrew Tweedie. Spiral 2d array designs for volumetric imaging, 2011.

[9] Peter J Shull. *Nondestructive evaluation: theory, techniques, and applications.* CRC press, 2002.

[10] François Le Chevalier. *Principles of radar and sonar signal processing.* Artech House, 2002.

[11] Bertram Alexander Auld. *Acoustic fields and waves in solids*, volume 2. RE Krieger, 1990.

[12] Peter R Hoskins, Kevin Martin, and Abigail Thrush. *Diagnostic ultrasound: physics and equipment.* Cambridge University Press, 2010.

[13] Josef Krautkrämer and Herbert Krautkrämer. *Ultrasonic testing of materials.* Springer Science & Business Media, 2013.

[14] Kenneth A Fowler, Gerry M Elfbaum, Karen A Smith, and Thomas J Nelligan. Theory and application of precision ultrasonic thickness gauging. *Insight*, 38(8):582–587, 1996.

[15] Emmanuel P Papadakis. Ultrasonic attenuation caused by scattering in polycrystalline metals. *The Journal of the Acoustical Society of America*, 37(4):711–717, 1965.

[16] John W Shirley. An early experimental determination of snell's law. *American Journal of Physics*, 19(9):507–508, 1951.

[17] LJ Bond and N Saffari. Mode-conversion ultrasonic testing. 1984.

[18] Harold Berger. *Nondestructive testing Standards: A Review*, volume 624. ASTM International, 1977.

[19] Antonio Arnau et al. *Piezoelectric transducers and applications.* Springer, 2008.

[20] Gordon Hayward and John A Hossack. Unidimensional modeling of 1-3 composite transducers. *The Journal of the Acoustical Society of America*, 88(2):599–608, 1990.

[21] F Dijkstra and J De Raad. The history of aut. In *European Conference on NDT*, 2006.

[22] Olympus NDT. Introduction to phased array ultrasonic technology applications. *D Tech Guideline?, Olympus NDT*, 2004.

[23] A McNab and MJ Campbell. Ultrasonic phased arrays for nondestructive testing. *NDT international*, 20(6):333–337, 1987.

[24] Shi-Chang Wooh and Yijun Shi. Optimization of ultrasonic phased arrays. In *Review of progress in quantitative nondestructive evaluation*, pages 883–890. Springer, 1998.

[25] Olympus NDT. *Advances in Phased Array ultrasonic technology applications.* Olympus NDT, 2007.

[26] ED Light, RE Davidsen, JO Fiering, TA Hruschka, and SW Smith. Progress in two-dimensional arrays for real-time volumetric imaging. *Ultrasonic Imaging*, 20(1):1–15, 1998.

[27] Eugene L Zuch. Principles of data acquisition and conversion. *Data Acquisition and Conversion Handbook*, pages 13–18, 1979.

[28] Abdul J Jerri. The shannon sampling theorem—its various extensions and applications: A tutorial review. *Proceedings of the IEEE*, 65(11):1565–1596, 1977.

[29] British Standards Institution. Bs en iso 7963:2010 non-destructive testing. ultrasonic testing - specification of calibration block. 2010.

[30] The Office for Nuclear Regulation. A guide to nuclear regulation in the uk. 2014.

[31] Jonathan Westlund and Anders Boström. Mathematical modelling of ultrasonic testing of components with defects close to a non-planar surface. Technical report, Swedish Radiation Safety Authority, Stockholm (Sweden), 2011.

[32] RK Chapman and KJ Bowker. Production of capability statements for standard ndt procedures. In *NDT 2000: Annual Conference of the British Institute of Non-Destructive Testing Proceedings*, pages 197–202, 2000.

[33] Steve Lampman. Weld integrity and performance. *ASM International*, 1997.

[34] Bruce W. Drinkwater and Paul D. Wilcox. Ultrasonic arrays for non-destructive evaluation: A review. *NDT and E International*, 39(7):525 – 541, 2006. ISSN 0963-8695.

[35] P. D. Wilcox, C. Holmes, and B. W. Drinkwater. Exploiting the full data set from ultrasonic arrays by post-processing. *AIP Conference Proceedings*, 820 (1):845–852, 2006.

[36] Alexander Velichko and Paul D. Wilcox. An analytical comparison of ultrasonic array imaging algorithms. *The Journal of the Acoustical Society of America*, 127(4):2377–2384, 2010.

[37] R/D Tech. *Introduction to Phased Array Ultrasonic Technology Applications: R/D Tech Guideline*. Advanced practical NDT series. R/D Tech, 2004. ISBN 9780973593303.

[38] Jie Zhang, Bruce W Drinkwater, and Paul D Wilcox. Comparison of ultrasonic array imaging algorithms for non-destructive evaluation. *IEEE*

Transactions on Ultrasonics, Ferroelectrics, and Frequency Control, 60(8): 1732–1745, 2013.

[39] D I A Lines. Rapid distributed data collection and processing with arrays - the next step beyond full waveform capture. *Insight - Non-Destructive Testing and Condition Monitoring*, 48(2):84–88, 2006.

[40] Patrick Tremblay and Daniel Richard. Development and validation of a full matrix capture solution. pages 457–466, 2012.

[41] Patrick Tremblay and Daniel Richard. Development and validation of a full matrix capture solution.

[42] L Moreau, AJ Hunter, BW Drinkwater, PD Wilcox, Donald O Thompson, and Dale E Chimenti. Efficient data capture and post-processing for real-time imaging using an ultrasonic array. *Aip Conference Proceedings*, 1211(1):839, 2010.

[43] A. Van Pamel, C R Brett, and M JS Lowe. A methodology for evaluating detection performance of ultrasonic array imaging algorithms for coarse-grained materials. *IEEE Transactions on Ultrasonics, Ferroelectrics, and Frequency Control*, 61(12):2042–2053, 2014.

[44] D Hopkins, G Neau, and L Le Ber. Advanced phased-array technologies for ultrasonic inspection of complex composite parts. 2011.

[45] C Mack. The multiple lives of moore's law. *Spectrum, IEEE*, 52(4):31–37, 2015.

[46] C Fan, M Caleap, M Pan, and B W Drinkwater. A comparison between ultrasonic array beamforming and super resolution imaging algorithms for non-destructive evaluation. *Ultrasonics*, 54(7):1842 – 1850, 2014.

[47] J Kitze, J Prager, R Boehm, U lz, HJ Montag, Donald O Thompson, and Dale E Chimenti. Saft-reconstruction in ultrasonic immersion technique using phased array transducers. In *AIP Conference Proceedings-American Institute of Physics*, volume 1430, page 825, 2012.

[48] Roy Edgar Hansen. *Introduction to Synthetic Aperture SONAR.* INTECH Open Access Publisher, 2011.

[49] J Camacho, M Parrilla, and C Fritsch. Phase coherence imaging. *IEEE Transactions on Ultrasonics, Ferroelectrics, and Frequency Control*, 56(5): 958–974, 2009.

[50] P D Wilcox, C Holmes, and B W Drinkwater. Enhanced defect detection and characterisation by signal processing of ultrasonic array data. *Proc. 9th ECNDT*, 2006.

[51] J Davies, F Simonetti, M Lowe, and P Cawley. Review of synthetically focused guided wave imaging techniques with application to defect sizing. In *Quantitative Nondestructive Evaluation*, volume 820, pages 142–149. AIP Publishing, 2006.

[52] J Dziewierz and A Gachagan. A design methodology for 2d sparse nde arrays using an efficient implementation of refracted-ray tfm. 2013.

[53] M. Njiki, A. Elouardi, S. Bouaziz, O. Casula, and O. Roy. Total focusing method for non-destructive evaluation: Toward real-time imaging systems. pages 1164–1167, 2013.

[54] J Dziewierz and A Gachagan. Correspondence: Computationally efficient solution of snell's law of refraction. *IEEE Transactions on Ultrasonics, Ferroelectrics, and Frequency Control*, 60(6):1256–1259, 2013.

[55] J Fung and S Mann. Using multiple graphics cards as a general purpose parallel computer: Applications to computer vision. In *Proceedings of the 17th International Conference on Pattern Recognition, 2004. ICPR 2004*, volume 1, pages 805–808. IEEE, 2004.

[56] V Boyer and D El Baz. Recent advances on gpu computing in operations research. In *Parallel and Distributed Processing Symposium Workshops*, pages 1778–1787. IEEE, 2013.

[57] Marc A Suchard, Quanli Wang, Cliburn Chan, Jacob Frelinger, Andrew Cron, and Mike West. Understanding gpu programming for statistical computation: Studies in massively parallel massive mixtures. *Journal of Computational and Graphical Statistics*, 19(2):419–438, 2010.

[58] John E Stone, David J Hardy, Ivan S Ufimtsev, and Klaus Schulten. Gpu-accelerated molecular modeling coming of age. *Journal of Molecular Graphics and Modelling*, 29(2):116–125, 2010.

[59] S W Keckler, W J Dally, B Khailany, M Garland, and D Glasco. Gpus and the future of parallel computing. *IEEE Micro*, 31(5):7–17, 2011.

[60] F Misiorek, M Stankiewicz, P Pawlowski, and A Dabrowski. Efficient use of graphics cards in implementation of parallel image processing algorithms. In *Proceedings of the 18th International Conference Mixed Design of Integrated Circuits and Systems (MIXDES)*, pages 592–595. IEEE, 2011.

[61] David Kirk. Nvidia cuda software and gpu parallel computing architecture. In *ISMM*, volume 7, pages 103–104, 2007.

[62] NVidia. Cuda parallel computing, 2015. URL `http://www.nvidia.co.uk/object/cuda-parallel-computing-uk.html`.

[63] N Cameron and Dikstra B J. Practical assessment of phased array beam generation. *9th European Conference on NDT*, 2006.

[64] A Tweedie, R L O'Leary, G Harvey, A Gachagan, C Holmes, P D Wilcox, and B W Drinkwater. Total focussing method for volumetric imaging in immersion non destructive evaluation. In *Ultrasonics Symposium*, pages 1017–1020. IEEE, 2007.

[65] Arthur Schuster. *An introduction to the Theory of Optics*. E. Arnold, 1904.

[66] BS EN ISO 17640:2010. Non-destructive testing of welds - ultrasonic testing - techniques, testing levels and assessment.

[67] Michael W Sayers and Steven M Karamihas. *The little book of profiling*, volume 2. 1998.

[68] ML Dufour, G Lamouche, V Detalle, B Gauthier, and P Sammut. Low-coherence interferometry - an nnced technique for optical metrology in industry. *Insight-Non-Destructive Testing and Condition Monitoring*, 47(4): 216–219, 2005.

[69] FT Arecchi, D Bertani, and S Ciliberto. A fast versatile optical profilometer. *Optics Communications*, 31(3):263–266, 1979.

[70] Gwénaël Toullelan, Arnaud Nadim, Olivier Casula, Philippe Dumas, Elie Abittan, and Loïc Doudet. Inspection of complex geometries using flexible phased-array transducers. In *17th World Conference on NonDestructive Testing*, 2008.

[71] Frederic B Cegla, Peter Cawley, Jonathan Allin, and Jacob Davies. High-temperature (below 500 c) wall thickness monitoring using dry-coupled ultrasonic waveguide transducers. *Ultrasonics, Ferroelectrics, and Frequency Control, IEEE Transactions on*, 58(1):156–167, 2011.

[72] Nava-Balanzar Luciano, Soto-Cajiga Jorge Alberto, Pedraza-Ortega Jesús Carlos, and Ramos-Arreguin Juan Manuel. Development of an ultrasonic thickness measurement equipment prototype. In *Electronics, Communications and Computer (CONIELECOMP), 2010 20th International Conference on*, pages 124–129. IEEE, 2010.

[73] Billur Barshan. Ultrasonic surface profile determination by spatial voting. In *Instrumentation and Measurement Technology Conference, 2001. IMTC 2001. Proceedings of the 18th IEEE*, volume 1, pages 583–588. IEEE, 2001.

[74] J Seydel. Ultrasonic synthetic-aperture focusing techniques in ndt. *Research techniques in nondestructive testing.*, 6:1–47, 1982.

[75] Inc MathWorks. *Curve fitting toolbox: for use with MATLAB® : user's guide.* MathWorks, 2002.

[76] Andreas Austeng and Sverre Holm. Sparse 2-d arrays for 3-d phased array imaging-design methods. *Ultrasonics, Ferroelectrics, and Frequency Control, IEEE Transactions on*, 49(8):1073–1086, 2002.

[77] Frédéric Reverdy, G Ithurralde, and Nicolas Dominguez. Advanced ultrasonic 2d phasedarray probes.

[78] Sivaram Ramadas, Joseph Jackson, Jerzy Dziewierz, Richard O'Leary, and Anthony Gachagan. Application of conformal map theory for design of 2-d ultrasonic array structure for ndt imaging application: a feasibility study. *Ultrasonics, Ferroelectrics, and Frequency Control, IEEE Transactions on*, 61(3):496–504, 2014.

[79] Ares Lagae and Philip Dutré. A comparison of methods for generating poisson disk distributions. In *Computer Graphics Forum*, volume 27, pages 114–129. Wiley Online Library, 2008.

[80] Wallace Arden Smith, Bertram Auld, et al. Modeling 1-3 composite piezoelectrics: thickness-mode oscillations. *Ultrasonics, Ferroelectrics, and Frequency Control, IEEE Transactions on*, 38(1):40–47, 1991.

[81] RP Pape. Developments in the tolerability of risk (tor) and the application of alarp. *Nuclear energy*, 36(6):457–463, 1997.

[82] Richard Szeliski. Image alignment and stitching: A tutorial. *Foundations and Trends® in Computer Graphics and Vision*, 2(1):1–104, 2006.

[83] Chia-Yen Chen and Reinhard Klette. Image stitching—comparisons and new techniques. In *Computer Analysis of Images and Patterns*, pages 615–622. Springer, 1999.